TOWARDS HIGH-TURNDOWN-RATIO SHAPE MEMORY ALLOY DRIVEN MORPHING SPACE RADIATORS: MANUFACTURING METHODS, COMPUTATIONAL MODELING, AND PROTOTYPE DEMONSTRATION

A Thesis

by

PATRICK PHILIP WALGREN

Submitted to the Office of Graduate and Professional Studies of
Texas A&M University
in partial fulfillment of the requirements for the degree of

MASTER OF SCIENCE

Chair of Committee,	Darren Hartl
Committee Members,	John Whitcomb
	Jim Boyd
Head of Department,	Rodney Bowersox

May 2019

Major Subject: Aerospace Engineering

ABSTRACT

Future manned space missions will require thermal control systems that can adapt to larger fluctuations in temperature and heat flux that exceed the capabilities of current state-of-the-art systems. These missions will demand novel space radiators that can vary the heat rejection rate of the system to maintain the crew cabin at habitable temperatures throughout the entire mission. Current systems can provide a turndown ratio (defined as the ratio of maximum to minimum heat rejection) of 3:1 under adverse conditions. However, future missions are projected to demand thermal control systems that can provide a turndown ratio of more than 6:1. A novel morphing radiator concept varies the system heat rejection rate by altering the shape of the radiator that is exposed to space. This shape change is accomplished through the use of shape memory alloys, a class of active materials that exhibit thermomechanically-driven phase transformations and can be used as both sensors and actuators in thermal control applications. In past efforts, prototype morphing radiators have been tested in a relevant thermal environment, demonstrating the feasibility and scalability of the concept. This thesis summarizes the progress towards testing a high-performance morphing radiator in a relevant thermal environment. Different methods of achieving load transfer between the shape memory alloy actuators are studied, an efficient numerical model that predicts the mechanical response of an arbitrary morphing radiator configuration due to changes in temperature is developed, and a flight-quality prototype is tested in a relevant environment.

DEDICATION

To my roots.

Notice that the stiffest tree is most easily cracked, while the bamboo or willow survives by bending with the wind.

ACKNOWLEDGMENTS

I would like to thank our collaborators at NASA: Dr. Othmane Benafan, for providing the SMA strips used in the thermal vacuum chamber testing, and Ms. Lisa Erickson, for providing guidance throughout the entire two year process.

Special thanks to Dr. Mike Fowler from NASA Johnson Space Center for providing invaluable guidance on best practices for adhesively bonding composites.

I would like to thank my undergraduate research assistants throughout the project: Matthew Wescott, for getting me up to speed and being patient enough to teach me how to make composites; Jorge Chong, for being a combination of kindness, curiousity, and inquisitiveness that I hope to one day match; Kurtis Parker, for approaching every problem with the same grit; and Gerardo Garza, for sacrificing your last week in College Station to prepare prototypes.

Special thanks to Dr. Hieu Truong for providing her SMA-composite bonding expertise.

The guidance of Rodney Inmon with MTS tensile testing is much appeciated.

The machining expertise of Zahir Udovic for manufacturing the steel terminal blocks is gratefully acknowledged.

Special thanks to Adam Kellen and the EIC staff for providing machining capability for the morphing radiator end caps and tube mount.

The assistance and support of the vacuum chamber technicians at Johnson Space Center is gratefully acknowledged.

Special thanks to Thomas Cognata and Miguel Perez for fabricating and installing the multi layer insulation.

Thank you to Hannah Stroud, Jacob Mingear, and Madalyn Mikkelsen for proofreading and editing this work for publication.

The photography expertise and patience of Kevin Lieb for directing the morphing radiator photoshoot is gratefully acknowledged.

CONTRIBUTORS AND FUNDING SOURCES

Contributors

This work was supervised by a committee consisting of Professor Darren Hartl (advisor) and Professor Jim Boyd of the Department of Aerospace Engineering and Professor John Whitcomb of the Department of Materials Science.

The computational tool for extracting experimental curvature measurements of the morphing radiator was provided by Jorge Chong (B.S. Aerospace Engineering, Class of 2018), and the simulation models for converting morphing radiator curvature into heat rejection rates was provided Chris Bertagne (M.S. Aerospace Engineering, Class of 2016).

Shape memory alloy characterization tools were provided by Pedro Leal (M.S. Mechanical Engineering, Federal University of Rio de Janeiro Class of 2016) and the one-dimensional shape memory alloy constitutive model was provided by Dr. Edwin Peraza Hernandez.

Machining work for this study was preformed by Zahir Udovic, Adam Kellen, and the Engineering Innovation Center (EIC) staff.

All other work conducted for the thesis was completed by the student independently.

Funding Sources

This graduate study was supported financially by a NASA Internal Research and Development grant.

TABLE OF CONTENTS

LIST OF FIGURES

FIGURE Page

LIST OF TABLES

TABLE Page

1. INTRODUCTION

1.1 Motivation

On April 13th, 1970, the number 2 oxygen tank on the Apollo 13 lunar module exploded due to a wire short-circuit, setting off a catastrophic chain reaction that left the astronauts onboard without electrical power generation capabilities [1]. Over the next four days, the crew worked tirelessly to remedy problems caused by the accident and prepare for a mission abort to send them home. During this time, temperatures inside the crew capsule dropped to 4°C (39°F) due to the lack of cabin heat, and water started to condense on critical surfaces risking further electrical short-circuits [2, 3]. As a result of a multinational effort to devise retrofits of existing systems and the resiliency of the crew to perform in situ repairs while under intense pressure, the Apollo 13 capsule safely splashed down in the Pacific Ocean on April 17th.

Apollo 13 illustrates the dangers of human spaceflight and the harsh nature of space, especially in terms of the thermal environment encountered. Spacecraft rely on the thermal control system (TCS) to maintain and regulate the temperature of critical components within acceptable ranges throughout the entire mission profile [4]. Overall, the TCS is responsible to maintain the energy balance of the spacecraft: the amount of heat absorbed must equal the amount of heat dissipated. The heat absorbed by the spacecraft may be generated from internal components (i.e., electrical motors or human astronauts), or be radiated from planetary or solar bodies [4]. However, the heat dissipated by the TCS can only be emitted as IR radiation, as convection does not exist in the vacuum of space. This is typically accomplished via the use of a radiator, strategically positioned and coated to reject different amounts of heat depending on the mission profile.

As nations once more turn towards human space exploration beyond LEO, TCS requirements will become much more stringent in terms of both weight and heat rejection capability the system can support. Typically, a particular TCS is sized such that the system can support the maximum possible heat load in the warmest thermal environment experienced on the mission. This requirement drives the size of the radiator; the more surface area the radiator covers, the larger heat load the system as a whole can reject. However, most long-haul space missions are characterized by large fluctuations in both heat load and thermal environment. To quantify the capability of different radiator systems to adapt for the different thermal environments, a performance metric called the *turndown ratio* is used and will be detailed in section 1.2.1 [5].

Current state-of-the-art radiators can provide a turndown ratio (TDR) of 3:1, but future missions to the Moon or Mars are projected to require TDRs up to an order of magnitude higher [6, 7, 8]. This increased requirement necessitates novel TCS designs such as *variable heat rejection radiators*. Previous work has considered digital radiators, electrochromic radiators, expandable radiators, or stowable radiators [9, 10, 11, 12]. Another concept, known as a *morphing radiator*, varies the system heat rejection rate by changing the physical geometry of the radiator [13, 14]. The morphing radiator uses the temperature-dependent phase transformation of shape memory alloy (SMA) materials to passively deform the radiator in response to environmental temperatures or internal heat loads. This shape change is accomplished without external input and simplifies the control system of the radiator by negating the need for external control or sensing instrumentation. Additionally, the concept is predicted to provide turndown ratios upwards of 35:1, which can enable the use of nontoxic heat transfer fluids with higher freezing points (e.g., propylene glycol) in a single fluid loop, potentially reducing the TCS weight by 23% [15]. The morphing radiator concept has been studied extensively in recent years; computational tools for simulating the coupled radiation have been developed and validated with multiple years of thermal vacuum chamber testing [14, 16, 17].

In the past few years, tested morphing radiator prototypes have progressed from copper to carbon fiber composite panels, maturing the design towards a realistic space radiator. This thesis focuses on different methods to further improve the performance of morphing radiator prototypes. A composite design tool is formulated to account for SMA constitutive behavior and the physical assembly of the radiator panel to efficiently predict the mechanical response of the panel to temperature stimuli. A systematic bonding study is completed to investigate the potential of adhesively bonding the SMA actuator onto the panel, which increases the heat transfer between the composite and SMA, and decreases the amount of transformation strain required to fully open the radiator. Finally, the rationale gained from the bonding study and design tool is implemented during the fabrication of morphing radiator prototypes, which are tested in a thermal vacuum chamber.

1.2 Literature Review

1.2.1 Review of Spacecraft Thermal Control and Variable Heat Rejection Technology

TCS operations can be segmented into three main phases: *acquisition*, where waste heat is collected from components or the crew cabin by use of an evaporator, *transport*, where the heat is transferred away from the evaporator with a working fluid through pipes, and *rejection*, where the waste heat is expunged into the environment by use of a radiator [18]. This system is similar to the system installed in the air conditioning systems of most cars, but instead of using a condenser to reject cooled air into the cabin, spacecraft use IR radiation to maintain the craft within a nominal temperature range. Different classes of spacecraft and missions yield vastly different TCS requirements; for example the Apollo Command Service Module (CSM) TCS was initially designed for a maximum heat rejection rate of 1.08 kW, a capability that was increased to 2.2 kW for lunar missions [19]. Conversely, the International Space Station (ISS) active thermal control system (ATCS) can reject a maximum heat load of 70 kW [8]. This stark difference in heat rejection requirements stems from the mission objectives of each platform; the Apollo CSM was designed to support three crewmen for fourteen days, while the ISS has been inhabited for more than eighteen years and supports up to ten astronauts for long-duration Low Earth Orbit (LEO) missions. Figure 1.1 depicts examples of space radiators used on the Apollo CSM and the ISS.

Heat rejected from the radiator results in a decrease in coolant temperature due to the conservation of energy. When the environment is cold or the heat load is low, the radiator temperature becomes extremely cold. This can lead to fluid freezing, which can result in difficulty controlling the TCS setpoint, mission failure, or even total loss of the crew. Current spacecraft ensure the fluid will not freeze by using fluids with low freezing points, such as Ammonia or Freon-21. However,

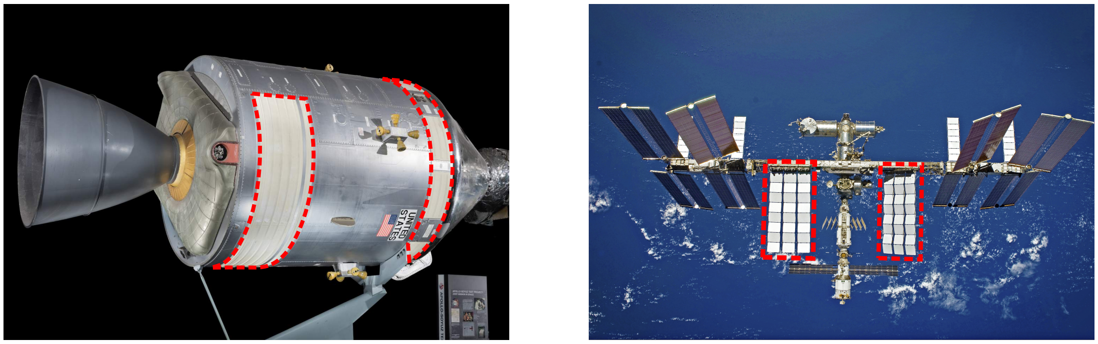

(a) Apollo Command Service Module. Adapted under fair use policy from [20]

(b) International Space Station. Adapted under fair use policy from [21]

Figure 1.1: Examples of historically used radiators, highlighted in red dashed lines.

these fluids are highly toxic and thus must be isolated from the crew, resulting in the necessity of a two-fluid-loop TCS. These designs add system complexity in the form of additional tubing and heat exchangers between the fluid loops, up to 23% of extra weight, and increase the possibility of more difficult repairs [7, 15, 22]. Single fluid loop TCS decrease the overall spacecraft mass and are sized smaller due to the increased efficiency without a heat exchanger. Additionally, they are more easily repaired, as all of the pumps are located within the crew cabin. But, while most higher freezing point fluids are nontoxic (e.g., propylene glycol or water), they present the risk of freezing if the radiators reject too much heat during the coldest phases of the mission. To ameliorate this, radiators must adapt the heat rejection rate depending on the mission profile - an ideal radiator would be one that is able to reject absolutely no heat during the coldest phase of the mission, eliminating the possibility of fluid freezing.

The turndown ratio (TDR) is a quantity that describes the ability of a radiator to adapt to different thermal environments, and is defined as the ratio between the maximum heat load rejected in the warmest thermal environment and the minimum heat load rejected in the coldest thermal environment:

$$TDR = \frac{q_{max}|_{T_{sink,max}}}{q_{min}|_{T_{sink,min}}} \approx \frac{q_{max}}{q_{min}}. \tag{1.1}$$

This quantity is sometimes approximated as the ratio between the maximum and minimum heat rejection rates, without regard to the sink temperatures. While this approximation captures the importance of varying heat rejection rate, it neglects the effect of an *adverse temperature profile* in which the radiator is required to reject large amounts of heat to a warm environment. However, it can be used as a method of comparing different radiator systems that were designed for different temperature profiles.

The spacecraft radiators on the ISS and Apollo CSM were able to support TDRs of around 3:1 via different methods. The ISS radiators can vary the heat rejection rate by rotating each array (shown in the red box of figure 1.1b) about the long axis. For maximum heat rejection, the radiator panel normals face the earth, while for minimum heat rejection, the radiator edges face the sun [8]. The Apollo CSM accomplished a TDR of 3:1 via the use of ethylene glycol, a thermal working fluid that is now banned from use due to its toxicity [7], and a radiator design that stagnated fluid during colder stages of the mission [19]. However, recent NASA programs have considered missions reaching much farther into space than the ISS orbits, and staying much longer than the Apollo astronauts walked on the moon. These missions encounter much more adverse temperature profiles, and thus require radiators with much higher turndown capability.

To illustrate this, consider the now-canceled Altair lunar lander [23]. The Altair lander was a modular approach to NASA establishing a lunar outpost, and was designed to land anywhere on the moon, return anytime, and stay longer (when compared to the Apollo lunar module) [24]. This goal represented a substantial increase in mission complexity compared to the Apollo program. The Apollo lunar missions were conducted in equatorial and near-temperature zones on the nearside of the moon, as opposed to landing at the lunar poles. Additionally, Apollo missions always coincided with lunar dawn to ensure minimal thermal variations were encountered. Finally, Apollo was only designed to stay on the lunar surface for two or three days with a maximum total mission duration of twelve days. The Altair program was projected to require seven day sorties on the lunar surface, with total mission durations reaching upwards of forty days.

A typical two-week Altair mission profile is depicted in figure 1.2, with the heat rejection rate denoted as a red dashed line and the effective sink temperature as a solid black line [7]. The

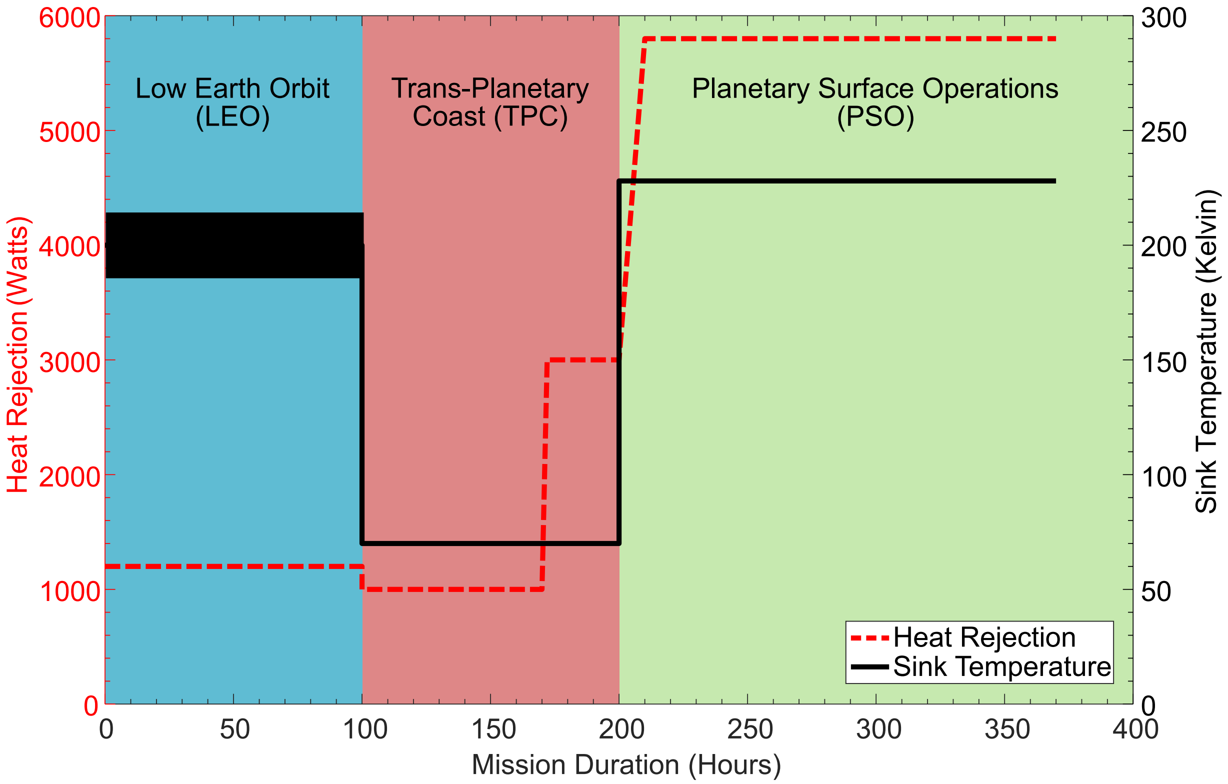

Figure 1.2: Notional temperature-heat load requirements for the Altair lunar lander mission.

mission profile is simplified to include the three main phases of flight: Low Earth Orbit (LEO), where the spacecraft is orbiting around Earth after launch; Trans-Planetary Coast (TPC), where the spacecraft has preformed a trajectory burn and is on course for the moon; and Planetary Surface Operations (PSO), where the spacecraft has landed on the moon and the astronauts are conducting daily science or colonization tasks. Each segment of the mission exhibits a different combination of heat rejection rate required and effective sink temperature, complicating the design of the TCS. During LEO, the TCS must reject a relatively low amount of heat to a relatively warmer environment, as the astronauts and equipment are not very active but the spacecraft is orbiting a warm radiating body. As the spacecraft enters TPC, the heat rejection rate stays low but the effective sink temperature drops due to the environment of deep space. This transition requires the radiator to "turn down" the operating temperature while maintaining a constant heat rejection rate. However, as the spacecraft nears the end of TPC and the orbital insertion burn is performed, the required heat rejection rate increases. This increase continues during PSO, as the electrical systems and astronauts are operating at full capacity. Additionally, as the spacecraft is on the surface of a planetary body, the effective sink temperature increases[1]. This concurrent increase in sink temperature and heat rejection requires the radiator to "turn up" the heat rejection rate it can support, in an adverse environment. Analysis has shown that the "turn up" is much more difficult for radiators to support than the "turn down," especially in a reasonable time span [7].

To begin to understand how radiators improve turndown performance, it is necessary to review the modes of heat transfer governing typical spacecraft TCS. As mentioned earlier, most TCS consist of a fluid loop that transports thermal energy from the spacecraft to radiators, which in turn reject waste heat to empty space [4]. This process of thermal transport from the crew cabin to the radiators can be described by the *simplified steady-flow thermal energy equation*:

$$q = \dot{m} c_p \Delta T, \tag{1.2}$$

where q represents the net rate of outflow of thermal energy, $\dot{m}$ describes the mass flow rate of the fluid (which is assumed to be steady in this case), c_p represents the specific heat capacity of the fluid, and ΔT describes the change in fluid temperature measured from the system outlet to the inlet [25]. In the case of the Apollo CSM radiators, during cold mission segments the working fluid stagnated, lowering the mass flow rate, which in turn lowered the rate of heat transfer. When the CSM transitioned to a relatively warmer mission segment, the mass flow rate would increase, resulting in an increased heat transfer. This variable heat transfer rate contributed to the aforementioned 3:1 turndown ratio.

However, exploiting the mass flow rate is not the only option to generate higher turndown ratios. The ISS radiators accomplish a turndown ratio greater than unity by manipulating terms found in the canonical radiative heat transfer equation, sometimes known as the *Stefan-Boltzmann*

---

[1] The effective sink temperature during PSO is calculated assuming a worst-case warm thermal environment: a mission centered around lunar noon on the equator.

relationship:

$$q = \sigma \epsilon F (T_s^4 - T_\infty^4), \tag{1.3}$$

where q represents the amount of heat rejected in Watts, σ represents the Stefan-Boltzmann constant (5.67×10^{-8} W/m^{2}K^4), ϵ is the emissivity of the radiating surface (a dimensionless quantity bounded between 0 for a perfectly reflective surface and 1 for an ideal blackbody), and F is the *radiative view factor* between the radiating surface and the surrounding environment [25]. Finally, T_s represents the temperature of the radiating surface and T_∞ represents the temperature of the surrounding environment (also referred to as the *sink temperature* [26]). Equation 1.3 is drastically simplified in the present form, but it can elucidate the general concepts that will be more thoroughly outlined later. The radiators installed on the ISS vary the heat rejection rate by varying the radiative view factor of each panel. When the panels are oriented with their normals facing the planet, the view factor is maximized, but then when the panels turn to face their edges to the sun, the view factor is minimized. The combination of changing the view factor and different thermal environments depending on whether the space station is in day or night contribute to the aforementioned turndown ratio of 3:1.

As NASA and other space agencies consider destinations farther than Low Earth Orbit, radiators that can provide a turndown ratio of greater than 3:1 are imperative. For example, the sample Altair mission profile required a turndown ratio of around 6:1 [7]. This increased requirement has led to the investigation of *variable heat rejection radiators* as a method of increasing turndown ratio [5]. The concept of a variable heat rejection radiator is not novel; in the 1980's, radiators were proposed for a nuclear-powered space station [27], heat pipe radiators were flown on multiple space shuttle missions [28], and roll-out-fin radiators were conceptualized by the United States Air Force [11]. With the Constellation and Orion programs renewing interest in long-haul manned space missions, multiple concepts have been investigated in the 21st century. Dermiryont and Moorehead proposed using electrochromic materials, in which an applied voltage results in a change in emissivity [10, 29]. Electrochromic coupons were tested in a thermal vacuum chamber and achieved a turndown ratio of 2:1, but were projected to provide a TDR of upwards of 7:1 at the full scale [30]. Digital radiators (e.g., radiator panels that could turn certain sections on or off) were benchtop tested, and projected to achieve a turndown ratio of 6:1 [9, 31]. Nagano et al. have conducted extensive research into a deployable radiator that uses a shape memory alloy (SMA) actuator to open and close louvered panels [32, 33]. The deployable radiator was thermal vacuum chamber tested and displayed encouraging thermally-activated actuation for passive heat control, producing a turndown ratio of 16:1 when sized for the Japanese Venus orbiter and high-conductivity graphite materials are integrated [12, 34]. Various efforts have focused on developing freezable radiators, including work performed by NASA that accomplished a turndown ratio of 1.8:1 [35, 36, 37]. This concept stagnates the fluid to the point of freezing, effectively reducing the heat rejection to zero in the cold state. The freezing fluid proved difficult to quickly thaw and subsequently “turn up” the radiator, which led to more holistic development of a modified stagnating radiator [38]. This derivative of the freezable radiator maintained the working fluid above the freezing point, but exploited the temperature-dependence of viscosity to lower the heat rejection rate, accomplishing a turndown ratio of 11:1 during transient operation and 6.5:1 at steady state [39]. Development has continued on the freezable radiator concept in the form of a fusible heat sink (FHS) radiator, in which a water phase change material is used to freeze around PGW fluid loops and maintain the radiator heat load at a constant 2.2 kW [40].

Additional research has been conducted into using nanoparticle solutions in the working fluid to increase the thermal properties of a fluid installed as a radiative coating, resulting in a projected turndown ratio of 1.95:1 [41]. The principles of origami have been investigated to change the emissive properties of surfaces [42], and smart materials using a mismatch in thermal expansion coefficient have been explored to actuate patterned structures and expose high emissivity surfaces when the temperature reached a certain value [43]. Finally, extensive work was completed to explore the possibility of using vanadium dioxide (VO_2) as a thermochromic (e.g., a material that changes emissivity with a change of temperature) radiative coating [44, 45, 46]. Many prototypes have been tested in thermal vacuum chambers, with the most successful coating exhibiting a turndown ratio of 4.25:1 [47].

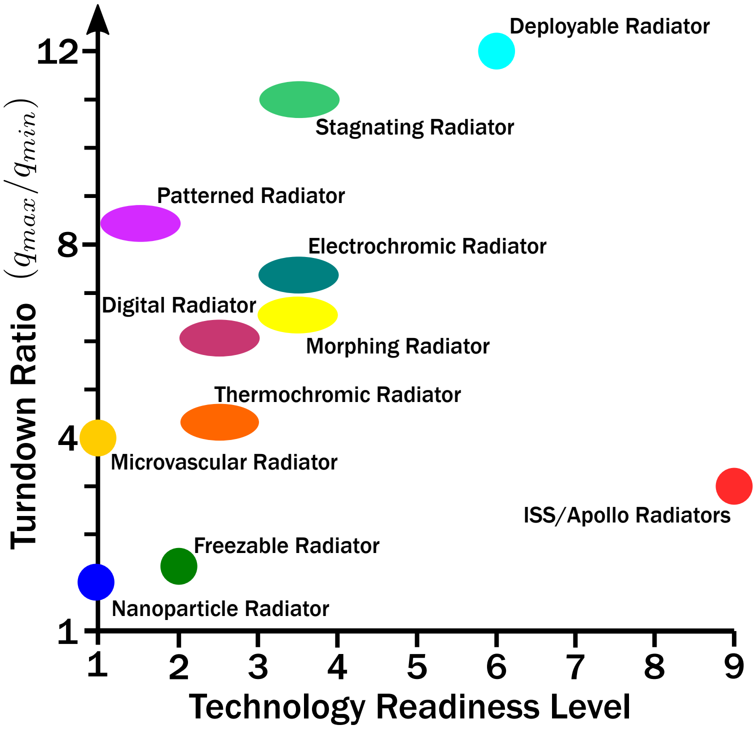

Figure 1.3: Past examples of radiator concepts, plotted in turndown ratio-technology readiness level space.

Figure 1.3 depicts all aforementioned radiator concepts plotted with respect to the experimental turndown ratio versus the system technology readiness level each design achieved. The technology readiness level (TRL) is a metric used by NASA and the DoD to quantify how close a technology is to being fully mature, e.g., able to be flown on a spacecraft. The ratings range from one, which describes a technology in which basic principles are observed, to nine, which describes an actual system that has been flown for successful mission operations. Upon inspection, only the deployable radiator developed by JAXA and Ono et al. achieved a TRL greater than four (which describes component validation in a laboratory environment). Many more technologies, including electrochromic, stagnating, and patterned radiators have performed well at low TRLs, but have not transitioned to a more advanced system. The purpose of this thesis is to improve upon the turndown ratio performance and TRL of the morphing radiator to demonstrate its viability for future long-haul space missions.

1.3 The Morphing Radiator Concept

A recently proposed design, coined a morphing radiator, accomplishes variable heat rejection through shape change driven by the actuation of shape memory alloys (SMAs) [48]. The inherent thermomechanical coupling present in SMAs makes them ideal for thermal control applications, as their responses can be tuned for specific thermal environments via manipulation of composition and processing [49]. In the morphing radiator, strategically placed SMA material is used to convert waste heat into mechanical energy, causing the radiator to change shape. In this way, the morphing radiator uses the SMAs simultaneously as mechanical actuators and thermal sensors. This novel design can achieve more than the necessary turndown ratios for future missions using a single fluid loop containing a non-toxic, high-freezing-point working fluid, potentially reducing the TCS mass by the aforementioned 23%. Due to the coupling between mechanical and thermal energy inherently present in SMAs, the morphing radiator concept can reduce the complexity of the control system overall and computational analysis has shown the potential for turndown ratios of 35:1 when multiple radiators are placed in an array [13].

The essential components of a morphing radiator include: a flow tube, which transports thermal working fluid from the spacecraft cabin to the radiator; an array of highly conductive cylindrical panels (also known as *fins*) that conduct heat away from the flow tube and subsequently radiate it to space; and SMA actuators (in wire, strip, or sheet form) attached to the outside of the conductive panels, which pull a warmer radiator open and allow a cooler radiator to close. Previous designs have included terminal blocks that act as mechanical anchors for the SMA, converting their tensile force into an applied moment and compressive force at the panel free edges (as identified in figure 1.4), but in this work bonding the SMA actuators directly onto the cylindrical panels will be investigated.

The morphing radiator functions as a high-turndown-ratio device by autonomously adapting the shape of a cylindrical radiator *fin* in response to changing conditions, enabling three mechanisms which vary the system heat rejection rate. Figure 1.5 depicts the conceptual implementation of the morphing radiator. The cylindrical panel is coated with a high-emissivity film on the inner

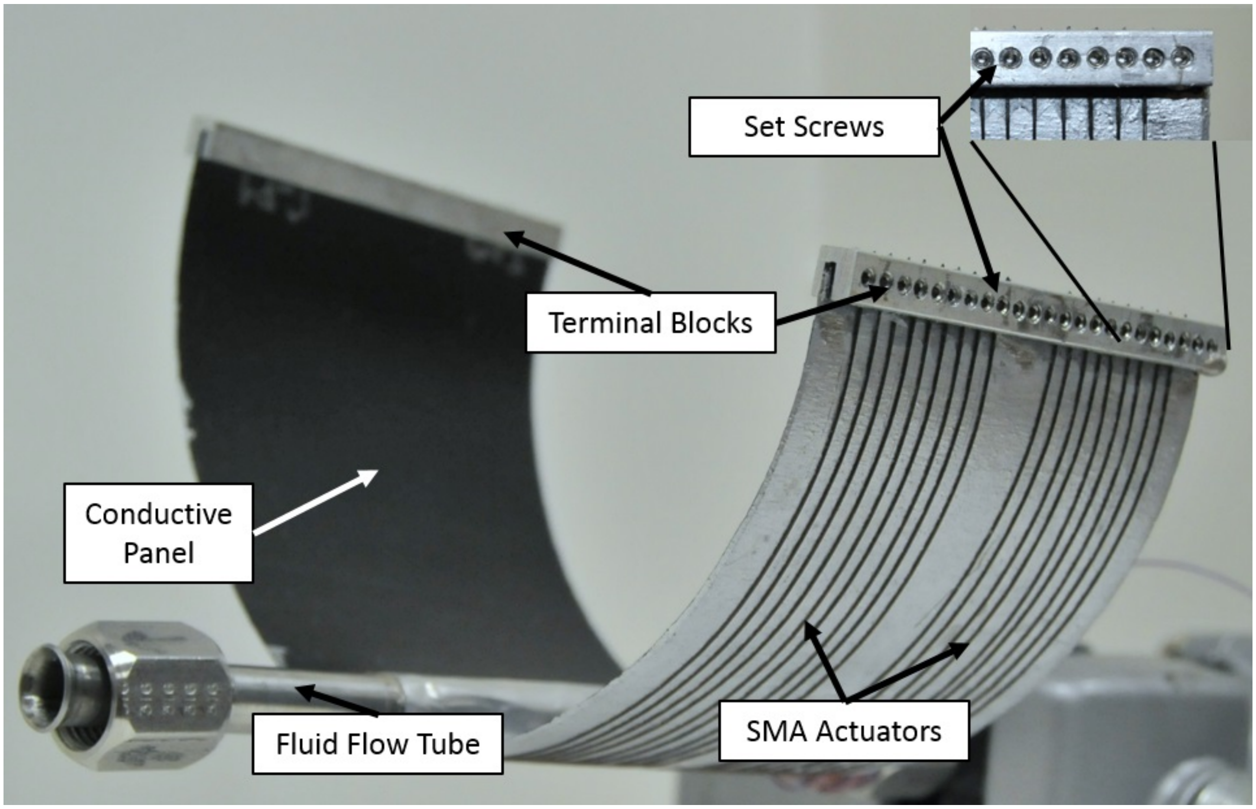

Figure 1.4: Assembly components of the Morphing Radiator concept.

(concave) surface, while the outer (convex) surface exhibits a low emissivity. During phases of the mission where external sink temperatures and internal heat loads of the spacecraft are low, the SMA actuators are fully martensitic and the morphing radiator assumes a closed cylindrical shape, blocking the high-emissivity surface and minimizing the amount of heat radiated to space. As the external sink temperature or internal heat loads increase, the SMA actuators transform into austenite and exhibit the shape memory effect, deforming the panel to resemble a semi-circular shape. This deformation exposes the high-emissivity inner surface of the radiator. The combination of an increased view factor to space and associated emissivity results in a high rate of heat rejection. Additionally, end shields are strategically installed on each circumferential end of the panel to further minimize the amount of heat rejected in the cold configuration. Past work has determined all three mechanisms (full morphing, high- and low-emissivity surfaces, and end shields) must be present in any morphing radiator prototype to provide a high turndown ratio [17].

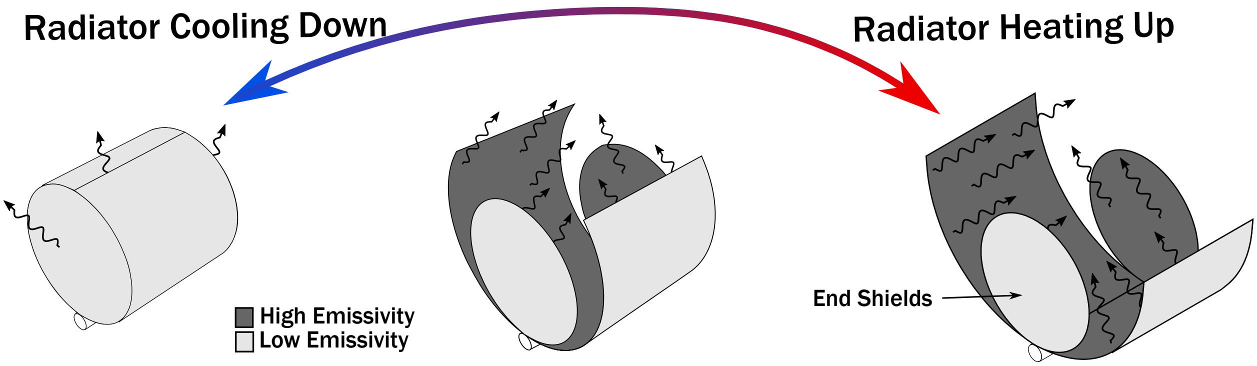

Figure 1.5: Schematic representation of the morphing radiator process. Republished with permission from [50].

1.4 Review of Adhesive Bonding of Shape Memory Alloys

Shape memory alloys (SMAs) are a class of metal that exhibit the ability to recover large amounts of strain with the application of temperature. This strain recovery is accomplished via solid-state phase change between two microstructural orientations, *martensite* and *austenite*. When the SMA temperature is above the austenite finish temperature (A_f), the molecular structure is cubic. But, as the SMA cools to the martensite start temperature (M_s), the molecular structure changes to monoclinic, which manifests itself as a strain in the material. Below the martensite finish temperature (M_f), the SMA is fully martensitic. If the SMA is once more heated to above the austenite start temperature (A_s), the strain generated begins to recover, fully recovering as the SMA reaches A_f once more. This phenomena is known as the *Shape Memory Effect* (SME) and is shown schematically in stress-strain-temperature space in figure 1.6. The SME enables SMA to be active materials, as they can transduce thermal energy into motion. SMA are very attractive candidates for many modern applications, as they are very compact, energy dense, and can recover large strains (approx. 5%) under large stresses (approx. 300 MPa) [51]. As such, SMA actuators have been used in a variety of applications, including variable geometry aircraft

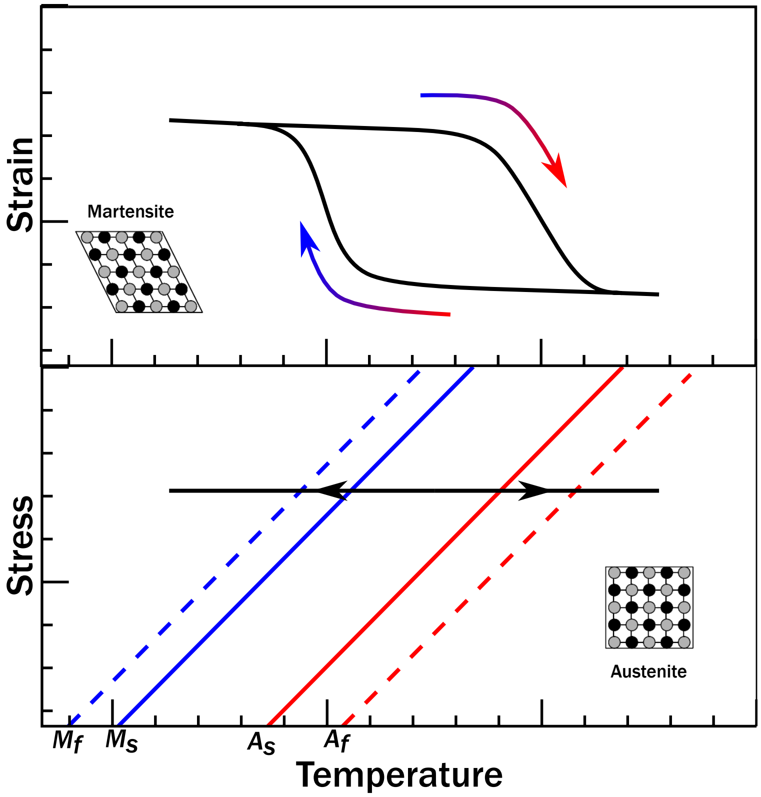

Figure 1.6: Schematic representation of the SME effect for SMA actuators and microstructures associated with each phase.

chevrons, deployable solar arrays, non-pyrotechnic separation mechanisms, and aircraft control surface actuators [52, 53, 54, 55]. However, challenges still remain with integrating SMAs and their host structures [56].

Historically, SMAs are joined with other structures via three processes: welding (i.e., fusion or solid-state), mechanical joining (via bolts, rivets, etc.), or adhesives (epoxies, etc.) [57]. Mechanical joining of SMAs is fairly simple, but can cause fatigue and corrosion in specific examples [58]. Many welding processes have been investigated, including tungsten inert gas (TIG) welding, friction stir welding (FSW), and soldering [59, 60, 61]. This section will focus on the developments in the fields of mechanically joining, adhesive bonding, or the intersection of the two as they pertain to integrating SMAs with composite structures.

Multiple research groups have investigated embedding SMA elements within composite beams to achieve shape change, vibration dampening, or increased structural rigidity [62, 63, 64]. Many of these studies included SMA wires that were integrated with the composite via the use of sleeves or sheathes [64, 65, 66]. This strategy allowed the composite to be cured separately and the wires installed afterwards to avoid transforming the wires due to high cure temperatures. Other groups focused on curing composites below the A_s of the actuator to prevent transformation [67, 68]. Finally, a large component of the existing literature focuses on using special fixtures and autoclaves to hot press the SMA-composite during cure [69, 70, 71]. This process involves prestraining the SMA before installation, and then clamping the SMA to prevent any unwanted actuation at elevated cure temperatures.

However, there is a lack of published work pertaining to the adhesive bonding of SMAs, when compared to other methods [56, 57]. This is mainly due to the challenges faced when a common SMA, nickel titanium (NiTi) is bonded with an adhesive. NiTi typically has a strong titanium oxide (TiO_2) layer, which decreases the adhesive properties of the SMA [72]. Multiple different surface treatments have been investigated to improve the bonding qualities by removing the oxide layer [73]. Surface treatments can be classified into three main groups: mechanical abrasion (such as sanding or grit blasting), acid etching (with etchants such as nitric or hydroflouric acid), or chemical treatments (such as silane or sol gel treatments). Ogisu et al., conducted rigorous studies of treating SMA foil before embedding the actuators into a carbon fiber reinforced plastic (CFRP) laminate [74]. The study considered sol gel, anodic oxidation, and acid etching and performed both peel resistance and single lap shear strength tests [75, 76]. Man and Zhao investigated the feasibility of laser gas nitriding (LGN) the NiTi surface to establish dendrite structures, and found that LGN increased the maximum shear stress up to 20 MPa [63]. Multiple studies have been conducted with pull-out tests of wires from an epoxy or polymer matrix, and some concluding that etching with hydroflouric (HF) acid increases bond strength the most [77, 78]. Smith extended the work and compared traditional surface treatments to a functionalized silane coupling agent, and found the functionalized samples performed almost 100% better [79].

As a way to avoid using highly toxic acids (such as HF), many researchers have investigated sol gel solutions to improve bonding characteristics. Sol gel is a process that involves chemical reactions that produce solid materials from small molecules. The sol is comprised of a colloidal liquid in which nanoparticles are dispersed, and the gel is a rigid structure containing microscopic pores and polymer chains. Gels can be a variety of structures from well-ordered to completely disordered [80]. The sol is fabricated by mechanically mixing colloidal particles in a water solution and placed into a mold for casting. In the mold, the sol begins to condense into the gel structure as the colloids start to establish chemical bonds. This process continues for a specified amount of time during which the gel ages and increases in strength. Finally, the gel is heated at a temperature unique to the particular composition (usually above 100°C) to remove the liquid from the gel leaving a silica gel behind on the substrate. This silica gel is instrumental in bonding to other materials, especially metals and composites, as it can create covalent bonds with the bonded material [81].

The sol gel process has been implemented, along with surface preparation, on a carbon fiber reinforced plastic (CFRP) bonded with SMA by a team at Boeing in 2010. Three classes of surface treatment were explored; chemical etching, abrasive blasting, and both etching and blasting. It was found that the abrasive blasting alone created the greatest surface roughness which is critical for insuring a consistent bond. The CFRP-SMA assembly was tested to determine the effect of the number of cycles on bond robustness and actuation magnitude, and compared to a baseline study of an SMA bolted onto an identical CFRP laminate. The deflection is far greater for the SMA bonded to the panel, and after over 1000 cycles, the bond did not show any physical signs of degradation. Additionally, Dr. Hieu Troung from Texas A&M conducted multiple studies on the interface between NiTi and Polyimide composites using Sol-gel and abrasive blasting techniques [82, 83].

1.5 Thesis Summary

The major goal of this work is to manufacture a morphing radiator prototype that is closer to flight quality hardware than previously constructed. This prototype will then be tested in a thermal vacuum chamber to simulate the relevant thermal environment encountered in space. This goal will be accomplished by building off the tools developed by previous researchers to analyze and accurately predict the performance of the morphing radiator.

1. Develop a morphing radiator design tool that considers material properties (both composite failure criteria and SMA constitutive behavior), composite stacking sequence, and SMA area fraction.

2. Investigate different methods of achieving load transfer between the SMA and composite by both adhesive bonding and mechanical fixturing.

3. Demonstrate improved turndown performance over past radiator prototypes in a relevant thermal environment and explore the possibility of experimentally measuring turndown ratio.

2. DEVELOPMENT OF AN SMA-COMPOSITE MORPHING RADIATOR DESIGN TOOL

To accurately and efficiently design a SMA-composite morphing radiator panel, a combination of numerical and analytical methods were implemented. Prior work has focused on modeling the entire prototype with high fidelity finite element analysis (FEA) [84] or approximating the composite behavior using analytic methods that do not account for SMA constitutive responses [85]. To bridge the gap between the two approaches, a design tool was formulated to more accurately predict the mechanical response of the radiator by accounting for the configuration of the SMA actuators, the constitutive behavior of the SMA candidate materials, and the SMA-composite *layup*, e.g, the number and material orientation of each composite lamina and the position of an embedded SMA actuator layer. Classical Lamination Theory (CLT) was applied to characterize the mechanical performance of embedding the SMA layer in between composite plies and varying the ratio of SMA material present on the radiator while evaluating the laminate failure criteria. Benchmarking studies were conducted with comparisons to ABAQUS FEA models to gain confidence in the predictions and understand the shortcomings of the design tool. In addition, the tool was modified to integrate with the one-dimensional SMA constitutive model to quickly analyze radiator performance due to different SMA actuator properties.

This chapter is organized as such: section 2.1 details the SMA-composite model formulation and the benchmarking study results. Section 2.2 describes the design rationale gained from the design tool for manufacturing new prototypes. Finally, section 2.3 outlines how a one-dimensional SMA constitutive model was integrated with the design tool and discusses insights gained from various test problems.

2.1 Model Formulation

In the case of the morphing radiator, the conductive panel is comprised of a cylindrical composite material. This composite consists of individual carbon fiber reinforced epoxy sheets and a sheet of SMA actuator material. These sheets are defined as individual *lamina* of the composite, and the assembly of laminae comprises the *laminate*. To accurately predict the complex load transfer between different laminae, CLT is implemented and will be discussed herein.

The design tool is formulated to approach problems in the following way. First, given material properties calculated from manufacturer data, the constitutive response of each lamina is calculated. Second, the individual laminae are assembled according to the composite *stacking sequence* (e.g., the order and relative orientation of all laminae with respect a global coordinate system) and the macromechanical response of the laminate is calculated. Last, stress analysis is performed on the laminate. Figure 2.1 depicts the design tool workflow schematically.

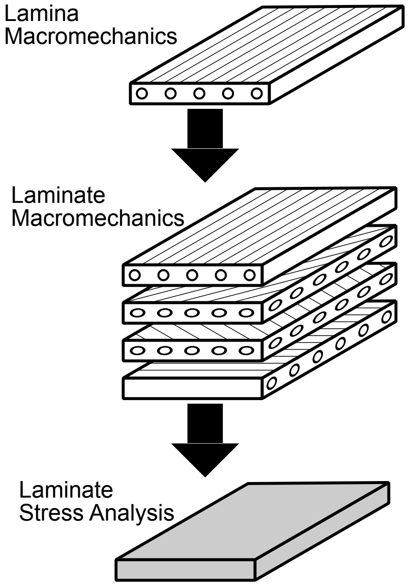

Figure 2.1: Schematic depiction of the morphing radiator design tool workflow.

Table 2.1: Composite material properties used in the design tool.

Material Property	**Mathematical Symbol**	**Value**
Longitudinal Modulus	E_1	589 GPa
Transverse Modulus	E_2	4.97 GPa
Shear Modulus	G_{12}	5.20 GPa
Poisson's Ratio	ν_{12}	0.24
Thickness	t	0.0635 mm

Table 2.2: Approximate SMA material properties.

Material Property	**Mathematical Symbol**	**Value**
Young's Modulus	E	70 GPa
Poisson's Ratio	ν_{12}	0.33
Yield Stress	σ_Y	400 MPa

2.1.1 Lamina Material Properties

The morphing radiator composite consisted of two types of lamina: pre-impregnated unidirectional carbon fiber tape, and SMA actuator material. The unidirectional pre-preg comprised of K13D2U pitch carbon fibers (produced by Mitsubishi Rayon) and RS-3C resin (produced by Tencate Advanced Composites). This material system was used in prior work, as it fulfills NASA low-outgassing requirements and exhibits a high thermal conductivity to weight ratio [85]. Material properties for the composite material are shown in table 2.1. The SMA actuator material was approximated to exhibit similar properties to isotropic aluminum and consist of a sheet equivalent in planar area to the carbon fiber sheets, but was updated as the study progressed. Approximate SMA material properties are shown in table 2.2.

2.1.2 Lamina Macromechanics

Classical Lamination Theory assumes the material is in a *plane stress* state [86]. Plane stress is valid for thin plates, and for load cases that are in the same plane as the plate. This can describe the morphing radiator, as all of the loads act in the same radial plane as the panel [87]. Mathematically, plane stress is defined as:

$$\sigma_3 = \tau_{23} = \tau_{31} = 0, \tag{2.1}$$

where σ and τ are defined as the axial and shear stresses, respectively, and the 1, 2, and 3 directions are depicted in figure 2.2.

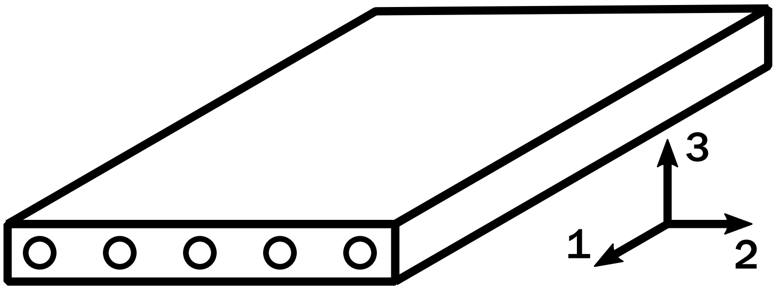

Figure 2.2: Schematic representation of the coordinate system used for plane stress in the design tool

Individual lamina stress-strain relations depend on the symmetry of the material. Metals (such as SMA), are defined as *isotropic*, which means the material exhibits the same constitutive response regardless of direction (e.g., a block of isotropic metal will feature the same stiffness if it is crushed vertically or horizontally). However, fiber reinforced composite lamina consist of stiff fibers encased by a more flexible matrix material, so the material is not isotropic. As the lamina is assumed to be in plane stress, it is assumed to exhibit *transverse isotropy*, as E_2 can be approximated to equal E_3. The stress-strain relations of an isotropic lamina in plane stress are given by:

$$\begin{bmatrix} \sigma_1 \\ \sigma_2 \\ \tau_{12} \end{bmatrix} = \begin{bmatrix} Q_{11} & Q_{12} & 0 \\ Q_{12} & Q_{11} & 0 \\ 0 & 0 & Q_{66} \end{bmatrix} \begin{bmatrix} \varepsilon_1 \\ \varepsilon_2 \\ \gamma_{12} \end{bmatrix} = [Q]\{\varepsilon\}, \tag{2.2}$$

where

$$Q_{11} = \frac{E}{1-\nu^2}, \qquad Q_{12} = \frac{\nu E}{1-\nu^2}, \qquad Q_{66} = \frac{E}{2(1+\nu)} = G, \tag{2.3}$$

and ε_1, ε_2, and γ_{12} are defined as the longitudinal, transverse, and engineering shear strain of the material. Additionally, E, ν and G are the Young's modulus, Poisson's ratio, and shear modulus.

For a transversely isotropic material, the stress-strain relations are given by the same matrix form, but different coefficients:

$$\begin{bmatrix} \sigma_1 \\ \sigma_2 \\ \tau_{12} \end{bmatrix} = \begin{bmatrix} Q_{11} & Q_{12} & 0 \\ Q_{12} & Q_{22} & 0 \\ 0 & 0 & Q_{66} \end{bmatrix} \begin{bmatrix} \varepsilon_1 \\ \varepsilon_2 \\ \gamma_{12} \end{bmatrix} = [Q]\{\varepsilon\}, \tag{2.4}$$

where

$$Q_{11} = \frac{E_1}{1-\nu_{12}\nu 21}, \qquad Q_{22} = \frac{E_2}{1-\nu_{12}\nu_{21}}, \qquad Q_{12} = \frac{\nu_{12}E_1}{1-\nu_{12}\nu_{21}}, \qquad Q_{66} = G_{12}, \tag{2.5}$$

and E_1, E_2, G_{12}, ν_{12} are defined as the longitudinal, transverse, and shear moduli, and Poisson's ratio, respectively. The reciprocal relation for Poisson's ratio is used to calculate ν_{21}:

$$\frac{\nu_{12}}{E_1} = \frac{\nu_{21}}{E_2}. \tag{2.6}$$

As orthotropic materials do not experience symmetry between the 1 and 2 directions, the material properties of a lamina will vary with respect to the angle at which the lamina is oriented to the principal axes (the 1, 2, and 3 directions in the global coordinate system). Consider a lamina undergoing positive rotation of principal material axes from x-y axes (shown in figure 2.3). To resolve the stress-strain relations from the principal axes to the x-y axes, the following equation is

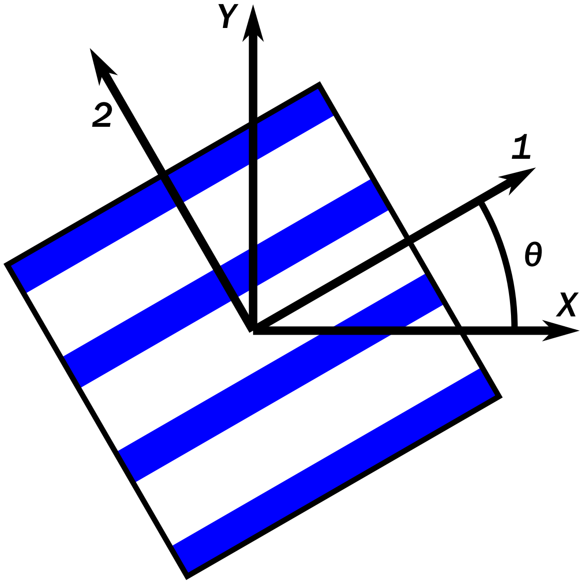

Figure 2.3: Schematic representation a fiber reinforced lamina undergoing positive rotation of principal material axes from x-y axes.

used:

$$\begin{bmatrix} \sigma_x \\ \sigma_y \\ \tau_{xy} \end{bmatrix} = [T]^{-1}[Q][R][T][R]^{-1} \begin{bmatrix} \varepsilon_x \\ \varepsilon_y \\ \gamma_{xy} \end{bmatrix} = [\bar{Q}] \begin{bmatrix} \varepsilon_x \\ \varepsilon_y \\ \gamma_{xy} \end{bmatrix}, \tag{2.7}$$

where $[T]$ and $[R]$ are defined as:

$$[T] = \begin{bmatrix} \cos^2\theta & \sin^2\theta & 2\sin\theta\cos\theta \\ \sin^2\theta & \cos^2\theta & -2\sin\theta\cos\theta \\ -\sin\theta\cos\theta & \sin\theta\cos\theta & \cos^2\theta - \sin^2\theta \end{bmatrix}, \qquad [R] = \begin{bmatrix} 1 & 0 & 0 \\ 0 & 1 & 0 \\ 0 & 0 & 2 \end{bmatrix}. \tag{2.8}$$

Using equation 2.7, each individual lamina can be resolved in a global coordinate frame (e.g., the x-y axes) and the overall mechanical properties of the laminate can be calculated.

2.1.3 Laminate Macromechanics

Once each lamina is resolved in a global coordinate frame, the mechanical response of the laminate can be calculated. The stress-strain relation of the k^{th} layer in the composite is denoted by:

$$\{\sigma\}_k = [\bar{Q}]_k \{\varepsilon\}_k, \tag{2.9}$$

where k is bounded by the number of lamina in the structure. The strain throughout the laminate can be described by:

$$\{\varepsilon\}_k = \{\varepsilon\}_0 + z\{\kappa\}, \tag{2.10}$$

where $\{\varepsilon\}_0$ defines the midplane strain of the laminate, z defines the midplane location of the lamina, and $\{\kappa\}$ describes the midplane curvature of the laminate. Figure 2.4 depicts equations 2.9 and 2.10 graphically. The force and moment resultants are then calculated for each ply. With the two resultant vectors, the overall laminate force vector $\{f\}$ can be formed by concatenating the two column vectors:

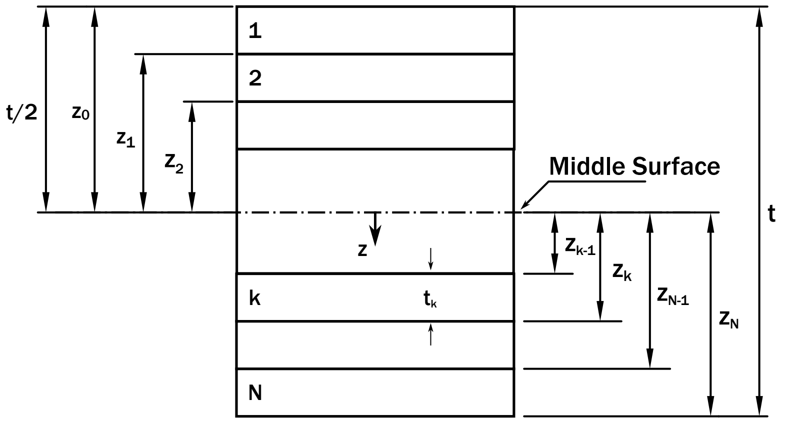

Figure 2.4: Geometry of an arbitrary laminate containing N laminae.

$$\{N\} = [\bar{Q}]_k \{\varepsilon\}_k t_{ply}, \tag{2.11}$$

$$\{M\} = \frac{1}{2}[\bar{Q}]_k \{\varepsilon\}_k t_{ply}^2, \tag{2.12}$$

$$\{f\} = \begin{bmatrix} N_x \\ N_y \\ N_{xy} \\ M_x \\ M_y \\ M_{xy} \end{bmatrix}. \tag{2.13}$$

The overall laminate stiffness matrix, also known as the *ABD matrix* and denoted Γ can be calculated by:

$$A = \sum_{k=1}^{N} [\bar{Q}]_k t_{ply}, \qquad B = \frac{1}{2} \sum_{k=1}^{N} [\bar{Q}]_k t_{ply}^2, \qquad D = \frac{1}{3} \sum_{k=1}^{N} [\bar{Q}]_k t_{ply}^3, \tag{2.14}$$

and assembled according to following relation:

$$[\Gamma] = \begin{bmatrix} A & B \\ B & D \end{bmatrix}. \tag{2.15}$$

The A, B, and D components of the matrix describe the extensional, bending-extensional coupling, and bending stiffnesses of the composites. With the ABD matrix, the constitutive response of the composite can be described:

$$\{f\} = [\Gamma]\{\varepsilon\}. \tag{2.16}$$

In the case of the morphing radiator design tool, the transformation strain in the SMA layer can be implemented:

$$\{\varepsilon\}_{SMA} = \{\varepsilon\}_0 + z\{\kappa\} - \{\varepsilon\}^t, \tag{2.17}$$

where $\{\varepsilon\}^t$ is the transformation strain in the SMA.

2.1.4 Stress Analysis and Failure Criterion

From the zero-position strains and curvatures, the overall ply stresses and strains can be calculated. These values are compared to failure criterion, first-ply fail strain for the composite laminate,

Table 2.3: Approximate composite failure properties.

Material Property	Mathematical Symbol	Value
Maximum Tensile Longitudinal Strain	$F_{0,T}$	0.29
Maximum Compressive Longitudinal Strain	$F_{0,C}$	-0.15
Maximum Tensile Transverse Strain	$F_{90,T}$	0.85
Maximum Compressive Transverse Strain	$F_{90,C}$	-1.2
Maximum Shear Strain	F_{xy}	0.75

and Von Mises stress for the SMA layer. First-ply fail strain is defined by:

$$F_{0,C} < \varepsilon_1 < F_{0,T}, \qquad F_{90,C} < \varepsilon_2 < F_{90,T}, \qquad |\gamma_{12}| < F_{xy}. \tag{2.18}$$

The strain limits of the composite material are shown in table 2.3.

2.1.5 Benchmarking Studies

To benchmark the design tool, identical laminates were analyzed in Abaqus and compared with the design tool predictions of both stress and curvature. A state of a 0.5% transformation strain in the SMA was applied to three different composite stacking sequences, and both simulations were compared with one another. Table 2.4 shows the agreement between Matlab and Abaqus, in both the overall curvature of the laminate and the principal directions of stress in the SMA layer. The laminates are denoted by the number of 0° plies embedded on the midplane (i.e., a one zero laminate has a stacking sequence of [SMA,90,45,-45,0,45,-45,90]).

Table 2.4: ABAQUS and Matlab Reconciliation

Layup	Curvature, 1/m		σ_{xx}, MPa		σ_{yy} ,MPa		σ_{xy}, MPa	
	Matlab	Abaqus	Matlab	Abaqus	Matlab	Abaqus	Matlab	Abaqus
One Zero	9.65	9.65	160.9	161.3	67.1	67.3	9.1	8.3
Two Zero	6.96	6.96	210.4	210.5	81.4	81.7	6.5	5.8
Three Zero	4.99	4.99	250.9	251.1	91.7	91.9	4.9	4.3

2.2 Morphing Radiator Design Rationale

The morphing radiator design tool allowed for quick and accurate calculations of the radiator mechanical response with respect to a variety of factors. Embedding the SMA actuator within the composite laminate was investigated as a way of increasing the heat transfer into the SMA and decreasing the required transformation strain to fully open the radiator. Further, the *Area Ratio* was introduced to approximate the mechanical behavior of the radiator if the SMA actuators were discrete strips that did not cover the entirety of the radiator convex face.

2.2.1 Investigating the possibility of embedding the SMA actuator within the composite laminate

To drive the design rationale for a bonding study, the design tool was modified to account for the possibility of embedding the SMA within the laminate. Using the laminate stacking sequence tested in FY 2016 ([90,±45,0,0,±45,90]), the mechanical response of the laminate was investigated. Figure 2.5a depicts the effect of SMA layer placement on maximum open angle, and Figure 2.5b shows the maximum open angle before failure for a laminate with the SMA bonded to the outermost layer. This tool drove the design rationale to abandon investigating embedding the SMA layer within the laminate, as all candidate designs featuring embedded SMAs failed before reaching the "full-open" baseline of 90°.

2.2.2 SMA Area Ratio Studies

The aforementioned design tool previously assumed that the SMA resembled the form of a sheet covering the entirety of the composite laminate. However, the difficulty of procuring SMA sheet as wide as the radiator and assembling a working prototype led to the exploration of the SMA-composite *area ratio* (denoted r^A). The area ratio is defined as the ratio of surface area covered by SMA to the uncovered composite surface area (e.g., the exposed area in the case that the SMA is installed in the final ply). Figure 2.6 depicts schematics of a few example area ratios, where the black and grey areas represent composite and SMA materials, respectively.

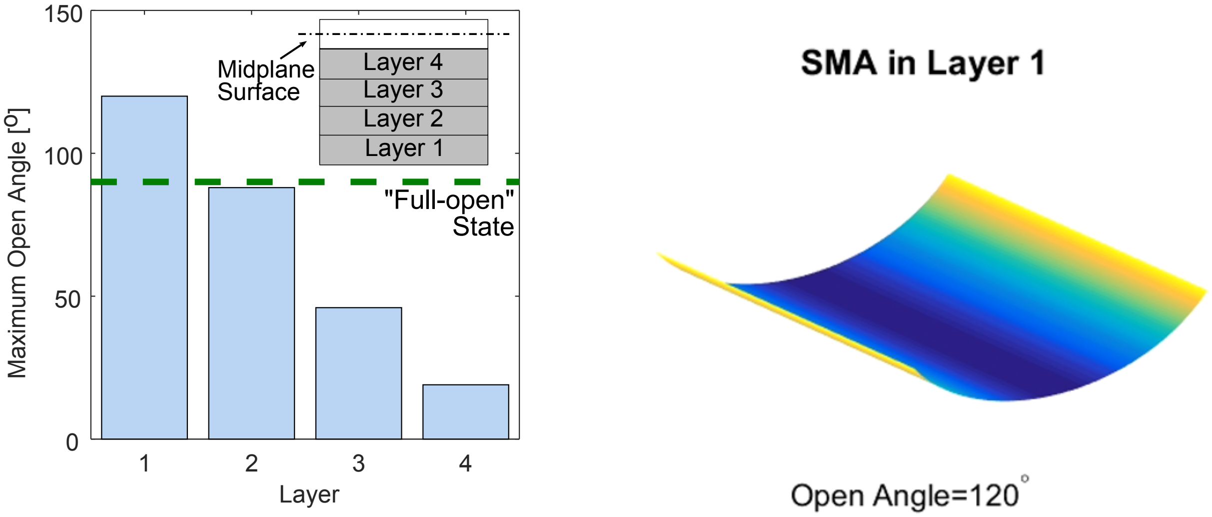

(a) Maximum open angle achieved as a function of layer in which the SMA was embedded.

(b) Maximum open angle predicted by the analytical model with the SMA on the outermost layer of the composite.

Figure 2.5: Design rationale gained and graphical representation of analytical model with the SMA as the outermost ply of composite; as only installing the SMA in the outermost ply allowed the radiator to fully open without fail, embedding the SMA was abandoned.

The area ratio is given by the following relation:

$$r^A = [r^A_{SMA} : r^A_{Comp}], \tag{2.19}$$

where r^A_{SMA} is defined as the fraction of radiator with SMA installed, and r^A_{Comp} is defined as the fraction of uncovered composite. The stiffness matrices (referred to as *ABD matrices* [86]) of both fractions of radiator are calculated following the same procedure as in section 2.1 and the literature [85]. The different stiffness matrices (denoted Γ) with their respective area ratio fractions were summed:

$$\widehat{\Gamma} = r^A_{SMA}\Gamma_{SMA} + r^A_{Comp}\Gamma_{Comp}, \tag{2.20}$$

where Γ includes the extensional, bending-extensional coupling, and bending stiffnesses of each lamina [86].

(a) 1:2 (b) 1:1 (c) 2:1 (d) 1:0

Figure 2.6: Example schematic representations of the SMA-composite area ratio. Reprinted with permission from [50].

The total force and moment resultant is calculated by:

$$\widehat{f} = r^A_{SMA} f_{SMA} + r^A_{Comp} f_{Comp}, \tag{2.21}$$

where f is defined as the force and moment resultant vector and calculated by integrating the stresses in each lamina through the composite laminate thickness. The midplane strains and curvatures (denoted $\widehat{\varepsilon_0}$) can be solved using the following constitutive equation:

$$\{\widehat{\varepsilon_0}\} = [\widehat{\Gamma}]^{-1}\{\widehat{f}\}. \tag{2.22}$$

These midplane strains and curvatures are then used to calculate the resulting geometry of the radiator. The effect of varying area ratio on resultant curvature was studied to determine the amount of SMA strips installed on the radiator prototype. Figure 2.7 depicts maximum open curvature as a function of SMA thickness and area ratio. From this analysis, an area ratio of 2:1 was targeted for the radiator prototype to ensure the highest probability of actuation without violation of material constraints.

2.3 SMA Model Integration

Previous studies with the morphing radiator design tool introduced SMA transformation strain by use of an eigenstrain analog. However, while this approach yields information about the overall mechanical performance and specific failure modes of the structure, it neglects the constitutive

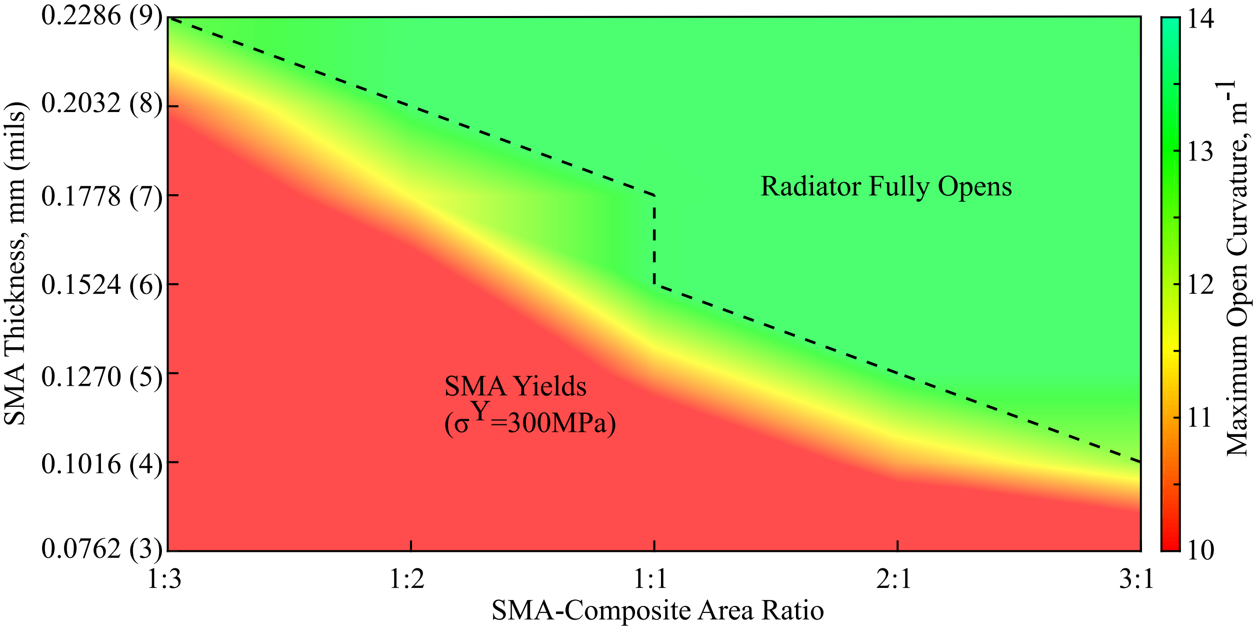

Figure 2.7: Maximum open curvature as a function of SMA thickness and SMA-composite area ratio. The black dashed line denotes the minimum thickness SMA required for full actuation. Reprinted with permission from [50].

response of the SMA actuator. To accurately predict radiator performance during thermal vacuum chamber tests, a one-dimensional SMA model was integrated into the existing design tool framework. The modified framework accounted for specific temperature cycles tested and SMA constitutive response, as derived from material characterization tests.

The SMA constitutive model implemented in this work was the Lagoudas polycrystalline model published in the International Journal of Plasticity [51]. This particular model was selected as it captures the smooth transitions in thermomechanical response during phase transformation, the variation of transformation strain magnitude as a function of applied stress, and the variation of transformation strain hysteresis as a function of applied stress. Additionally, the availability of a benchmarked one-dimensional reduction of the model allowed for quick integration into the existing morphing radiator design tool framework [88].

2.3.1 One-Dimensional Model Formulation

In one dimension, given a current temperature and strain increment, the SMA constitutive model reduces to solving fourteen scalar equations with fourteen unknowns. The stress-strain relation is given by:

$$\sigma = E(\xi)[\varepsilon - \alpha(T - T_0) - \varepsilon^t], \tag{2.23}$$

where $E(\xi)$ describes the elastic modulus of the SMA and is a function of the material *martensitic volume fraction*, calculated according to the rule of mixtures:

$$E = \left[\frac{1}{E^A} + \xi\left(\frac{1}{E^M} - \frac{1}{E^A}\right)\right]^{-1} \tag{2.24}$$

In equation 2.24, E^A and E^M describe the austenitic and martensitic elastic moduli, respectively. The evolution equation of transformation strain is given by:

$$\dot{\varepsilon^t} = \dot{\xi}\Lambda^t, \quad \Lambda^t = \begin{cases} H_{cur}\text{sgn}(\sigma) & \text{if } \dot{\xi} > 0 \\ \varepsilon^{t-r}/\xi^r & \text{if } \dot{\xi} < 0 \end{cases}, \tag{2.25}$$

where Λ^t denotes the direction of transformation (e.g., either forward or backward), H_{cur} describes the current maximum transformation strain, ε^{t-r} is defined by macroscopic transformation strain at reversal, and ξ^r denotes the martensitic volume fraction at reversal. Evolution of hardening energy during forward transformation is defined as:

$$\Phi^t_{fwd}(\sigma, T, \xi) = (1 - D)|\sigma|H_{cur}(\sigma) + \frac{1}{2}(\frac{1}{E^M} - \frac{1}{E^A})\sigma^2 + \rho\Delta S_0 T - \rho\Delta U_0 - f^t_{fwd}(\xi) - Y^t_0 = 0, \tag{2.26}$$

while the evolution of hardening energy during reverse transformation is described by:

$$\Phi^t_{rev}(\sigma, T, \xi) = -(1+D)\sigma\frac{\varepsilon^{t-r}}{\xi^r} - \frac{1}{2}(\frac{1}{E^M} - \frac{1}{E^A})\sigma^2 - \rho\Delta S_0 T + \rho\Delta U_0 + f^t_{rev}(\xi) - Y^t_0 = 0. \tag{2.27}$$

In the two preceding equations, ρ is defined as the material density, ΔS_0 and ΔU_0 are the changes in entropy and internal energy, respectively, f^t_{fwd} and f^t_{rev} are the forward and reverse *hardening functions* and define the current transformation hardening behavior, and Y^t_0 and D are model parameters.

From these five equations, the following parameters can be calibrated to fit the specific SMA material response:

1. Thermoelastic constants, E^M, E^A, ν^M, ν^A, and α.
2. Maximum transformation strain, $H_{cur}(\sigma)$, which is fit to an exponential decay function of the form:

   $$H_{cur}(\sigma) = \begin{cases} H_{min}; \quad \text{if} \quad \sigma \leq \sigma_{crit}, \\ H_{min} + (H_{sat} - H_{min})(1 - e^{-k(\sigma - \sigma_{crit})}); \quad \text{if} \quad \sigma \geq \sigma_{crit}. \end{cases} \tag{2.28}$$

   The terms H_{min} and H_{sat} describe the minimum and saturation transformation strain, respectively, σ_{crit} denotes the critical stress at which transformation strain manifests, and k is a constant fitted from experimental data [52].
3. Model Parameters $\rho\Delta S_0$, $\rho\Delta U_0$, a_1, a_2, a_3, Y^t_0, and D.

With these parameters calibrated, the one-dimensional SMA constitutive response can be predicted and integrated into the morphing radiator design tool.

2.3.2 SMA Model Integration

The integrated model calculates the equilibrium state of the SMA-composite system as it evolves with temperature, which is crucial to capture the nonlinear behavior of SMA materials. Figure 2.8 is a flowchart that outlines the implementation of the laminated plate theory model integrated with the SMA model. The model is initialized by calculating the SMA prestress required to maintain the radiator in a fully open (semicircular) configuration through force equilibrium. This

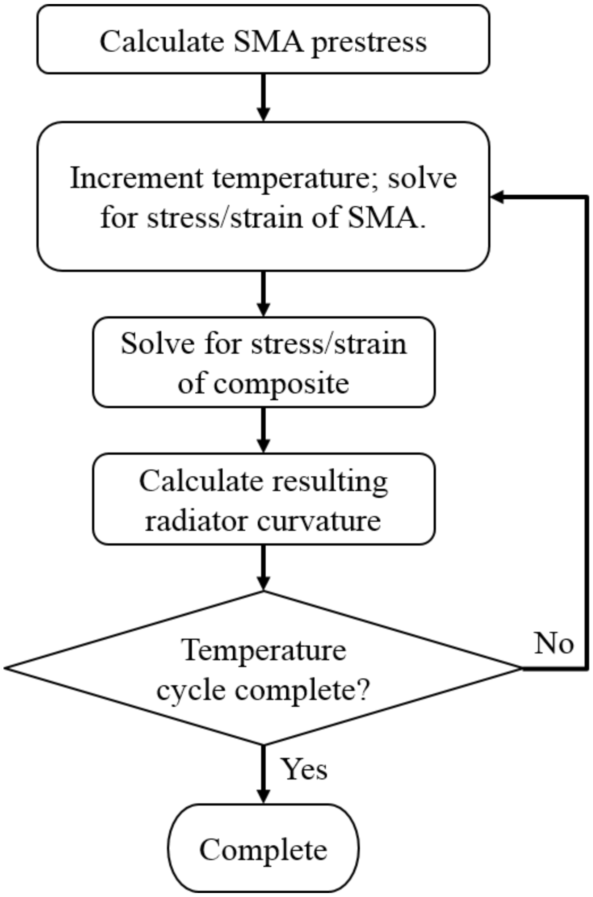

Figure 2.8: Flowchart detailing SMA model integration with laminated plate theory model.

prestress amount was calculated to be roughly 250 MPa, and was used in the fabrication of the prototypes. Following the prestress step, the model increments through the temperature cycle, solving the SMA constitutive equations and composite constitutive equations sequentially. After determining the stress-strain state of the radiator assembly, the model calculates the resulting curvature of an equivalent radiator prototype and increments temperature until completion. Although this is a low-fidelity approximation given the complex behavior of the radiator, the model allows for quick mechanical calculations that would otherwise require orders of magnitude longer runtimes with full three-dimensional constitutive models implemented into finite element frameworks.

2.3.3 Demonstration of the SMA-Composite Morphing Radiator Design Tool

The design tool with SMA model integrated was demonstrated using two different SMA materials to illustrate the utility of the tool and gain insights on the SMA-composite system. Two SMA materials were selected because they were both tested in Thermal Vacuum Chambers at NASA Johnson Space Center, detailed in section 4. Experimental temperature cycles were mirrored in the design tool framework, and the mechanical response of the radiator was predicted. The two SMA materials selected were a binary NiTi (e.g., equiatomic nickel and titanium) strip, of thickness 0.2032 mm (8 mils), and a cobalt alloy strip, of thickness 0.1270 mm (5 mils). Each morphing radiator prototype exhibited an area ratio of 2:1 with each strip measuring approximately 8 mm in width. The complete characterization data for both SMA specimens can be found in appendix A.

2.3.3.1 0.2032 mm NiTi strip tests

The NiTi strip was procured by Dr. Othmane Benafan of NASA Glenn Research Center. Figure 2.9a depicts the approximate phase diagram for the SMA (assuming constant slope transformation surfaces), as derived from multiple isobaric tensile tests (shown as the discrete data points). The shaded green rectangle indicates the operational envelope of the thermal vacuum chamber. The solid black path represents an approximate actuation cycle for a radiator assembled with this material, while the dashed black path represents the ideal actuation cycle with no regard for the testing temperature range. The ideal actuation cycle trends to a state of zero stress when the SMA is fully transformed due to the zero-stress state of the composite facesheet. When the radiator is fully closed, the entire system (SMA and composite facesheet) must be in a zero-stress state to satisfy equilibrium. The red circle illustrates that this material was not well-suited for thermal vacuum chamber testing, as the SMA would not be capable of transforming completely before the lower chamber temperature limit of -45°C was reached. The lack of complete transformation was demonstrated during thermal vacuum chamber tests and preliminary thermal chamber tests at Texas A&M University[1].

---

[1] Trade names and trademarks are used in this report for identification only. Their usage does not constitute an official endorsement, either expressed or implied, by the National Aeronautics and Space Administration.

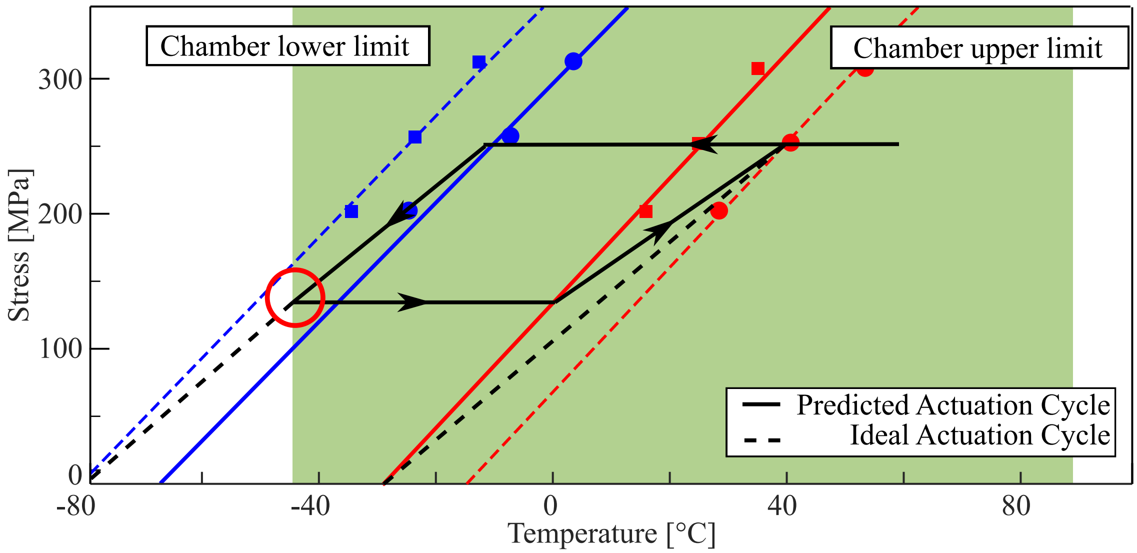

(a) Experimental phase diagram with expected actuation cycle (solid line) superimposed. Full actuation during cooling (i.e., closing) was not expected given thermal chamber operational constraints.

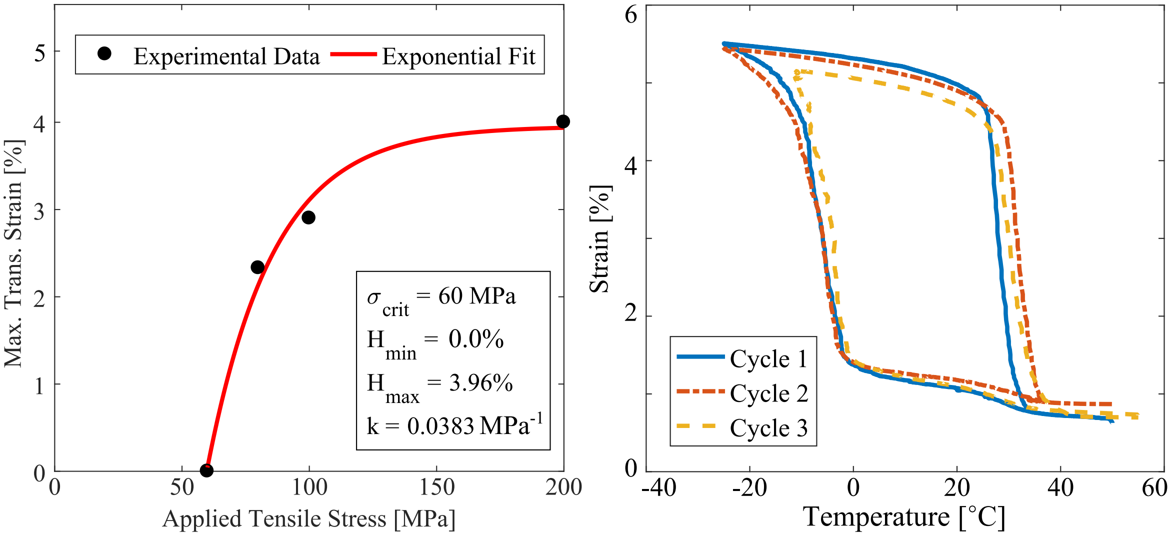

(b) Maximum transformation strain as a function of applied tensile stress.

(c) Constant force thermal training cycles at 200 MPa.

Figure 2.9: Characterization data for the 0.2032 mm thick SMA strip used in thermal vacuum chamber testing. Reprinted with permission from [50].

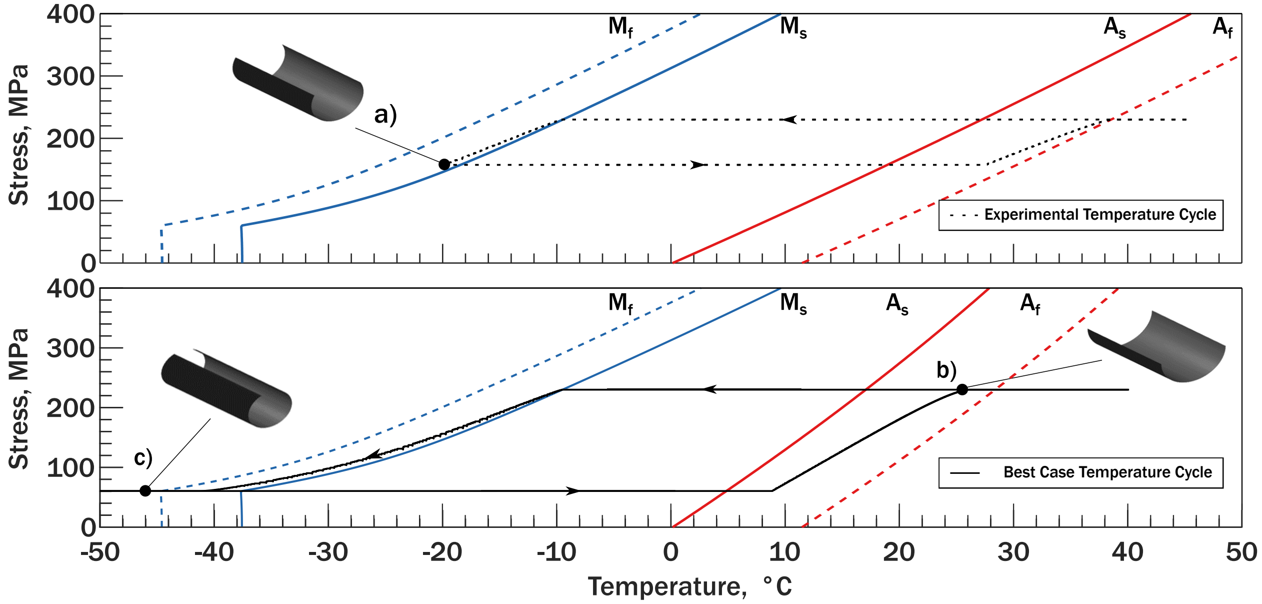

Figure 2.10: Stress-temperature cycles, as predicted by the composite-SMA model. Note that the reverse transformation surfaces vary as a function of the transformation strain at reversal.

Figure 2.9b depicts $H^{cur}(\sigma)$ for the material, and it can be seen that the SMA exhibited a high σ_{crit} (defined as the stress state at which transformation does not produce actuation strain), which inhibited full closure of the radiator regardless of the temperature.

Furthermore, the material exhibited excellent cyclic stability, which is defined as the amount of recoverable strain generated during cyclic loading. Three isobaric training cycles at 200 MPa are shown in Figure 2.9c, demonstrating small amounts of irrecoverable strain measured from cycle to cycle. This material stability decreased the time required to fully train a strip, but the lack of training resulted in no two-way (i.e., stress-free) transformation strain.

Figure 2.10 depicts the SMA phase diagram and the temperature-stress cycle of the morphing radiator as predicted by the SMA-composite model for the same temperature cycle as tested (assuming thermal homogeneity). Incomplete transformation to martensite is observed in both the experiment and model predictions at the lower limit of the temperature cycle (Figure 2.10, state a). Additionally, full recovery is shown at the upper limit of the temperature cycle (Figure 2.10, state b). The performance of the radiator can also be assessed if the fluid temperature had been cycled from 50°C to -50°C (the best case, shown as the dashed line of Figure 2.10). Although the radiator actuates significantly more towards full closure, the model still predicts incomplete actuation for a temperature of -50°C due to the lack of two-way transformation strain generation in the SMA material (Figure 2.10, state c).

These results indicate the importance of a multitude of SMA properties, not just the presence of correct transformation temperatures. To produce a morphing radiator that actuates fully, the SMA actuators must exhibit transformation temperatures between -50°C and 50°C and *two-way shape memory effect*[2] to fully close the radiator and thus provide maximum turndown performance. Previous efforts have only considered the maximum transformation strain H_{sat}, but the design tool illustrates the necessity of considering the evolution of transformation strain as a function of applied stress. This consideration is only possible with thorough characterization of the SMA material throughout the entire operating range.

2.3.3.2 0.1270 mm cobalt strip tests

The 0.1270 mm cobalt strips were procured by Dr. Othmane Benafan, and underwent multiple heat treatments to tune the transformation temperatures for the morphing radiator application. Figure 2.11 illustrates the effect of the heat treatments and the ability of the researchers at Glenn Research to shift transformation temperatures to better fit a particular mission profile. Figure 2.11a depicts the zero-stress transformation temperatures before heat treatment, and features a distinct R-phase. After heat treatment, the hysteresis was tightened, but the austenite finish temperature had the potential of prohibiting the radiator from fully opening at high stresses. To remedy this, a final round of annealing was conducted to attempt to shift the transformation temperatures down 20°C.

The final cobalt material exhibits a zero-stress transformation temperature of -61°C, which was slightly under the thermal vacuum chamber limits. However, as the material features a very tight hysteresis, the transformation temperatures do not approach the upper temperature limit of

---

[2] The two-way shape memory effect is defined as the ability of an SMA actuator to exhibit repeatable shape change under no applied stress.

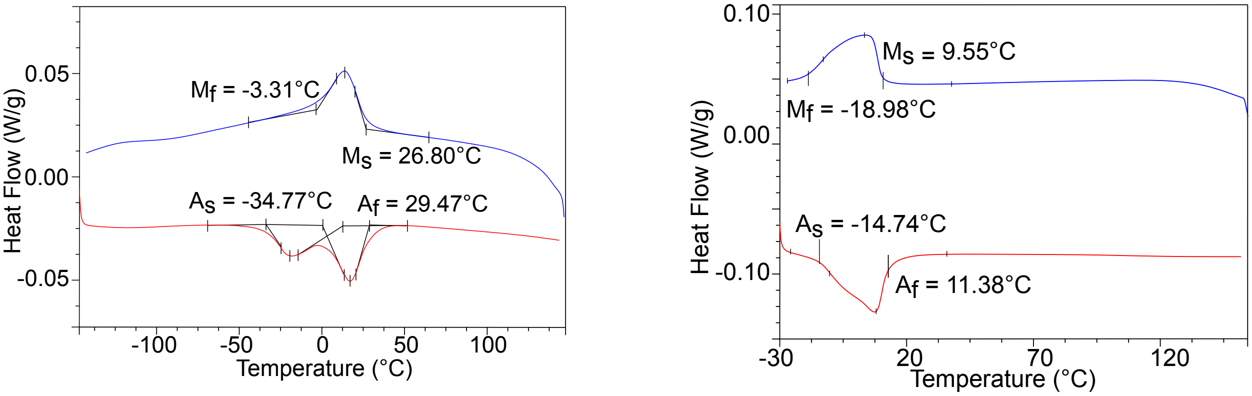

(a) Before heat treatment

(b) After heat treatment

Figure 2.11: Differential Scanning Calorimetry of the NiTiCo, highlighting the effect of heat treatment on transformation temperatures

the thermal vacuum chamber within the predicted stress range of the radiator. Complete SMA characterization data is provided in appendix A.

Furthermore, the material exhibits a much lower σ_{crit} (as shown in Figure 2.12a, which is encouraging for thermal vacuum chamber testing. The evolution of maximum transformation strain (H^{cur}) as a function of applied tensile stress, as well as the related isobaric actuation cycles are shown in Figure 2.12. Although the last round of annealing removed most stability from this material, sufficient training was accomplished in 15 isobaric cycles.

The design tool was implemented to predict the radiator performance until a thermal cycle with the 0.1270 mm thick cobalt strips. The complete stress-temperature cycle is depicted in figure 2.13. Even without the presence of two-way shape memory effect, it can be seen that the radiator fully closes upon SMA transformation (state b)), and fully reopens upon heating (state a). Additionally, as the SMA actuators exhibit sufficient transformation strain at low applied stresses (contrary to the 0.2032 mm strip), the radiator closes well before the zero-stress martensite finish temperature. This early actuation may be a result of the material exhibiting more transformation strain than necessary to fully close the radiator, as only slightly more the 1% strain is needed, and at low stresses (under 50 MPa) the SMA transforms up to 3.5%.

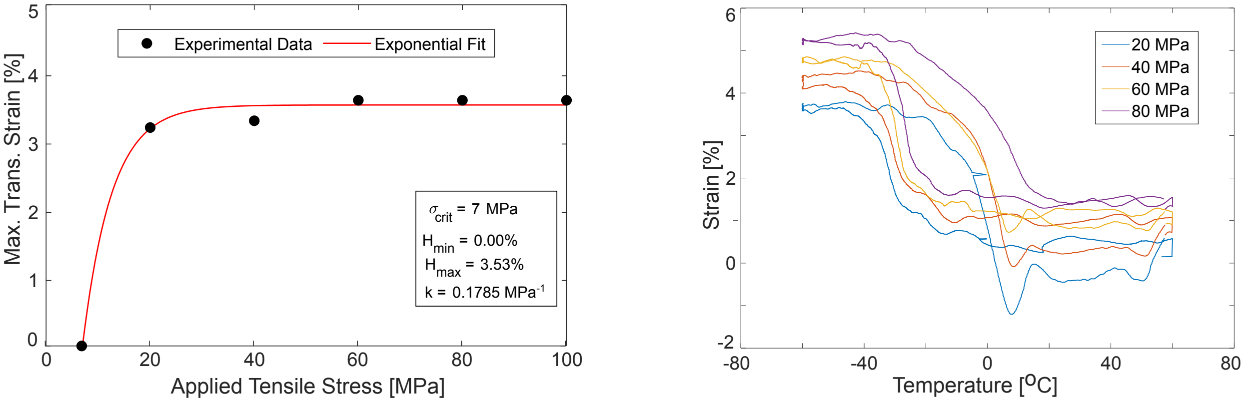

(a) Maximum transformation strain as a function of applied tensile stress.

(b) Constant force thermal cycles for actuation characterization.

Figure 2.12: Additional characterization data for the 0.1270 mm thick NiTiCo

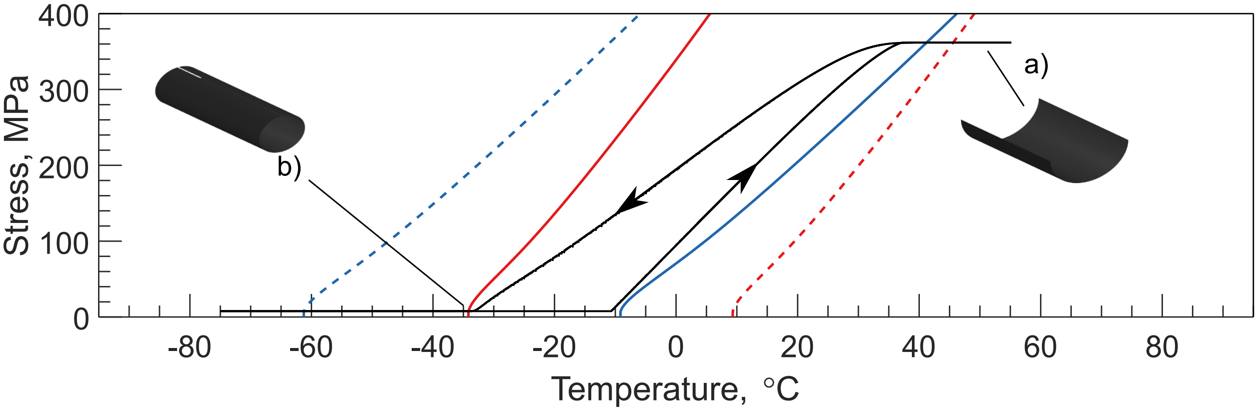

Figure 2.13: Stress-temperature cycle of the 0.1270 mm cobalt strip, as predicted by the composite-SMA model.

2.4 Conclusions

In this chapter, a SMA-composite morphing radiator design tool was presented and multiple test cases were analyzed, demonstrating the utility of the tool to predict the mechanical performance of the morphing radiator in response to thermal cycles. The design tool was derived from classical plate theory and integrated with a one-dimensional SMA constitutive model to capture the thermomechanical response of the SMA actuators. Predictions from the design tool were benchmarked against commercial finite element solvers, and used to inform the thickness and area ratio of the SMA strips installed on tested prototypes. Finally, the integrated constitutive model provided insight into the complex SMA-composite interaction during thermal cycles and illustrated the need for sufficient transformation strain at low applied stresses.

3. BONDING AND MECHANICAL FIXTURING TRADE STUDY

3.1 Chapter Outline

One goal of this work was to explore the viability of bonding the shape memory alloy (SMA) actuator with the composite laminate. This was investigated because a bonded actuator would reduce the complexity and weight of the morphing radiator compared to a mechanically fixed subsystem. Additionally, bonding could potentially decrease the required actuation strain to fully open the radiator from a closed cylindrical shape to a semicircle, as the actuation strain would be more localized around the entirety of the radiator instead of merely fixed at each circumferential end. The study was organized as such:

1. A surface treatment study to compare different methods of pretreating the SMA actuator.
2. First order shear lag calculations to gain an understanding of the stress distribution in a bond if the SMA was adhesively bonded to the outermost composite ply.
3. Candidate epoxy selection.
4. Isothermal single lap shear bond tests of SMA-composite bonds.
5. Coupon-level tests of SMA-composite bonds under actuation loads with straight and cylindrical curved specimens.

These steps informed the manufacturing methods implemented on the prototypes tested in thermal vacuum chambers, and represent a thorough investigation of alternative options to mechanically fixing the SMA actuators onto the prototype.

3.2 Surface Treatment Study

Preliminary tests indicated the need for a comprehensive understanding of available surface treatments, as most test articles failed in the adhesive regime (close to 100% of the epoxy on one substrate after failure). Additionally, after discussing with Dr. Hieu Troung (Texas A&M

Class of 2016, Mechanical Engineering), primary surface treatments were applied to the SMA before application of the sol gel. These primary surface treatments can be broken into two groups: mechanical abrasion and acid etching. Both treatments are intended to remove the oxide layer from the NiTi surface.

3.2.1 Mechanical Abrasion Experiment

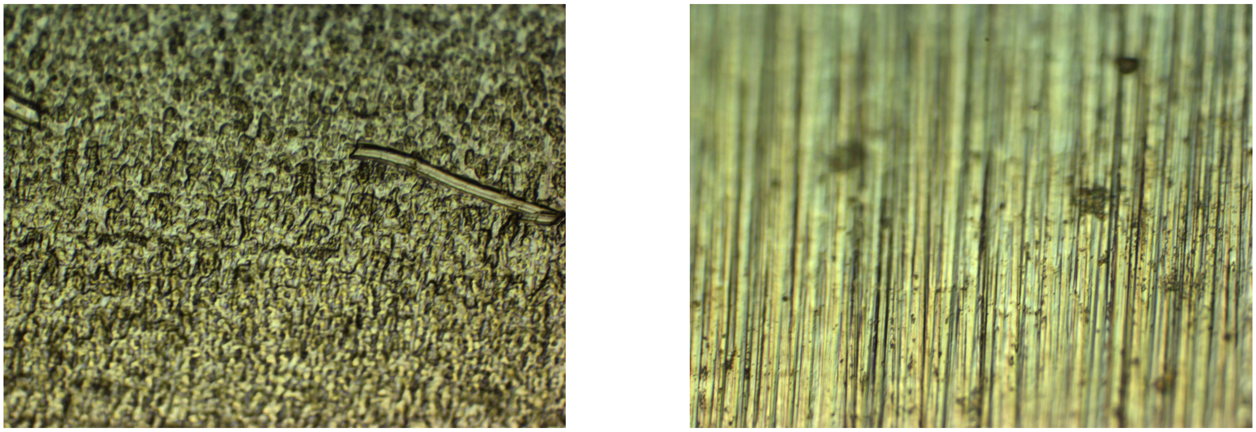

(a) No Surface Treatment

(b) Mechanical Abrasion

Figure 3.1: Comparison between SMA material with and without mechanical abrasion.

Mechanical abrasion is defined as using a rough medium (sand, grit, diamond) to remove material from a surface, and is used in many industries to prepare surfaces for adhesive bonding. The surface of the SMA was first mechanically abraded using a powered hand tool with a sanding disk. However, it was discovered that the high rotational speed of the tool was locally transforming the SMA from detwinned martensite to austenite and causing plastic deformations, known as peening [89]. To avoid altering the material unfavorably, hand sanding with fine grit Scotch Brite was used to remove the oxide layer. Figure 3.1 depicts an optical microscopy image of the SMA treated with Scotch Brite abrasion compared to an untreated sample. Note the ordered striations of the material due to the mechanical abrasion; this may be due to the directionality of the hand sanding. From this study, it was found that using powered hand tools locally transformed and potentially plasticly deformed the SMA, but using Scotch Brite by hand produced noticeable differences in surface quality.

3.2.2 Acid Etching

Acid etching is a process in which an acidic solution (sometimes referred to as a *pickle*) is used to remove oxide layers or other contaminants from metal surfaces [90]. There are numerous examples in the literature that explore the effects of acid etching on NiTi[77, 91, 56]. However, the majority considers hydroflouric acid (HF) as the active reagent; due to the hazardous nature of HF, alternative methods using nitric acid (NO_3) were investigated. The etching pickle contained the following:

1. 1 Part Hydrochloride (Solid Form of Hydrochloric Acid)
2. 3 Parts Nitric Acid

This solution was used in the following procedure:

1. Immerse SMA specimen in pickle for 180-300 s at 80°C.
2. Rinse with distilled water.
3. Oven dry for 15 minutes at 90°C

Figure 3.2 shows optical microscopy images for acid etches of duration 0 s, 180 s, and 350 s. It is shown that the duration of the etch was not sufficient to impart noticeable change on the material. It is advised to use a much stronger pickle to explore the changes in surface quality more thoroughly, however due to the hazardous nature of such acids, sol gel was investigated in more detail.

3.3 First-order shear stress calculations

To select candidate epoxies, a rudimentary shear lag analysis of the bond was conducted. Shear lag is an approximation method for determining the stress distribution in a bond. Most shear lag methods approximate a single-lap joint, whereas the bond between the SMA and composite on

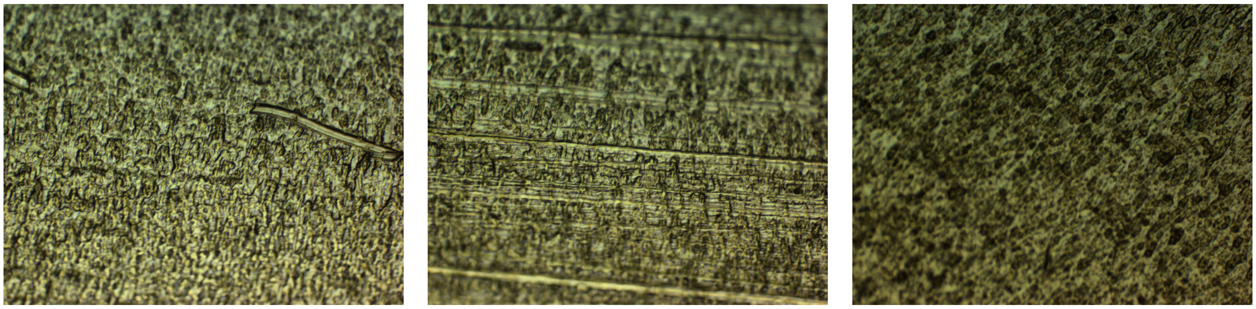

(a) No Acid Etching (b) 180 second etch (c) 350 second etch

Figure 3.2: Comparison between SMA material with no acid etching and two different etch durations. Etching for 350 seconds showed no difference in the surface quality.

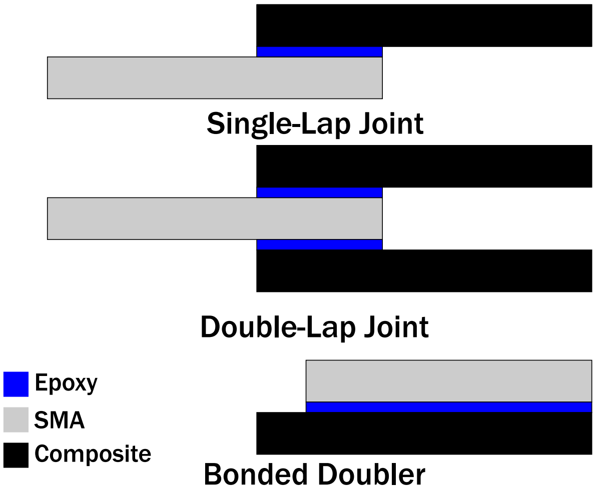

Figure 3.3: Common Bond Types

the morphing radiator is more accurately described as a bonded doubler [92]. However, Volkerson's method, arguably the simplest analysis method for shear lag, models a double lap joint [93]. Double-lap joints closely resemble the behavior of bonded doubler joints in shear, hence Volkerson's method was selcted for this analysis. Figure 3.3 shows the various geometric configurations for the three bond types discussed.

3.3.0.1 Volkerson's Analysis

While Volkerson's Analysis is one of the oldest methods (first published in 1938) for describing adhesive joint behavior, it is quite accurate for certain cases. Additionally, the analysis accounts for

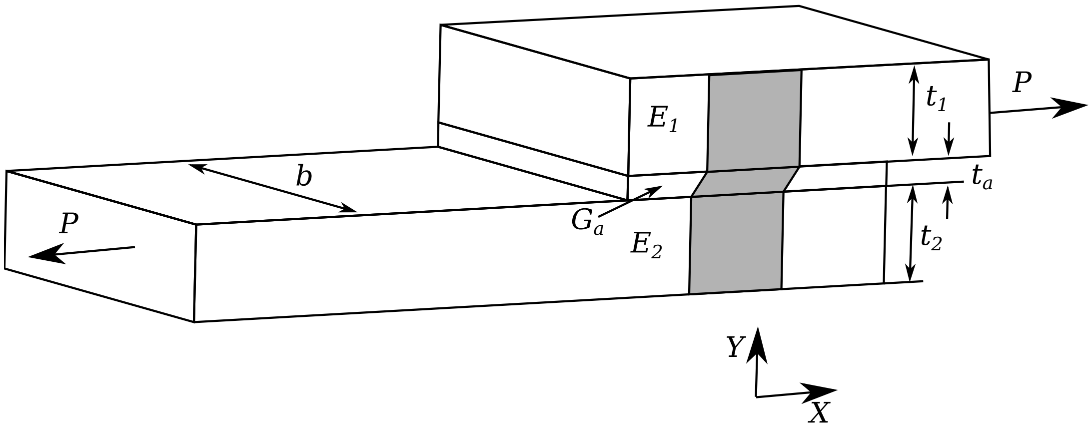

Figure 3.4: Sample Bond Geometry for Volkerson's Method

deformable adherends as well as dissimilar adherend thicknesses and materials. The shear stress distribution for a bond of length l is given by

$$\tau = \frac{P}{bl}\frac{w}{2}\frac{\cosh wX}{\sinh \frac{w}{2}} + \frac{t_1 - t_2}{t_1 + t_2}\frac{w}{2}\frac{\sinh wX}{\cosh \frac{w}{2}}. \tag{3.1}$$

Where w is a constant specific to bond properties and dimensions, given by

$$w = \sqrt{\frac{G_a l^2}{E_a t_1 t_a}(1 + \frac{t_1}{t_2})}, \tag{3.2}$$

and X is the normalized length along the bond, described by

$$X = \frac{x}{l}, -0.5 \leq X \leq 0.5. \tag{3.3}$$

The bond strength was calculated using nominal properties for the adhesive, as well as the actual geometry of the morphing radiator. Figure 3.5 shows the calculated shear stress distribution as a function of length along the panel. It is evident that the shear stress will be concentrated in each extreme of the bond. This observation agrees with previous qualitative tests, as every bond failed at the end of the SMA-composite assembly with respect to actuation direction. Volkerson's

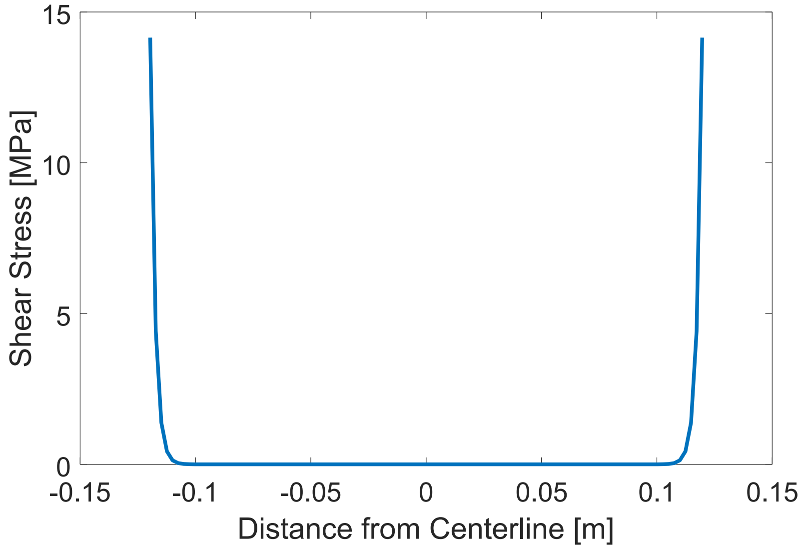

Figure 3.5: Shear Stress Distribution using Volkerson's Analysis

analysis also provided a benchmark shear stress of 13 MPa that the radiator bond must withstand. This benchmark value was taken into account when selecting candidate epoxies.

3.4 Candidate Epoxy Selection

An ideal epoxy for the morphing radiator is compliant in bending, capable of withstanding 13 MPa of shear stress, curable at room temperature, and compliant with NASA outgassing standards. From these criterion and knowledge gained from prior experiments, three candidate epoxies were selected: Henkel Hysol Loctite 9309.3NA, 3M Scotchweld EC 2216 B/A, and Arctic Silver Thermal Epoxy [94, 95, 96]. Both the Loctite 9309.3NA and Scotchweld EC 2216 B/A exhibit exceptional characteristics in peel and shear; the 9309.3 NA performs slightly better in both categories but is also less ductile, which could influence its ability to maintain a bond over the entire actuation of the radiator. Arctic Silver was selected as a baseline epoxy with which to compare the performance of the Loctite and Scotchweld, as it was used in previous experiments to secure thermocouples to the prototype. Moving forward, it is important to note the inherent balance between resistance to peel and shear: an ideal epoxy in shear will be highly vulnerable to failure in peel.

Table 3.1: Reported Material Properties for Candidate Epoxies

Epoxy	Lap Shear Strength	T-Peel Strength	Cure Time
Loctite EA 9309.3 NA	32 MPa	5.6 N/mm	3 days
ScotchWeld 2216 B/A	21 MPa	4.4 N/mm	7 days
Arctic Silver Thermal Epoxy	Not Reported	Not Reported	1 day

3.5 Lap Shear Bond Tests

To gain an understanding of how different surface treatments affect bond strength, lap shear tests were performed on a variety of specimens. Lap shear bond tests measure the ability of the epoxy to withstand shear stresses. These tests were based on ASTM Standard D1002 procedure, adapted to a composite-SMA bonded joint [75]. The experimental setup consisted of a bonded SMA-composite strip that was placed in MTS load frame grips and loaded in tension until failure. The maximum load at failure was recorded, and the maximum shear stress of each specimen was calculated using the following equation:

$$\sigma_{max} = \frac{F_{max}}{w * L}, \tag{3.4}$$

where w and L are the width and length of the bonded area. The width of each bond was determined by the width of both strips, while the length was determined from calculating the maximum permissible bond length as specified in ASTM D1002. The maximum permissible bond length is given by the following relationship:

$$L = \frac{\sigma_Y t}{\tau}, \tag{3.5}$$

where σ_Y is defined as the yield stress of the substrate, t is the substrate thickness, and τ is the approximate maximum shear stress of the epoxy. Figure 3.6 depicts a schematic representation of the lap shear test specimen compared to a specimen installed in the MTS load frame. A number of modifications were made to the testing procedure to accommodate a variety of factors. First, even though ASTM D1002 specifies a nominal specimen width of 25.4 mm, tested specimens were

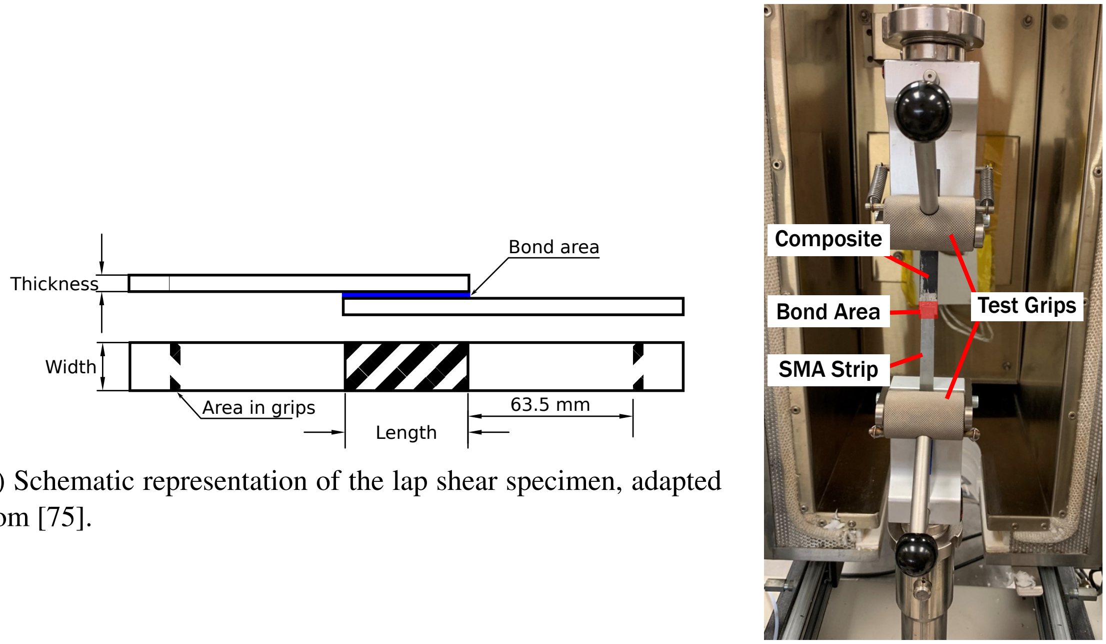

(a) Schematic representation of the lap shear specimen, adapted from [75].

(b) Physical geometry of the specimen installed in the load frame.

Figure 3.6: Schematic representation and physical geometry of the lap shear bond tests.

cut to a nominal width of 8 mm due to SMA material availability. Second, the nominal thickness reported in the standard is 1.6 mm, but changed to 0.20 mm for the current tests. Last, the standard calls for 25.4 mm of material installed in the load frame grips, but available hardware only allowed for the material to be gripped by knurled cylindrical strip grips (depicted in figure 3.6b.

3.5.1 Lap Shear Test Matrix

To identify the potential performance benefits of different epoxies and surface treatments, a full factorial test matrix was constructed (depicted in figure 3.7). The three aforementioned candidate epoxies were tested with three distinct surface treatments each, referred to as solvent rinse, abrasion, and sol gel. However, it must be noted that the abrasion surface treatment also included solvent rinses, and the sol gel treatment included both abrasion and solvent rinses. This was to compare the potential additive effect of surface treatments. Maximum failure shear stress and failure mode of each specimen was recorded, and provided a qualitative and quantitative measure of

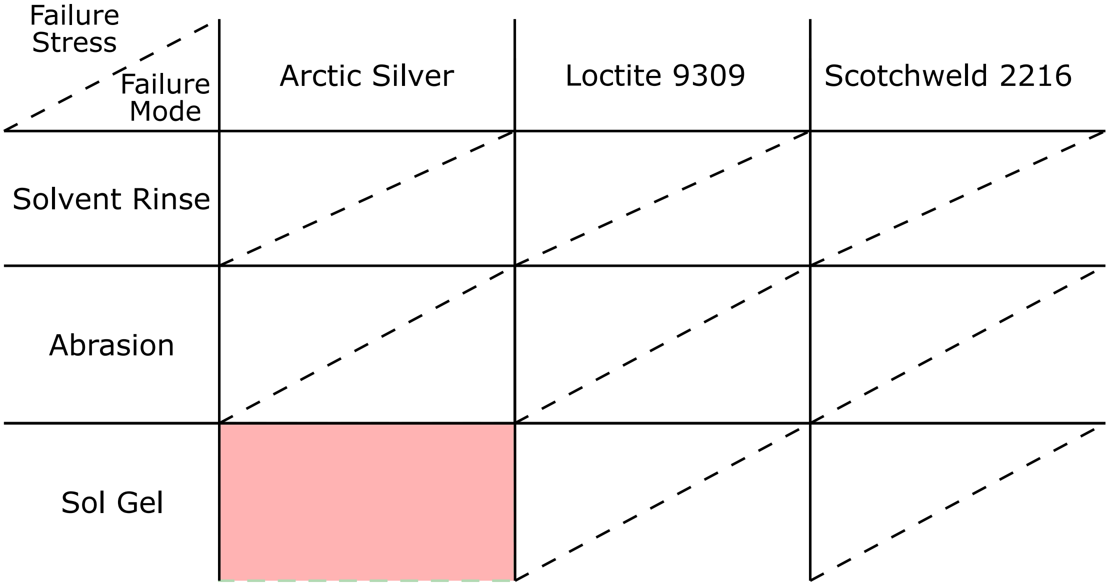

Failure Stress / Failure Mode	Arctic Silver	Loctite 9309	Scotchweld 2216
Solvent Rinse			
Abrasion			
Sol Gel	🟥		

Figure 3.7: Lap shear bonding test matrix of the SMA-composite adhesive.

the bond strength in shear. In total, eight specimens were tested; the Arctic Silver sol gel sample was unable to be fabricated as the epoxy was discontinued by the manufacturer.

3.5.2 Lap Shear Test Results

The maximum shear stress recorded in each test is depicted in figure 3.8, arranged to visualize the effect of each surface treatment. It can be seen that both surface treatments beyond solely rinsing the SMA specimens with solvents will increase the strength of the bond, and that performing a sol gel application in addition to a solvent rinse and abrasion will further increase the bond strength. However, the Loctite and Scotchweld samples showed different amounts of improvement from adding a sol gel application, so no conclusions can be drawn in terms of the relative benefit. Additionally, the two specimens with sol gel applied failed in a cohesive manner, while all other specimens failed adhesively. This indicates that the interfacial quality of the bonds without sol gel was the main cause of failure. It is important to note that even though surface treatments drastically improved the bond strength for both Loctite and Scotchweld samples, neither epoxy came close to the reported maximum shear strength (detailed in table 3.1). This could be due to the fact that the manufacturers perform lap shear tests with aluminum samples and optimized surface treatments

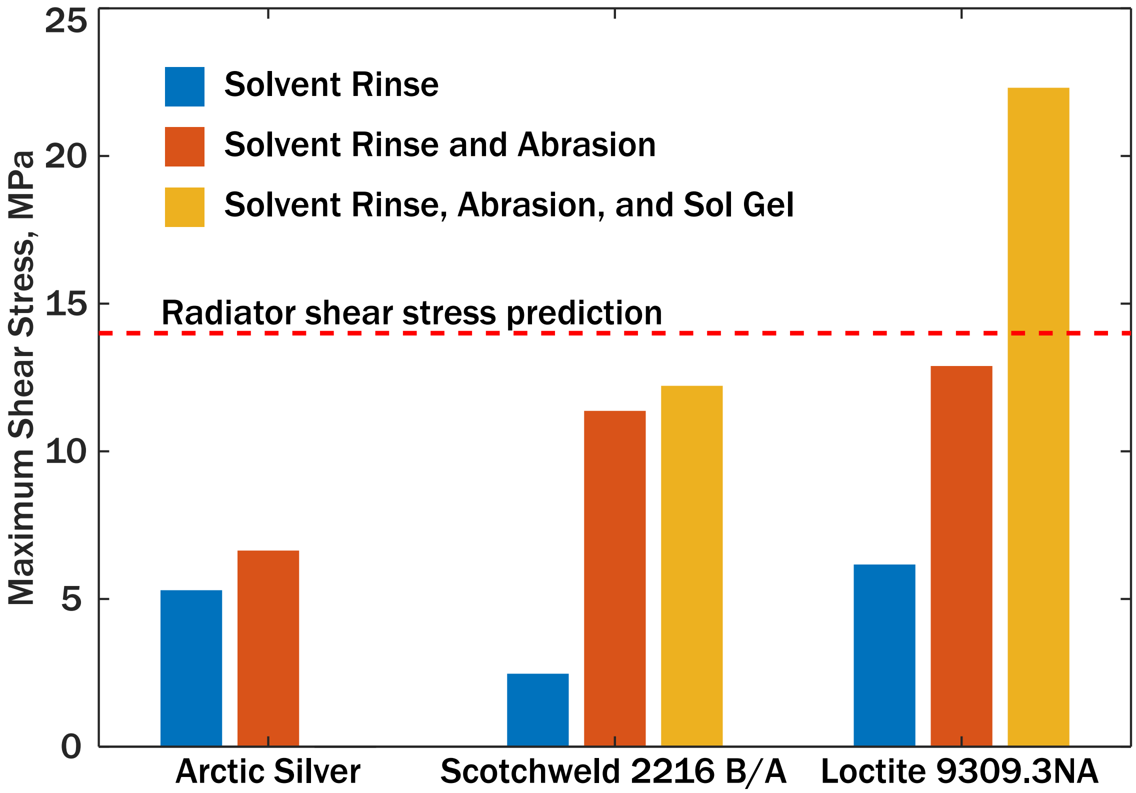

Figure 3.8: Graphical representation of the maximum shear stress obtained for all three candidate epoxies with respect to different surface treatments.

(e.g., grit blasting in a controlled environment), and illustrates the importance of surface treatments for bond strength in shear.

3.6 Actuation Bond Tests

Quantifying the performance of SMA-composite bonds solely using single lap shear tests is not an accurate prediction in terms of the morphing radiator. Therefore, the bonds were also subjected to SMA actuation loads to mimic the strains required for morping radiator actuation. However, there are no standardized test methods to quantify the strength of an adhesively bonded SMA under actuation, so a custom experiment was formulated.

3.6.1 Experimental Setup

The purpose of the actuation bond tests was to quantify the amount of strain that the adhesive bond was capable of withstanding before failure. The experimental setup consisted of an SMA

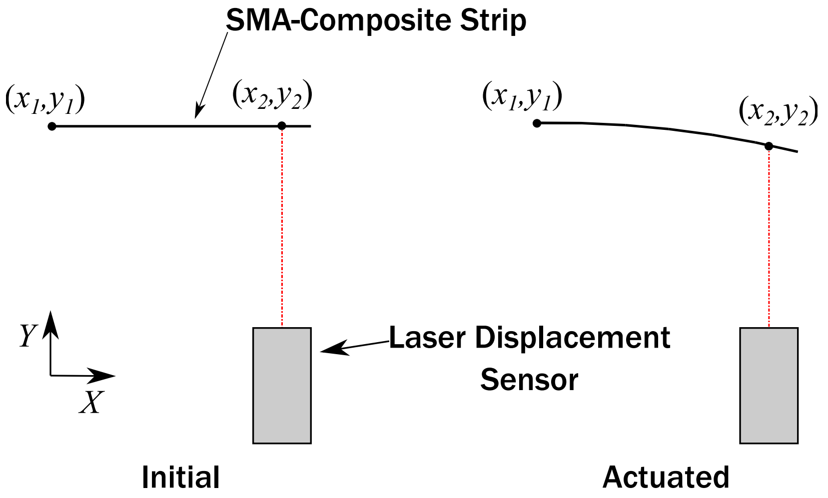

Figure 3.9: Schematic representation of the SMA-composite bonding setup.

strip bonded to a composite panel, which was clamped at one end to prevent displacement and rotation. A single type T thermocouple was placed in the center of the SMA strip to monitor temperature, and connected with a Fluke 287 multimeter for data collection. Displacement of the free end of the strip was measured using a Keyence laser displacement sensor and data collection was conducted via a National Instruments DAQ. Heat was applied to the specimen by one of two ways: a Dewalt heat gun at a small angle to minimize localized transformation, or an MTS environmental furnace to minimize the thermal gradients throughout the specimen.. Figure 3.9 depicts a schematic representation of the experimental setup.

By assuming that the displacement and rotation of the clamped end of the strip are zero and that the SMA-composite beam maintains constant curvature throughout actuation, the curvature as a function of tip displacement can be calculated. Considering the root and tip of the beam, labeled (x_1, y_1) and (x_2, y_2), an isosceles triangle having angles α, α, and θ can be formed. The angle α can be calculated by taking the inverse tangent of the line between the two points:

$$\alpha = \tan^{-1} \frac{|x_2 - x_1|}{|y_2 - y_1|}. \tag{3.6}$$

As the sum of the angles of all triangles is 180 degrees, and isosceles triangles have two equal

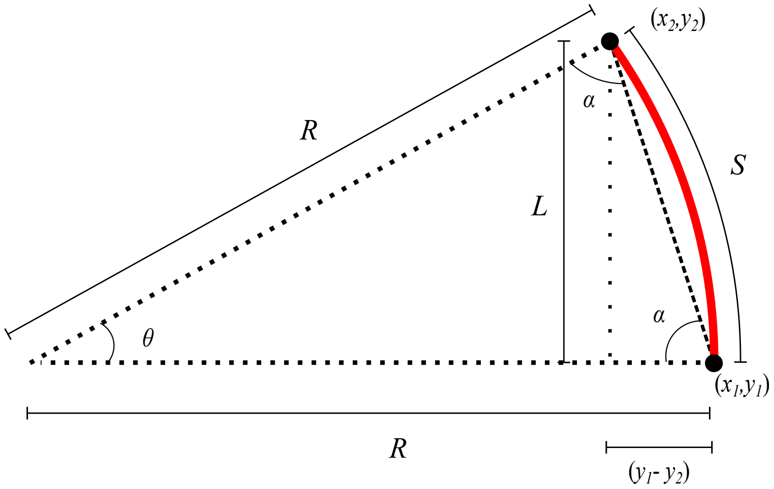

Figure 3.10: Schematic of actuated SMA-composite strip (shown in bold red), and relevant geometric parameters to calculate curvature.

angles, θ can be calculated:

$$\theta = 180 - 2\alpha. \tag{3.7}$$

Consequently, the radius of curvature of the beam can be calculated:

$$R = \frac{x}{\sin\theta}. \tag{3.8}$$

Finally, the curvature of the beam can be calculated by inverting the radius of curvature,

$$\kappa = \frac{1}{R}. \tag{3.9}$$

Using these simple geometric relations and a thermocouple, a curvature as a function of temperature can be computed. This allows for a quick characterization of the SMA-composite beam to quantify the performance of different adhesive bonding techniques.

3.6.2 Experimental Procedure

The following procedure is conducted when preparing samples for testing. This includes the steps necessary for applying the surface treatment to the SMA; for the specimens tested without steps 5-9 were omitted.

1. Sand the composite specimen with 240 grit sandpaper until water runs smoothly over its entirety. If the water beads at any point, the specimen has not been sanded thoroughly.
2. Clean the composite specimen with a strong solvent to remove any sanded material.
3. Abrasively clean the SMA specimen with a green scotch brite pad (600 grit). Be sure to conduct the cleaning on both sides of the specimen, as only sanding one side will induce curvature. It is also important to note that this step should be performed before detwinning the SMA, as the abrasive has the potential to locally transform the SMA.
4. Detwin the SMA to a 5% transformation strain.
5. Soak the SMA specimen in a solvent bath for approximately two minutes.
6. Mix the two parts (A and B) of the treatment together. Shake for fifteen seconds, then let sit for thirty minutes. After thirty minutes, shake for fifteen seconds once more.
7. Liberally apply the mixed treatment onto the SMA with a microfiber brush or spray for over two minutes, thoroughly soaking the entire area of interest.
8. Dry the treatment at ambient conditions in a controlled environment for at least two hours.
9. After the sol gel is sufficiently dry, apply the epoxy to both the SMA and composite, and ensure a consistent bond line by placing the sample in between two flat surfaces.
10. Once the epoxy is fully cured per the manufacturer specifications, the SMA-composite beam is clamped in an experimental fixture.
11. Data collection starts, and heat is applied to the beam until full actuation is achieved or the bond fails.

3.6.3 Actuation Test Matrix

The experimental test matrix was arranged to collect two types of data: the quantitative measure of maximum curvature attained under actuation (before bond failure or complete SMA transformation), and the qualitative measure of the bond failure mode, if present. The goal maximum curvature was 13.3 m^{-1}, derived from the change of curvature the morphing radiator would undergo from fully closed to semicircular states upon actuation. The failure mode is a metric to determine the quality of the bond line, and as mentioned previously a cohesive failure was desired. The three candidate epoxies were tested with two distinct surface treatments applied to different SMA specimens: pure abrasion (steps 1-6 of the experimental procedure) and abrasion with sol gel applied (steps 1-9 of the experimental procedure). These results were compared with a mechanically bonded sample (in which both ends of the SMA were affixed to the composite strip with set screws and terminal blocks), making for a total of seven data points in the study. Figure 3.11 depicts the test matrix graphically.

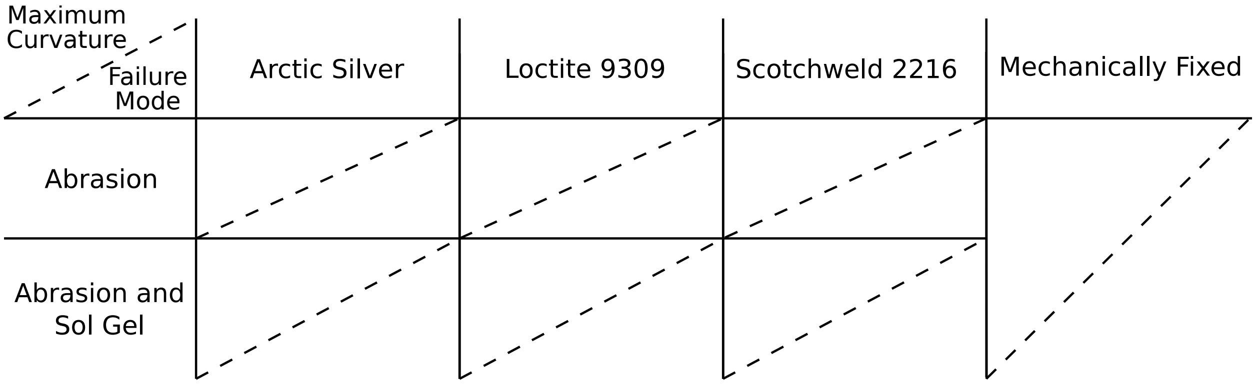

Maximum Curvature / Failure Mode	Arctic Silver	Loctite 9309	Scotchweld 2216	Mechanically Fixed
Abrasion				
Abrasion and Sol Gel				

Figure 3.11: Actuation test matrix of the bonded SMA-composite.

3.6.4 Actuation Test Results

Preliminary tests were conducted comparing the bond qualities of Arctic Silver to a mechanically fixed specimen. Figure 3.12 depicts the curvature and temperature as a function of time of the Arctic Silver test. At test point **a)** (approximately t=10s), heating of the sample begins. Due to the localized heating, the response is not constant and varies. Just before test point **b)**, the SMA starts to transform and the curvature of the beam increases. However, at a curvature of 4.8 m^{-1} the bond fails suddenly and the curvature drops substantially. At approximately t=180s (test point **c)**), the bond fails completely and the curvature returns to zero. Test point **c)** is omitted from figure 3.12, but the physical geometry of all three test points is depicted in figure 3.13. As shown in figure 3.13c, the SMA becomes completely detatched from the adhesive bond line. Upon further inspection, the bond failed adhesively between the epoxy and SMA, which suggested poor surface treatment on that interface. Additionally, due to the variability of temperatures along the beam and lack of precision associated with heating, all future tests were conducted within a furnace with a heating rate of 10°C/min to measure the steady-state curvature of the specimen.

Tables 3.2 and 3.3 show the maximum measured curvature and failure modes associated with tests conducted with mechanical abrasion and sol gel, respectively. The failure temperature of each bond is not recorded, as the critical parameters of this experiment are the bond strength and quality, but all samples failed very close to the austenite start temperature of the SMA material (specifics of which are provided in appendix **??**). Upon inspection of the mechanically abraded samples, no particular epoxy substantially outperforms another, and actually Arctic Silver performs slightly better than Loctite and Scotchweld. However, all three samples obtain less than 20% of the curvature obtained by the mechanically fixed analog. Additionally, all epoxied samples fail in a purely adhesive mode between the SMA and epoxy, suggesting the SMA exhibited poor surface treatment with mechanical abrasion alone.

Comparing the maximum curvature obtained for each surface treatment method, each epoxy sample shows a marked improvement when sol gel is applied, with Loctite performing the best out of the three. Additionally, the Loctite sample failed in a 50% adhesive mode (in which 25% of the epoxy remained on the SMA sample), which indicates improved surface treatment on portions of the SMA. However, even though the Loctite performed almost 50% with sol gel and mechanical abrasion, it still only achieved 25% of the curvature that the mechanically fixed sample achieved,

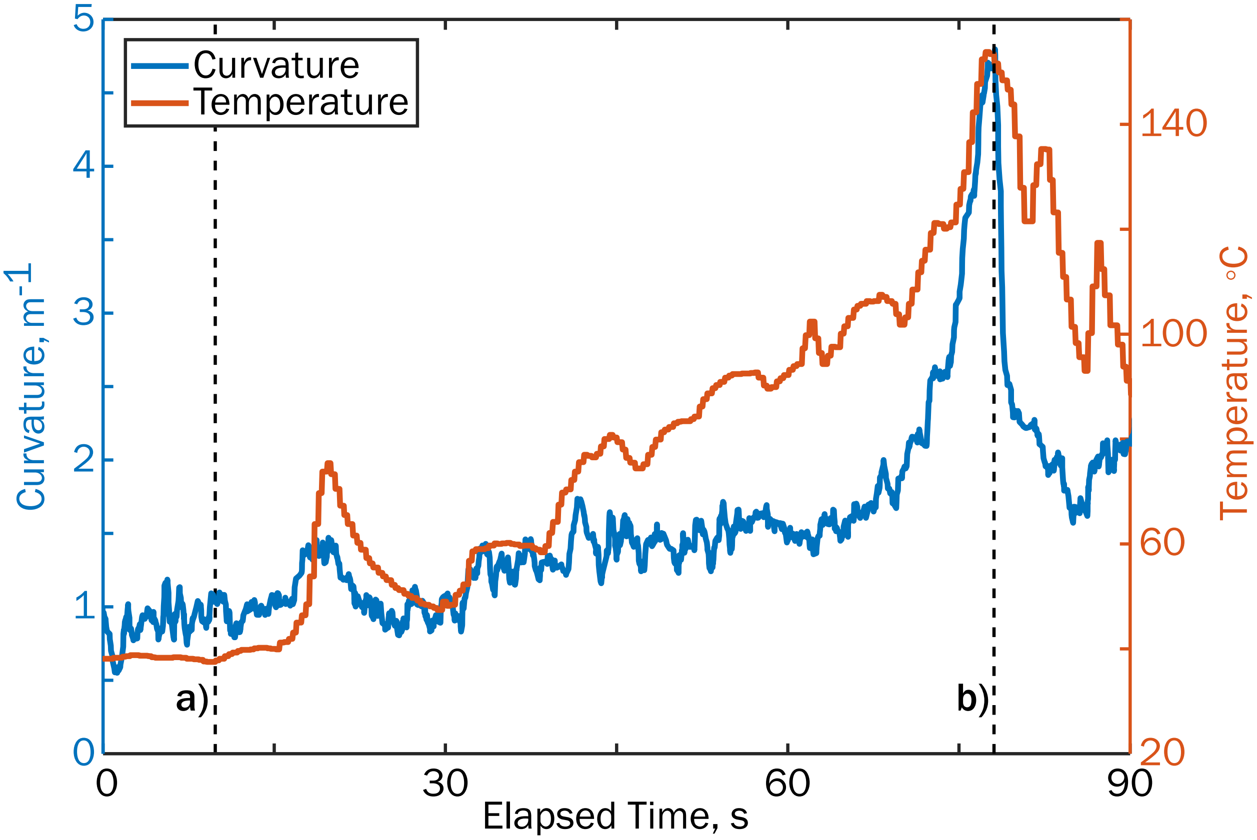

Figure 3.12: Temperature and curvature as a function of time for the Arctic Silver preliminary adhesive bond test.

Table 3.2: Maximum measured curvature and failure mode for the adhesively bonded SMA composite beams using only mechanical abrasion as a surface treatment, as compared to a mechanically fixed strip.

	Arctic Silver	**Loctite 9309.3NA**	**Scotchweld 2216 B/A**	**Mechanically Fixed**
Max Curvature, m^{-1}	1.62	1.59	1.41	9.33
Failure Mode	Adhesive	Adhesive	Adhesive	-

indicating that adhesively bonding the SMA onto the composite is severely outmatched in this application. This result is also depicted graphically in figure 3.14, and it is evident that the amount of curvature obtained from the adhesively bonded tests is not sufficient to solely bond the SMA

(a) Test point **a)** (b) Test point **b)** (c) Test point **c)**

Figure 3.13: Physical geometry of the Arctic Silver bonded specimen at three test points.

Table 3.3: Maximum measured curvature and failure mode for the adhesively bonded SMA composite beams using mechanical abrasion and sol gel as a surface treatment, as compared to a mechanically fixed strip.

	Arctic Silver	**Loctite 9309.3NA**	**Scotchweld 2216 B/A**	**Mechanically Fixed**
Max Curvature, m^{-1}	1.92	2.34	2.11	9.33
Failure Mode	Adhesive	50% Adhesive	Adhesive	-

onto the composite for future testing.

The adhesive bonds failed under actuation loads due to a combination of factors. First, even though both the Loctite 9309 and Scotchweld 2216 reported higher maximum lap shear strength that what was necessary, the loads experienced during actuation are not simple shear, but a combination between shear and peel. Additionally, the start of austenitic transformation of the SMA actuator was at a relatively high temperature, which could have contributed to debonding. However, installation the SMA at lower temperatures was not possible due to epoxy viscocity. Phenomenon including the debonding of foils under the shape memory effect has not been widely studied [56, 78].

3.7 Bonding Summary and Conclusion

A multi-faceted surface treatment and bonding study was conducted to investigate implementing a bonded SMA actuator on the morphing radiator. Optical microscopy was used to qualitatively

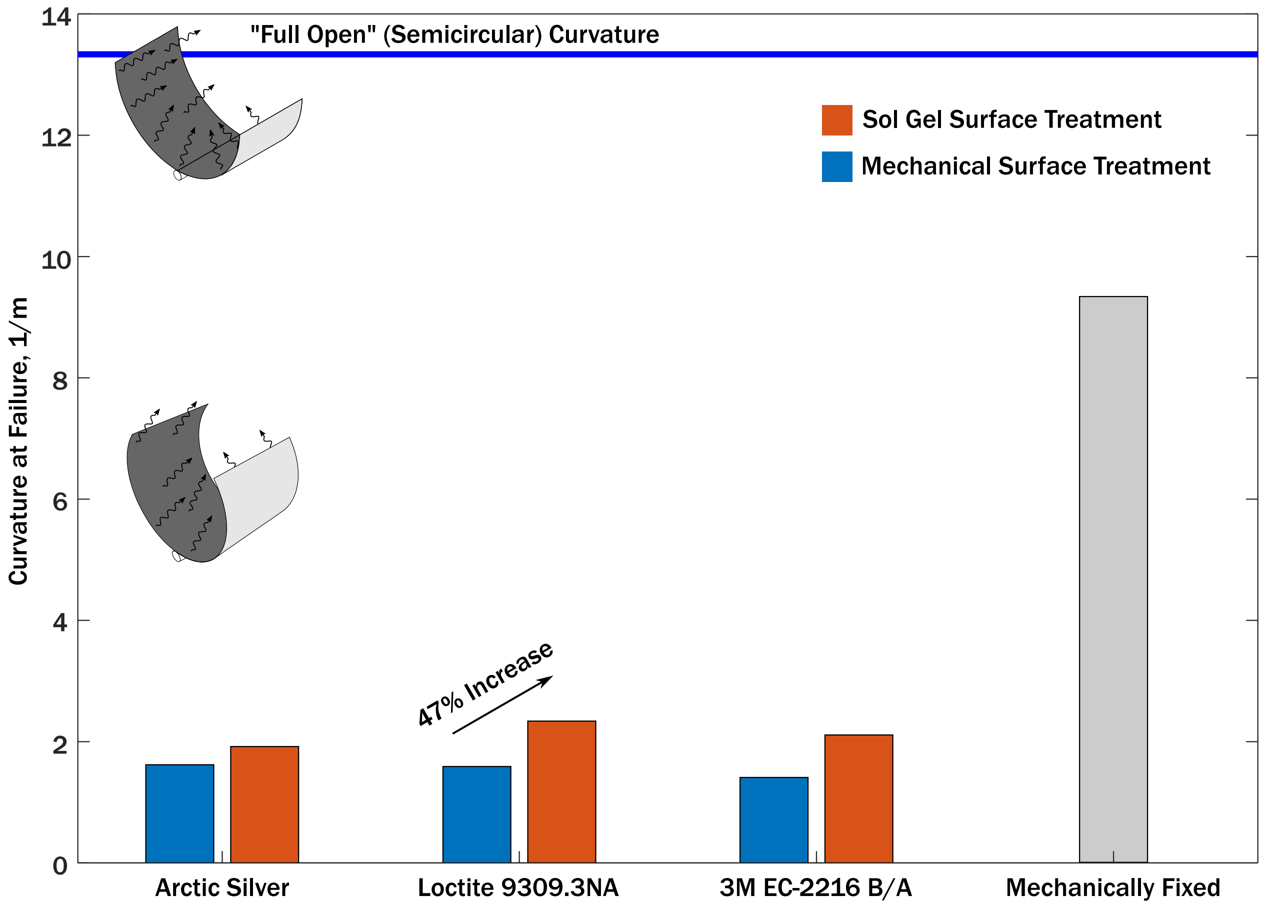

Figure 3.14: Graphical representation of the maximum curvature obtained for all three candidate epoxies, as compared to the mechanically fixed analog and goal curvature of the morphing radiator.

analyze the effect of different surface treatments on virgin SMA sheet. Abrasive cleaning was compared to nitric acid etching, and it was found that nitric acid was insufficient. Therefore, renewed focus was placed on sol gel treatments to improve the adhesive qualities of the epoxy-SMA interface. Single lap shear bond tests were conducted, and it was found that the specimens with sol gel exhibited the most improvement over the baseline specimens and failed cohesively, which indicates the sol gel may eliminate the problems caused by the titanium rich oxide layer present on NiTi alloys. Actuation test results followed the same trends, with the specimens with sol gel performing the best. However, the best performing adhesively bonded specimen only achieved 25% of the maximum curvature achieved by a mechanically fixed analog. Therefore, the tested prototypes will not include solely adhesive bonding to affix the SMA onto the composite panel.

4. MANUFACTURE AND DEMONSTRATION OF A HIGH TURNDOWN RATIO MORPHING RADIATOR

This study culminated in testing multiple morphing radiator prototypes in a relevant thermal environment to demonstrate the high turndown ratio capability of the concept. Refined manufacturing methods were implemented using prior knowledge and revised techniques specific to the current morphing radiator configuration. Multiple component improvements were integrated to resemble a space-qualified radiator. Prototypes were installed in a thermal vacuum chamber at NASA Johnson Space Center and the temperature of a thermal working fluid was cycled to induce SMA actuation. Tests were conducted with a single panel and two panels installed in series, signifying a step towards subsystem scale demonstration. This section outlines the various improvements made to the manufacturing process, details the experimental process, and describes conclusions gained from thermal vacuum chamber testing.

4.1 Component Improvements

Three areas of improvement were identified after the previous relevant environment testing in a thermal vacuum chamber: 1) enhance heat transfer from the flow tube into the panel, 2) upgrade high-performance coatings to exhibit a greater difference in internal and external emissivities, and 3) implement radiation end shields to minimize heat rejection in the cold configuration. Past prototypes had transferred heat from the fluid loop to the radiator fin via a bond of thermally-conductive epoxy. However, as most thermally-conductive epoxies only exhibit conductivities on the order of 1 W/mK, an aluminum (conductivity of 167 W/mK) tube mount was designed to maximize the heat transfer from the fluid loop to the radiator. The optimized tube mount was designed to match the curvature of the radiator in the closed configuration and was epoxied using a thin layer of conductive epoxy. A schematic representation of the previous and optimized fluid flow block designs is shown in Figure 4.1. Figure 4.2a shows CAD renderings of the fluid flow block. The upper surface of the tube mount is machined to a radius of 3 inches, which is identical to the composite

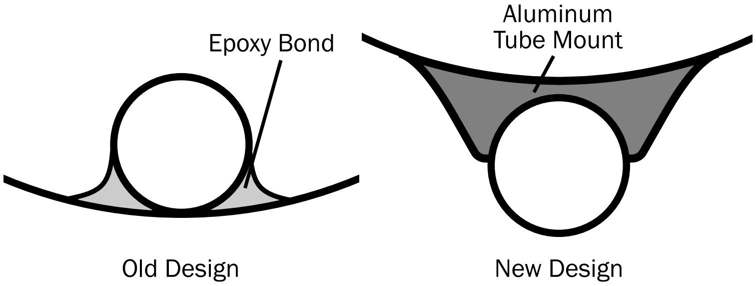

Figure 4.1: Previous and current fluid flow interface schematics. Reprinted with permission from [50].

laminate in the closed configuration.

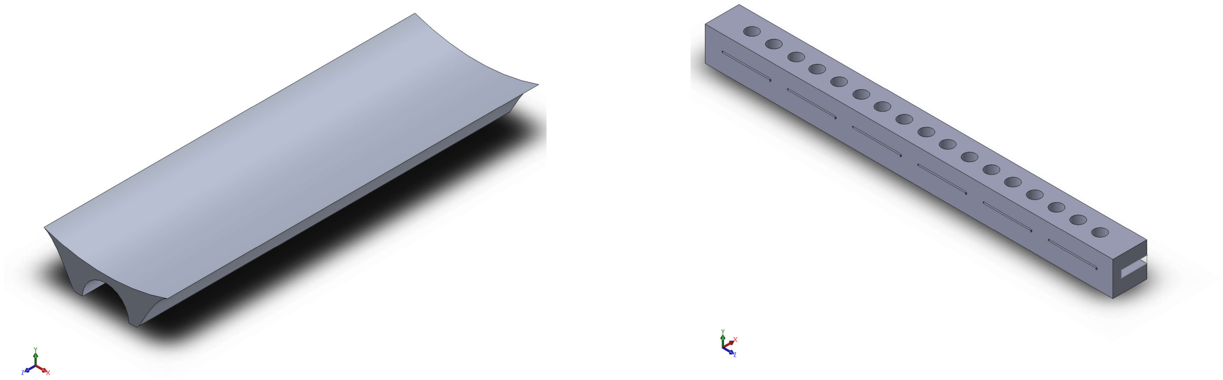

(a) Isometric view of the fluid flow block.

(b) Isometric view of the modified terminal block.

Figure 4.2: CAD renderings of the custom-machined components for panel assembly.

The prototype radiator was also coated with Acktar Black Velvet high-emissivity film ($\varepsilon = 0.937$) on the concave side and multi-layer insulation (MLI) ($\varepsilon = 0.037$), procured by Paragon Space Corporation, was applied on the outside[1]. This difference in inside and outside emissivities represents a vast improvement over past prototypes ($\Delta\varepsilon = 0.9$ compared to $\Delta\varepsilon = 0.4$ from prior work) [17]. Additionally, previous mechanical fixturing methods were updated to accomodate

---

[1] Trade names and trademarks are used in this report for identification only. Their usage does not constitute an official endorsement, either expressed or implied, by the National Aeronautics and Space Administration.

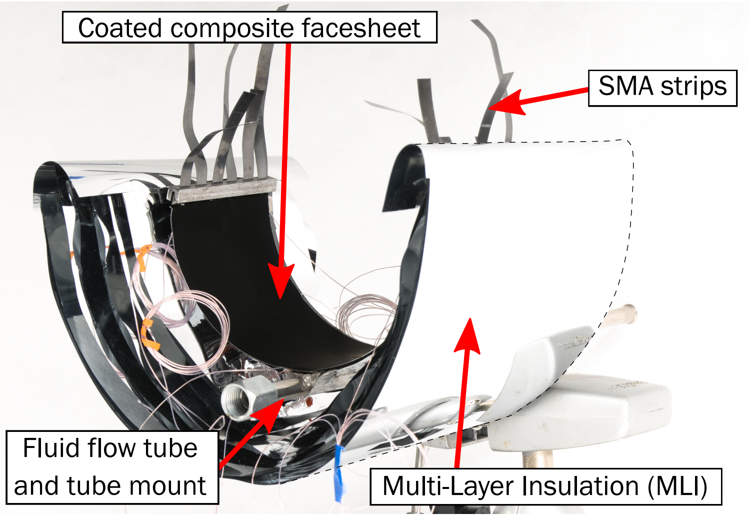

Figure 4.3: Morphing radiator prototype with Multi-Layer Insulation (MLI) installed (Note that MLI is highly reflective, leading at times to unclear images). Reprinted with permission from [50].

SMA strips, depicted in figure 4.2b. The rectangular slots on the terminal block were required to accept the strips for pre-stressing during assembly. Finally, radiation end shields were designed to match the radiator inner diameter, machined from Aluminum 6061, and similarly coated with Black Velvet on the interior and MLI on the exterior. Figure 4.3 depicts an assembled prototype with optimized flow tube and high performance coatings, but without end shields for clarity.

Additionally, a training fixture was designed and machined to expedite the SMA training process. For the 0.2032 mm thick NiTi, even though the material exhibited a large amount of stability and only required three cycles for sufficient training, the lack of a fixture to train multiple lengths of strip at once increased the time spent training by almost an order of magnitude. To remedy this, a fixture was machined to accept a single long strip of SMA, which is woven around pulleys and secured to the fixture at both ends (Figure 4.4). This fixture was placed in a thermal chamber and the entire length of the strip was trained at the same time.

4.2 Manufacturing Methods

To produce a morphing radiator prototype that resembled space qualified hardware, all components of the radiator (composite facesheet, end shields, tube mount, and SMA actuators) required

(a) Isometric view of the SMA strip training fixture.

(b) Front view of the SMA strip training fixture with strip installed.

Figure 4.4: SMA strip training fixture.

strict manufacturing methods. The composite facesheet was constructed the same way as prior work; a laminate assembly of pre-impregnated carbon fiber sheets were vacuum bagged and cured in a circular shape (the radiator cold state) [85]. End shields and tube mounts were machined out of 6061 aluminum sheet, and tabs protruding from the end shields were angled to facilitate bonding with the composite facesheet.

Previous test articles including strips involved detwinning the strips by submerging them in liquid nitrogen while previous test articles involving wires were installed by clamping less than 50lbs of weight to pre-stress the material. Submerging the strips in liquid nitrogen was not available for the tests in this work, so a method was developed to subject the SMA strip to the correct prestress (200 MPa, or approximately 250 lbs). This involved installing a custom prestressing jig onto an MTS load frame to ensure the SMA actuators were loaded sufficiently during installation, depicted in figure 4.5. To install the actuators on the prototype, the following procedure was used:

1. Open the facesheet prototype to a semicircular shape with a roll of spring steel to prevent against material failure.

2. Install the prototype onto the prestressing jig and fasten the terminal blocks to each circumferential end with set screws.

3. Align a slot in the terminal block with the frame load path.

4. Thread one SMA strip actuator through the prestressing jig and secure each end to the upper load frame grip.

5. Raise the upper grip until the prestress load was reached and constant.

6. Secure the strip with set screws and release the load.

7. Repeat until all six strips were secured.

8. Remove the morphing radiator prototype from the prestressing jig.

This procedure allowed for safe and consistent prestressing loads to be applied to each SMA actuator and represents an advance in manufacturing repeatability compared to previous prototypes (wherein the SMA wires were prestressed by use of a pair of visegrips with weights attached). However, the jig started to deform under the prestressing load and contributed to the radiator curvature varying in the radial direction. In future work, this deformation could be mitigated by manufacturing a more robust jig that can withstand higher applied moments (84 N-m or 750 lbf-ins).

After the SMA actuators were installed on the facesheet, coatings were applied to both concave and convex sides. Acktar black coating was rolled on the concave side to ensure a smooth surface and the MLI was attached to the convex side using double sided Kapton tape. Last, end shields were similarly coated and epoxied to the composite facesheet using Arctic Silver Thermal Epoxy.

4.3 Thermal Vacuum Chamber Testing

To simulate a radiative space environment in a laboratory, thermal vacuum chamber (TVC) testing was performed on the morphing radiator prototypes. Multiple different tests were performed on the prototypes with NiTi and cobalt SMA actuators installed to better characterize the

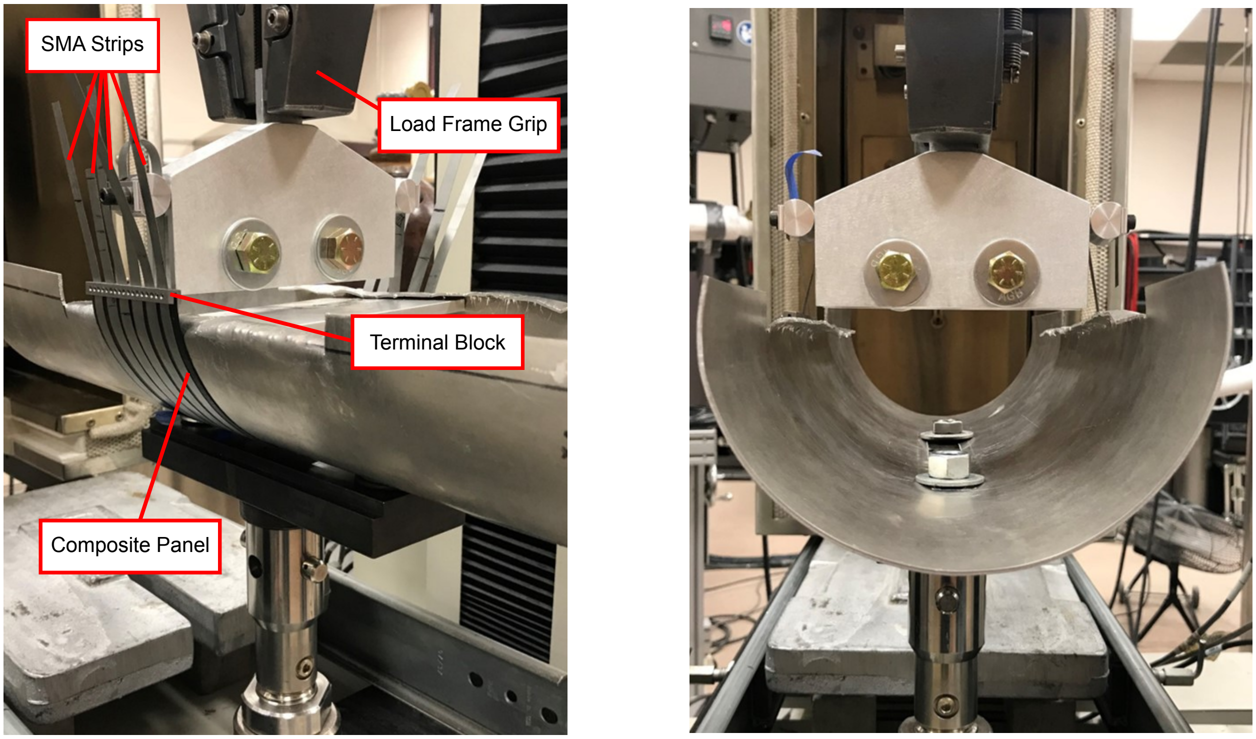

(a) Isometric view.

(b) Front view.

Figure 4.5: Prestressing jig installed on the load frame.

morphing radiator system and demonstrate maturation of the technology to a higher TRL. Both one- and two-panel tests were conducted, with the two panels installed in series configuration to illustrate the scalability of the concept in a relevant thermal environment. In all, five days of testing was completed; in this work two specific tests will be discussed: a two-panel test with the NiTi actuators and a one-panel test with the cobalt actuators.

4.3.1 Test Setup

Thermal vacuum chamber testing was conducted in Chamber G at NASA Johnson Space Center. The chamber cylindrical test section measures 0.4318 m (17 in) in diameter and 0.5842 m (23 in) in depth, allowing for installation of two morphing radiator panels (maximum dimensions 0.1778 m by 0.2286 m). The test section is surrounded by a temperature-controlled shroud that allows for varying effective sink temperatures and provides a surface to which the radiator can reject heat. A fluid loop is integrated to the TVC which is powered by a SP Scientific RC211 pump

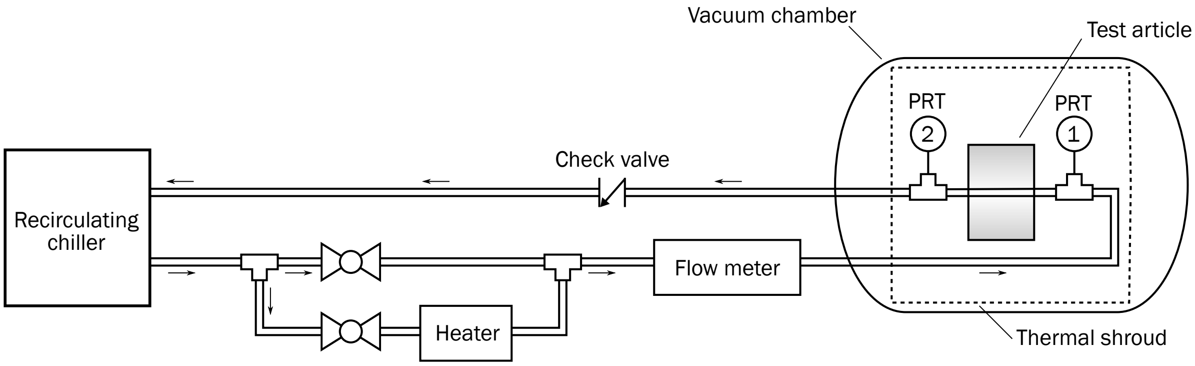

Figure 4.6: Schematic description of the experimental setup.

and contains a fluid heater and chiller to control the working fluid temperature. Two platinum resistance thermometers (PRTs) were positioned in the fluid loop at the radiator inlet and outlet to measure the temperature change across the prototype. Dynalene HC-50, a nontoxic thermal fluid with a freezing point of -50°C, was used in this study. The test article was positioned in the center of the test section with the concave side of the radiator facing down. Figure 4.6 describes the experimental setup and 4.7 depicts two radiators installed in series in Chamber G. Type T thermocouples were epoxied to installed prototypes to measure the temperature in different locations of the radiator.

The chamber setup allowed for multiple variables to be specified throughout the test. First, the working fluid temperature was specified and cycled to induce SMA transformation via heating and cooling of the composite panel. Second, the flow rate of the working fluid was varied to attempt to measure the temperature drop as a result of the radiator rejecting heat, as a lower flow rate could potentially allow for a higher temperature drop. Third, the shroud temperature was varied to attempt to simulate adverse thermal conditions in which the radiator rejects high amounts of heat to a warmer environment and low amounts of heat to a colder environment. Prior studies had only focused on varying the working fluid temperature to characterize the actuation behavior of the morphing radiator; this work represents a step towards understanding the system behavior in the context of adverse thermal environments.

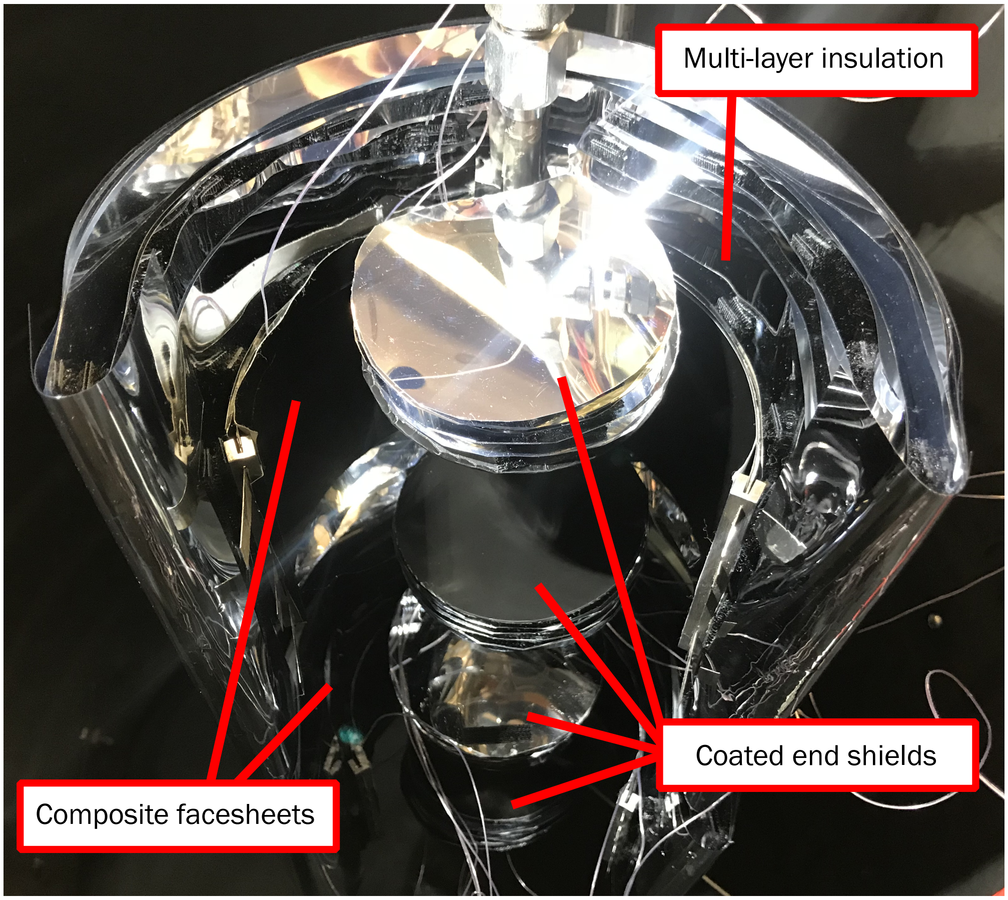

Figure 4.7: Two morphing radiator prototypes installed in Chamber G at NASA JSC. Reprinted with permission from [50].

4.3.2 Test Results

In this work, two main thermal vacuum chamber tests will be discussed: a two-panel test with the NiTi strips installed, and a single-panel test with the cobalt strips. Each test provided crucial information pertaining to the morphing radiator system, results of which are detailed herein.

4.3.2.1 Two Panel NiTi Test

Two morphing radiator prototypes were installed inside the test section in series to advance the technology towards a subsystem demonstration. The test setup consisted of a temperature-controlled fluid loop that pumped Dynalene HC-50 through the radiator prototypes, which radiated heat to a temperature-controlled shroud maintained at -178°C. Temperature was measured with

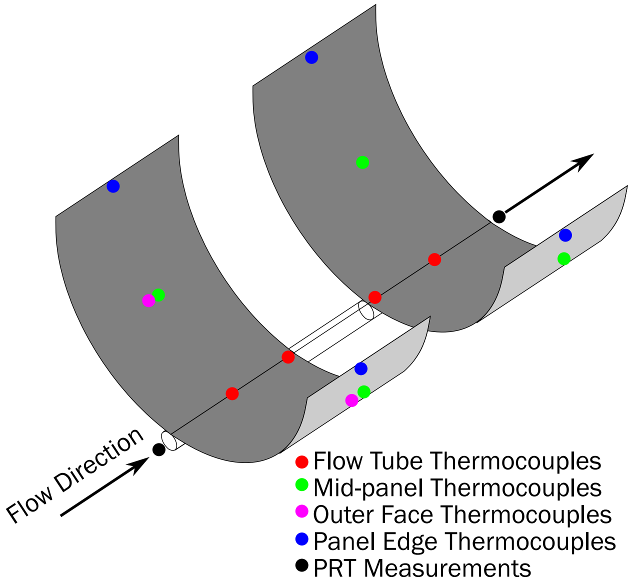

Figure 4.8: Thermocouple and PRT placement for vacuum chamber testing. Reprinted with permission from [50].

14 thermocouples on the panels, and fluid temperature was measured via two platinum resistance thermometers (PRTs) that were submerged in the flow. A schematic of the thermocouple and PRT placement relative to the prototypes is shown in Fig 4.8. Note that the MLI and end shields are omitted for clarity. A digital camera was installed on the outside of the chamber window to record the deformation of the radiator at a frequency of 0.033 Hz, and the thermocouples were sampled at a rate of 1.0 Hz. Figure 4.7 shows both radiator prototypes installed in the thermal vacuum chamber.

The test started with the fluid temperature at a constant temperature of 50°C, and the flow rate was held at a constant of approximately 50 kg/hr to establish a steady-state heat rejection rate for the hot case. After 20 minutes, the flow rate was increased and the fluid temperature was reduced to -20°C after cooling for approximately 90 minutes. Upon reaching the cold limit, the flow rate was once again reduced for 20 minutes to measure a steady-state heat rejection rate for the cold case. The flow temperature and flow rate were subsequently increased, and once the panel reached room temperature, the test concluded. Due to time constraints and equipment malfunction, the fluid temperature was unable to reach 50°C, but full recovery during heating was observed in both

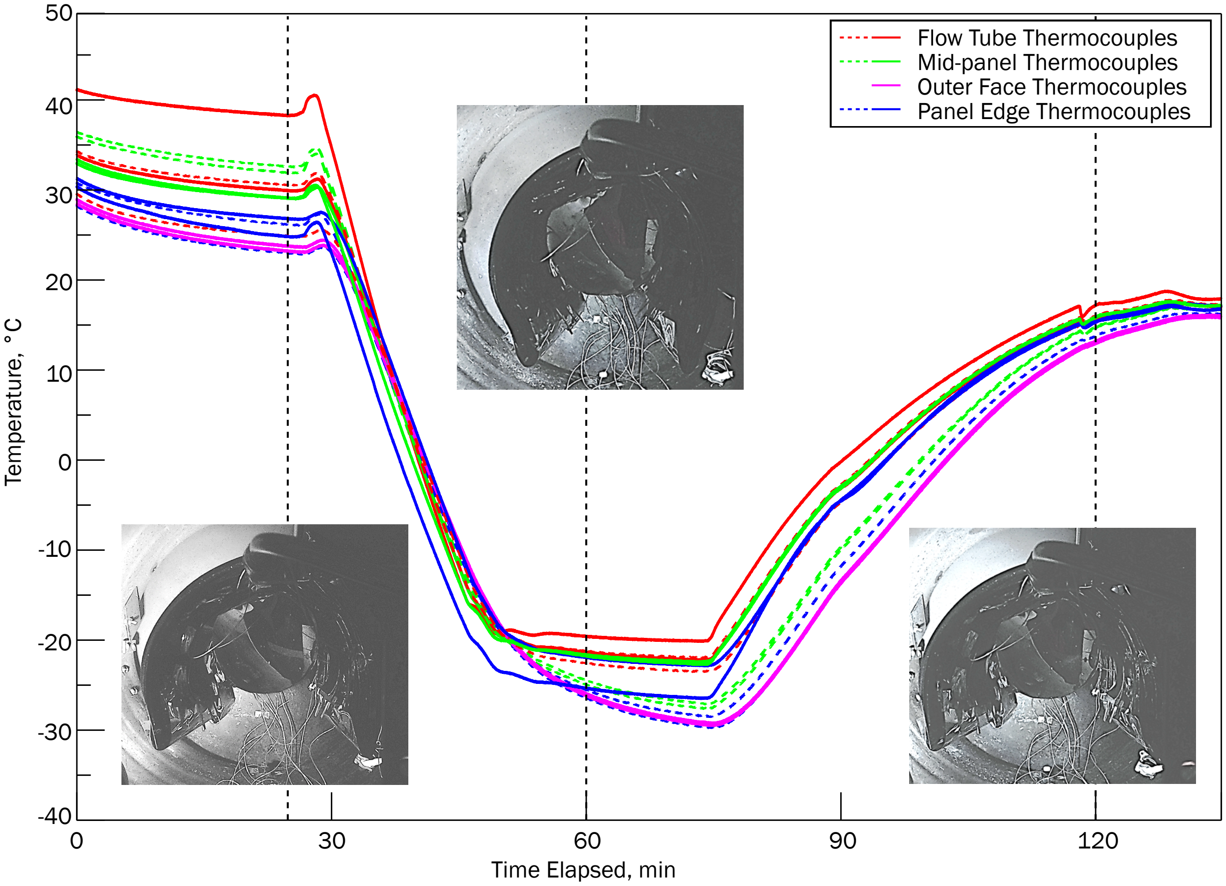

Figure 4.9: Temperature vs. time history for the two-panel thermal vacuum chamber test (see figure 4.8 for thermocouple placement schematic). Reprinted with permission from [50].

prototypes.

Figure 4.9 depicts the temperature-time history of the test for both panels, where the solid and dotted lines denote the temperatures closer to and farther from the fluid inlet, respectively. Although the prototypes did not exhibit the desired morphing to full closure during cooling due to the mismatch in chamber operating temperatures and SMA transformation temperatures (figure 2.9a, there are still insights to be gained from the experimental data. Examing figure 4.9 the cold state (t = 60 min), there is some latency observed in both the thermocouples on the outside of the first panel (solid magenta lines) and the second panel (dotted blue and green lines), from t = 50 min-80 min. This indicates a temperature gradient through the thickness of the composite prototype and over the length of panels. While the gradient over the length of the panels is to be expected due

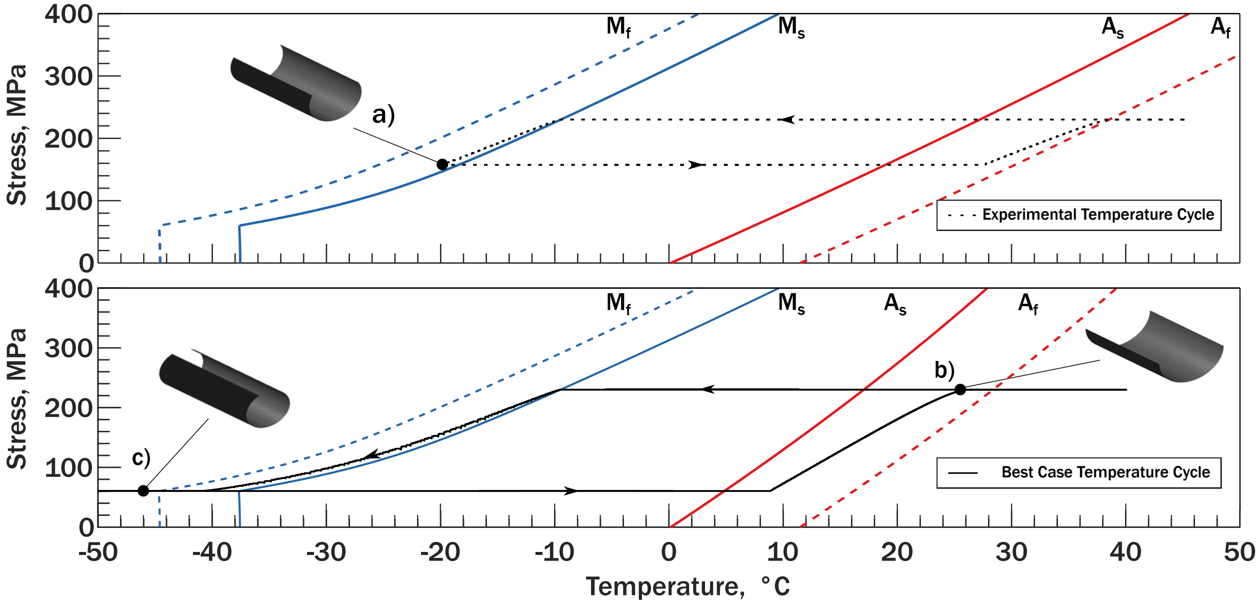

Figure 4.10: Stress-temperature cycle for the two panel NiTi strip test, as predicted by the composite-SMA model.

to heat loss from radiation, prior work has assumed the temperature to be constant through the thickness of the composite; thus, models must be corrected to include this by considering the full heat transfer calculations.

Due to the challenging lighting environment in the chamber, quantitative curvature measurements of the composite panel are not possible with the current experimental setup. However, qualitative comparisons can be made with respect to the experimental test data and model predictions. Figure 4.10 depicts the SMA phase diagram and the temperature-stress cycle of the morphing radiator as predicted by the SMA-composite model for the same temperature cycle as tested (assuming thermal homogeneity). Incomplete transformation to martensite is observed in both the experiment and model predictions at the lower limit of the temperature cycle (Figure 4.10, state a). Additionally, full recovery is shown at the upper limit of the temperature cycle (Figure 4.10, state b). The performance of the radiator can also be assessed if the fluid temperature had been cycled from 50°C to -50°C (the best case, shown as the dashed line of Figure 4.10). Although the radiator actuates significantly more towards full closure, the model still predicts incomplete actuation for

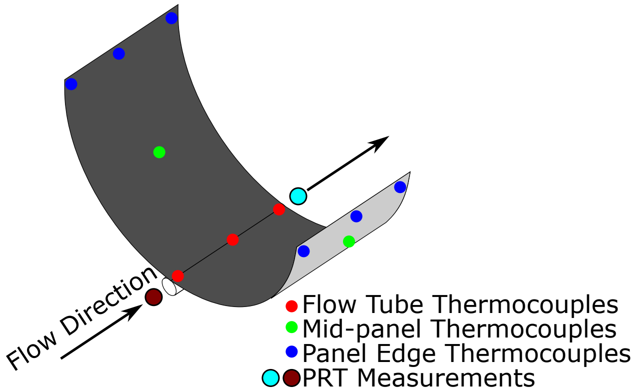

Figure 4.11: Schematic description of thermocouple and PRT placement for single panel cobalt test.

a temperature of -50°C due to the lack of two-way transformation strain generation in the SMA material (Figure 4.10, state c).

4.3.2.2 Single Panel Cobalt Test

Thermal vacuum chamber testing was conducted on a single test article with cobalt SMA strips installed to demonstrate the utility of tuning SMA transformation temperatures to achieve large turndown ratios. In this test, the same fluid loop temperature cycle was used as the previous test, but both the fluid flow rate and shroud temperatures were varied. The fluid flow rate was varied to attempt to measure the radiator turndown ratio experimentally, and the shroud temperature was varied to simulate an adverse thermal environment similar to that experienced on a Mars mission. Temperature was measured with eleven type T thermocouples epoxied to the radiator prototype and six thermocouple affixed to the shroud. Similar to the NiTi strip tests, fluid loop temperature was measured with two PRTs at the inlet and outlet of the test article. Figure 4.11 depicts the thermocouple and PRT placement for the single panel cobalt test. Temperature measurements were recorded at a frequency of 1 Hz. A digital camera was installed in the chamber viewing window and images were recorded at a frequency of 0.033 Hz, consistent with the NiTi strip test. To ameliorate the poor lighting environment observed in the NiTi tests, marking dots were placed in critical locations on the panel to assist with curvature measurements.

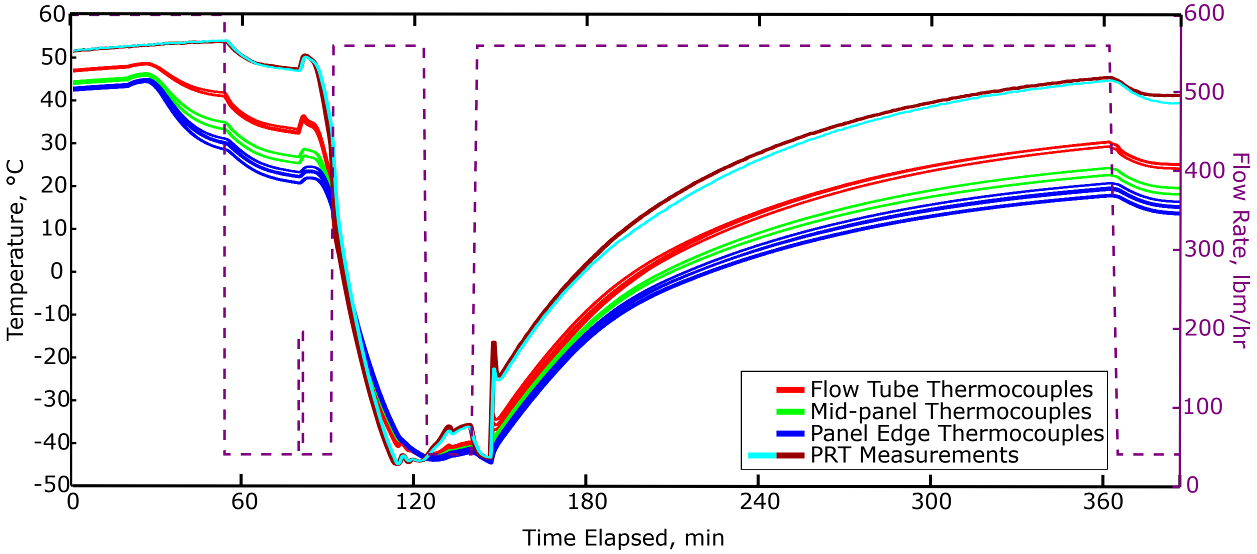

Figure 4.12: Time histories of the panel thermocouples, PRTs, and fluid flow rate for the single panel cobalt strip test.

Figure 4.12 depicts the time histories of the panel thermocouples, PRTs, and the fluid flow rate. The test starts with a the fluid temperature upwards of 50°C with a high flow rate. At approximately t=30 minutes, the shroud is cooled to -176°C and the panel starts to cool. Once the panel temperatures appear to have reached steady-state, the flow rate is decreased at t=55 min to measure the temperature drop over the panel via the PRT measurements. Cooling starts at t=75 min, signified by the slight increase in flow and panel temperatures. At t=80 min, the flow rate is increased to cool the panel and fluid temperature faster. After the fluid temperature reaches the low setpoint of -45°C, the flow rate is once more decreased to obtain a steady-state measurement of the radiator in the cold state (t=120 min). The slight increase in fluid temperature is due to the heater being turned on to ensure the fluid did not freeze. After dwelling at the cold state for ten minutes, the flow rate was increased and heating to the upper setpoint begain (signified by the spike in PRT temperature). The fluid and panel warms much slower than it did while cooling, but at t=360 min the flow rate was reduced for a last steady-state measurement, after which the test concluded.

Due to modifications in the chamber lighting setup and the addition of tracking points on panel key locations, in situ radius measurements were possible. Figure 4.13 depicts the time history

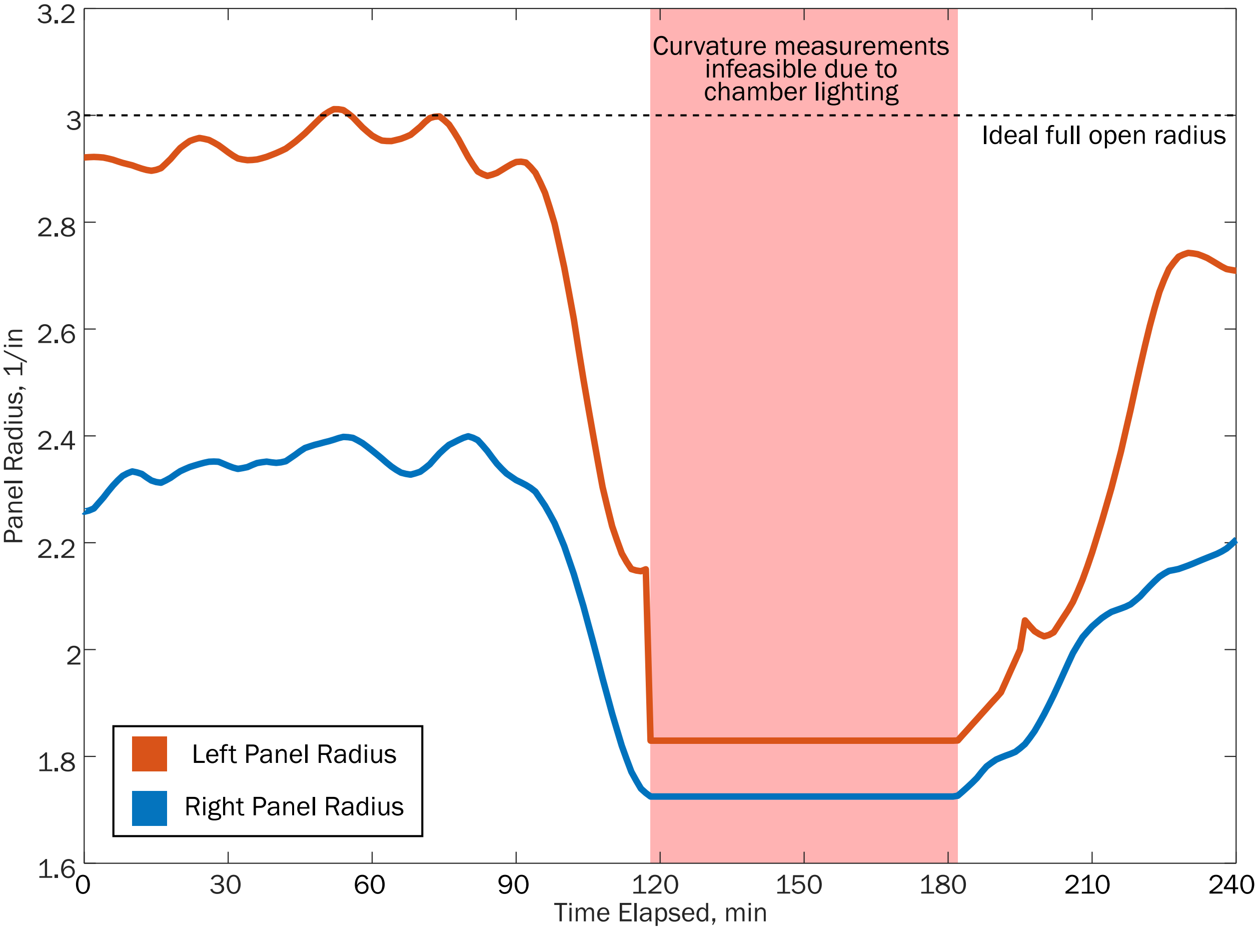

Figure 4.13: Time histories of the left and right panel radii during the single panel cobalt thermal vacuum chamber test.

of the left and right panel radii during the test. At the start of the test, a large disparity between radii is observed (almost 0.75 in). However, as cooling begins and the SMA actuators transform to martensite (t=100 min), both sides of the radiator start to close and the disparity decreases. During the cold state of the test (t=115-185 min), curvature measurements became infeasible, as the majority of the panel was hidden from view by the radiative end shield nearest the chamber viewing window. Upon heating, the panel actuates towards an open configuration and measurements resume.

The disparity in right and left radii may be due to manufacturing defects on the panel induced by the prestressing process; the deformation of the prestressing jig under high loads resulted in certain sections of the panel exhibiting more curvature than others. Additionally, the panel curvature was not constant close to the fluid flow block, as it was epoxied to the panel at a fixed radius of 3 in. This phenomenon may be responsible for incomplete radiator closure in the cold state.

With the curvature measurements obtained from the thermal vacuum chamber, conservative calculations can be made to determine the heat rejection rate of the radiator, and thus the turndown ratio of this particular prototype. The method developed in prior work was utilized and updated to account for the radiator coatings, geometry, temperatures, and end shields. Table 4.1 shows the parameters used to calculate steady-state heat rejection rates from the cobalt strip tests. The concave and convex surface emissivities were modeled as the tested materials, exhibiting emissivities of 0.937 and 0.037, respectively. Using the radiator parameters for the hot and cold states, the heat rejection rate for each state was calculated to be 6.22 W and 0.85 W, respectively. This results in a turndown ratio in a favorable thermal environment of 7.32:1, a significant increase from previous prototypes.

Additionally, the previous morphing radiator thermal vacuum chamber tests were conducted with a hot state root temperature of 65 °C, a 24°C increase over the current prototypes. This large discrepancy was due to the chamber fluid heater malfunctioning and time constraints prevented heating to that temperature. However, assuming the morphing radiator prototype attained this higher root temperature and didn't open any further (a conservative estimate), the heat rejection rate during the hot state becomes 7.49 W, resulting in a turndown ratio of 8.8:1. This turndown ratio is a more accurate comparison to previous prototypes, as the tested temperatures are consistent. The turndown ratio of 8.8:1 represents a 40% increase in performance over all previously tested morphing radiators and is a result of better actuation.

4.4 Comparison to Design Tool

To demonstrate the utility of the previously described morphing radiator design tool, comparisons were made between the tool predictions and the tested prototype performance. The right and left open angle measurements were compared to the predicted open angle measurements and the percent error was calculated for both the hot and cold state of the NiTiCo single panel tests, as

Table 4.1: Radiator parameters used in steady-state heat rejection rate calculations.

Parameter	**Hot State**	**Cold State**
Left Radius	3.061 in	1.829 in
Right Radius	2.512 in	1.706 in
Concave Emissivity	0.937	0.937
Convex Emissivity	0.037	0.037
Sink Temperature	-177.845°C	-177.7°C
Root Temperature	41.615°C	-40.78°C

Table 4.2: Comparisons between design tool predictions

Parameter	**Hot State**	**Cold State**
Left Curvature	12.9 m^{-1}	21.5 m^{-1}
Right Curvature	15.7 m^{-1}	23.0 m^{-1}
Predicted Curvature	13.1 m^{-1}	26.1 m^{-1}
Right Percent Error	3.5%	17.7%
Left Percent Error	17.5%	12.0%

shown in table 4.2. Design tool predictions were within 20% of tested prototypes, and the discrepancy between the two can be explained due to a multitude of reasons. First, the panel curvature measurements were averaged over each half-panel, while during experiments the panel curvature varied as a function of circumferential distance. Second, the design tool assumed small local deflections and calculated the curvature of one infinitesimal unit, while the real prototype underwent large deflections. Last, the SMA calibration was conducted for untrained material, but training the NiTiCo potentially altered the constitutive behavior. Regardless of these discrepancies, these predictions provide a good first-order approximation of radiator behavior and the design tool can be used in future applications.

4.5 Conclusion

In this section, the progress made towards manufacturing and testing a high TRL and high turndown ratio morphing radiator prototype was discussed. Multiple component improvements were enacted, including space quality coatings, optimized heat transfer methods, and radiative end shields. Manufacturing methods were revised to incorporate prestressing and installation of SMA strips. Two thermal vacuum chamber tests were discussed: a two-panel test with NiTi acutators, and a single-panel test with cobalt actuators. The two panel test demonstrated the subsystem functionality of the morphing radiator concept, but failed to produce quantitative curvature data due to SMA material incompatibilities and a poor lighting environment. The single panel test improved the lighting environment and used SMA actuators tuned for the experimental temperature cycles, and achieved a turndown ratio of 7.32:1. Additionally, when compared to previous test cycles, the turndown ratio increases to 8.8:1 as a result of the higher hot state root temperature.

While this turndown ratio is more than 40% higher than the turndown ratio of previous prototypes, the morphing radiator concept has been projected to provide a turndown ratio as high as 26.7:1. There are multiple potential reasons why the current prototype was unable to attain that performance:

1. SMA material training changed the transformation temperatures and the critical stress levels at which transformation strain manifests.
2. The SMA training jig induced heterogeneous material behavior along the length of the strip.
3. The SMA prestressing method resulted in variations in curvature and local composite material failure.
4. Epoxying the fluid flow block to the panel with a fixed radius of 3 inches inhibited the panel from fully closing.
5. The end shields covering the radiator tracking points during the cold state prohibited accurate measurements of the lowest possible heat rejection rates.

The morphing radiator prototypes tested in this work demonstrated the possibility for high turndown ratios using space qualified material. However, these studies illustrate the difficulty of integrating SMA actuators into a system. To further prove the performance of the system, more development must be performed refining manufacturing and assembly methods of both the SMA and composite materials.

5. CONCLUSIONS

Future manned space missions outside of low earth orbit require innovative solutions to help regulate the crew capsule temperature in spite of large variations in thermal environment. Novel radiator solutions will be required to provide turndown ratios between 6:1 and 12:1 to accommodate these harsh mission scenarios. In this work, a morphing radiator prototype was developed and tested to demonstrate the high turndown capability of the concept. Previous work has shown the possibility for the morphing radiator to provide a turndown ratio as high as 26.7:1, when the panel fully actuates, high performance coatings are applied, and radiative end shields are installed to minimize heat rejection when the panel is fully closed. This study focused on methods to predict radiator behavior efficiently and to manufacture a high performance morphing radiator capable of attaining the aforementioned turndown ratio.

A Matlab design tool was formulated to assist with actuator selection and placement, as well as mechanical performance predictions due to a temperature cycle. The design tool informed the manufacturing methods investigated, and it was found that a morphing radiator with SMA actuators embedded within the composite laminate was infeasible. Using this knowledge, manufacturing studies focused on adhesively bonding the SMA actuators to the outermost composite ply. Furthermore, the design tool supported investigating SMA actuators in the form of strips to achieve more uniform load and heat transfer between the SMA and the composite. The optimal SMA strip width and thickness was explored by implementing the area ratio into the design tool, information which drove procurement of the SMA material from NASA Glenn. Finally, a one-dimensional SMA constitutive model was implemented to predict the radiator mechanical performance as a function of temperature. This analysis elucidated that the transformation strain as a function of applied stress was equally as important as the transformation temperatures of a particular SMA material. Two examples based on tested materials demonstrated the feasibility of using the design tool with constitutive model to predict radiator performance.

Adhesive bonding was explored as an alternative method to mechanically fixturing the SMA actuators onto the composite panel. As the oxide layer present on most SMAs inhibits favorable bonding properties, a systematic surface treatment study was conducted to explore different methods of removing it. Mechanical abrasion and acid etching were compared, and it was found that acid etching required a hazardous pickle, so mechanical abrasion was used in future studies. Sol-gel surface treatments were applied to multiple test specimens, which were then lap shear tested or tested by actuating the SMA strip. It was found that the combination of sol-gel and mechanical abrasion produced the strongest bonds, but those bonds were still too weak to solely attach the SMA to the composite; thus, mechanical fixturing was once again selected for the tested prototypes.

Two distinct morphing radiator prototypes were tested in a thermal vacuum chamber at NASA Johnson Space Center. These prototypes included multiple component improvements over prior tests, such as high performance coatings, radiative end shields, and a fluid flow block designed to optimize the heat transfer from the working fluid to the radiator panel. Manufacturing methods were revised to accommodate SMA strip training and installation, in which a prestressing jig capable of withstanding 250 lbs was constructed. Two panels were installed in the thermal vacuum chamber in series, representing a step towards subsystem prototype demonstration. Additionally, a single panel with SMA actuators tuned for the specific temperature ranges was tested and attained a turndown ratio of 7.32:1, more than 50% higher than previous composite prototypes.

However, there are multiple areas for improvement to further increase the performance of the prototype. Most of the improvements lie within the manufacturing area of this study. To produce a morphing radiator with high turndown ratio, SMA material behavior must be thoroughly understood, before and after training; a robust prestressing procedure must be formulated and tested to ensure consistency; and a new flow block fixturing method must be conceptualized to limit the variability of radiator curvature. If the SMA material behavior and assembly process is well understood, the morphing radiator prototype will be able to achieve as high of a turndown ratio as projected.

REFERENCES

[1] NASA, “Mission Operations Report Apollo 13,” Tech. Rep. MSC-02680, Houston, TX, Apr. 1970.

[2] J. Lovell, “Apollo Expeditions to the Moon: Chapter 13.”

[3] S. S. KSC, “NASA - Generation Constellation Learns about Apollo 13,” Sept. 2007.

[4] D. Gilmore, *Spacecraft Thermal Control Handbook, Volume I: Fundamental Technologies*. Washington, DC: American Institute of Aeronautics and Astronautics, Inc., Dec. 2002.

[5] R. Stephan, “Overview of NASA’s thermal control system development for exploration project,” in *40th International Conference on Environmental Systems*, p. 6135, 2010.

[6] R. Stephan, “Overview of the Altair Lunar Lander Thermal Control System Design and the Impacts of Global Access,” in *41st International Conference on Environmental Systems*, (Portland, Oregon), American Institute of Aeronautics and Astronautics, July 2011.

[7] T. Leimkuehler and G. Lantz, “Single Loop Thermal Control for Deep Space Exploration,” in *42nd International Conference on Environmental Systems*, (San Diego, California), American Institute of Aeronautics and Astronautics, July 2012.

[8] R. Reysa and R. Thurman, “The International Space Station ECLS and thermal control systems - Overview,” in *Sixth European Symposium on Space Environmental Control Systems* (T.-D. Guyenne, ed.), vol. 400 of *ESA Special Publication*, p. 11, Aug. 1997.

[9] G. B. Ganapathi, E. T. Sunada, G. C. Birur, J. R. Miller, and R. Stephan, “Design Description and Initial Characterization Testing of an Active Heat Rejection Radiator with Digital Turn-Down Capability,” *SAE International Journal of Aerospace*, vol. 4, pp. 272–278, July 2009.

[10] H. Demiryont and D. Moorehead, “Electrochromic emissivity modulator for spacecraft thermal management,” *Solar Energy Materials and Solar Cells*, vol. 93, no. 12, pp. 2075–2078, 2009.

[11] R. Ponnappan, J. Beam, and E. Mahefkey, “Conceptual design of an 1 m long ’roll out fin’ type expandable space radiator,” in *4th Thermophysics and Heat Transfer Conference*, (Boston,MA,U.S.A.), American Institute of Aeronautics and Astronautics, June 1986.

[12] S. Ono, H. Nagano, Y. Nishikawa, M. Mishiro, S. Tachikawa, and H. Ogawa, “Thermophysical Properties of High-Thermal-Conductivity Graphite Sheet and Application to Deployable/Stowable Radiator,” *Journal of Thermophysics and Heat Transfer*, vol. 29, pp. 403–411, Apr. 2015.

[13] C. L. Bertagne, T. J. Cognata, R. B. Sheth, C. E. Dinsmore, and D. J. Hartl, “Testing and analysis of a morphing radiator concept for thermal control of crewed space vehicles,” *Applied Thermal Engineering*, vol. 124, pp. 986 – 1002, 2017.

[14] C. Bertagne, P. Walgren, L. Erickson, R. Sheth, J. Whitcomb, and D. J. Hartl, “Coupled Behavior of Shape Memory Alloy-Based Morphing Spacecraft Radiators: Experimental Assessment and Analysis,” *Smart Materials and Structures*, Apr. 2018.

[15] D. A. Ochoa, W. Vonau, and M. K. Ewert, “A Comparison between One- and Two-Loop ATCS Architectures Proposed for CEV,” *SAE International Journal of Aerospace*, vol. 4, pp. 344–350, July 2009.

[16] L. Erickson and A. Loveless, “APPROACH FOR SIZING AND TURNDOWN ANALYSIS OF A VARIABLE GEOMETRY SPACECRAFT RADIATOR,” p. 21, 2017.

[17] P. Walgren, C. Bertagne, M. Wescott, O. Benafan, L. Erickson, J. Whitcomb, and D. Hartl, “Development and Testing of a Shape Memory Alloy-Driven Composite Morphing Radiator,” *Shape Memory and Superelasticity*, pp. 1–10, Jan. 2018.

[18] S. H. Lee, I. Mudawar, and M. M. Hasan, “Thermal analysis of hybrid single-phase, two-phase and heat pump thermal control system (TCS) for future spacecraft,” *Applied Thermal Engineering*, vol. 100, pp. 190–214, May 2016.

[19] F. H. Sumonski and E. M. Tzccker, “APOLLO EXPERIENCE REPORT - COMMAND AND SERVICE MODULE ENVIRONMENTAL CONTROL SYSTEM,” Tech. Rep. TN D-6718, NASA, Houston, TX, Mar. 1972.

[20] T. S. Institute, “Apollo Command And Service Modules.”

[21] “Active Thermal Control System (ATCS) Overview,” Tech. Rep. 473486, Boeing Co., St. Louis, MO.

[22] NASA, “TA 14: Thermal Management Systems,” in *NASA Technology Roadmaps*, NASA, July 2015.

[23] “Altair Lunar Lander,” tech. rep., NASA, Johnson Space Center, Sept. 2008.

[24] M. Cohen, “From Apollo LM to Altair: Design, Environments, Infrastructure, Missions, and Operations,” in *AIAA SPACE 2009 Conference & Exposition*, (Pasadena, California), American Institute of Aeronautics and Astronautics, Sept. 2009.

[25] T. L. Bergman and F. P. Incropera, eds., *Fundamentals of heat and mass transfer*. Hoboken, NJ: Wiley, 7th ed ed., 2011.

[26] Y. V. Rao, *Heat Transfer*. Universities Press, Sept. 2001. Google-Books-ID: 9ZnvlodE2mcC.

[27] J. Oren, “Flexible Radiator System,” Tech. Rep. CR-171765, NASA, Houston, TX, 1982.

[28] J. P. Alario, “Monogrove Heat Pipe Radiator Shuttle Flight Experiment: Design, Analysis, and Testing,” July 1984.

[29] H. Demiryont, “Electrochromic Devices for Satellite Thermal Control,” vol. 813, pp. 64–73, AIP, 2006.

[30] E. Bannon, C. Bower, R. Sheth, R. Stephan, P. Chandrasekhar, and B. Zay, “Electrochromic Radiator Coupon Level Testing and Full Scale Thermal Math Modeling for Use on Altair Lunar Lander,” in *40th International Conference on Environmental Systems*, (Barcelona, Spain), American Institute of Aeronautics and Astronautics, July 2010.

[31] E. Sunada, G. Birur, G. Ganapathi, J. Miller, D. Berisford, and R. Stephan, “Design and Testing of an Active Heat Rejection Radiator with Digital Turn-Down Capability,” in *40th International Conference on Environmental Systems*, (Barcelona, Spain), American Institute of Aeronautics and Astronautics, July 2010.

[32] H. Nagano, Y. Nagasaka, and A. Ohnishi, “Simple Deployable Radiator with Autonomous Thermal Control Function,” *Journal of Thermophysics and Heat Transfer*, vol. 20, pp. 856–864, Oct. 2006.

[33] H. Nagano, A. Ohnishi, K. Higuchi, and Y. Nagasaka, “Experimental Investigation of a Passive Deployable/Stowable Radiator,” *Journal of Spacecraft and Rockets*, vol. 46, pp. 185–190, Jan. 2009.

[34] H. Nagano, A. Ohnishi, and Y. Nagasaka, “Development of a lightweight deployable/stowable radiator for interplanetary exploration,” *Applied Thermal Engineering*, vol. 31, pp. 3322–3331, Nov. 2011.

[35] S. Lillibridge, M. Navaroo, T. Cognata, and J. Guinn, “Freezable Radiator Testing,” in *40th International Conference on Environmental Systems*, (Barcelona, Spain), American Institute of Aeronautics and Astronautics, July 2010.

[36] S. Lillibridge and M. Navarro, “Six-Tube Freezable Radiator Testing and Model Correlation,” in *42nd International Conference on Environmental Systems*, (San Diego, California), American Institute of Aeronautics and Astronautics, July 2012.

[37] J. A. Nabity, “Modeling a Freezable Water-Based Heat Exchanger for Use in Spacecraft Thermal Control,” *Journal of Thermophysics and Heat Transfer*, vol. 28, no. 4, pp. 708–716, 2014.

[38] E. Bannon, C. Iacomini, C. Bower, and C. Linrud, “Stagnating Radiator Thermal Model Design and Verification,” in *10th AIAA/ASME Joint Thermophysics and Heat Transfer Conference*, American Institute of Aeronautics and Astronautics, 2010.

[39] E. Bannon and C. Iacomini, “Full Scale Demonstration and Modeling of a Quick Recovery Stagnating Radiator,” in *41st International Conference on Environmental Systems*, American Institute of Aeronautics and Astronautics, 2011.

[40] B. Abraham, J. Pantermuehl, B. Conger, C. Massina, and M. Gernhardt, “Thermal Design Assessment of a Water Based Fusible Heat Sink Radiator for Space Exploration Missions,” July 2018.

[41] T. Otanicar and R. Smith, “Controllable Nanoparticle Radiative Properties for High-Turndown Ratio Heat Rejection,” in *11th AIAA/ASME Joint Thermophysics and Heat Transfer Conference*, (Atlanta, GA), American Institute of Aeronautics and Astronautics, June 2014.

[42] R. B. Mulford, M. R. Jones, and B. D. Iverson, “Dynamic Control of Radiative Surface Properties with Origami-Inspired Design,” p. 10, 2015.

[43] N. Athanasopoulos and N. Siakavellas, “Variable emissivity through multilayer patterned surfaces for passive thermal control: preliminary thermal design of a nano-satellite,” July 2018.

[44] A. Hendaoui, N. Émond, M. Chaker, and m. Haddad, “Highly tunable-emittance radiator based on semiconductor-metal transition of VO2 thin films,” *Applied Physics Letters*, vol. 102, p. 061107, Feb. 2013.

[45] Y. Ke, S. Wang, G. Liu, M. Li, T. J. White, and Y. Long, “Vanadium Dioxide: The Multistimuli Responsive Material and Its Applications,” *Small*, vol. 14, no. 39, p. 1802025, 2018.

[46] K. Sun, C. A. Riedel, A. Urbani, M. Simeoni, S. Mengali, M. Zalkovskij, B. Bilenberg, C. de Groot, and O. L. Muskens, “VO2 Thermochromic Metamaterial-Based Smart Optical Solar Reflector,” *ACS Photonics*, vol. 5, pp. 2280–2286, June 2018.

[47] M. Benkahoul, M. Chaker, J. Margot, E. Haddad, R. Kruzelecky, B. Wong, W. Jamroz, and P. Poinas, “Thermochromic VO2 film deposited on Al with tunable thermal emissivity for

space applications," *Solar Energy Materials and Solar Cells*, vol. 95, pp. 3504–3508, Dec. 2011.

[48] T. Cognata, D. Hartl, R. Sheth, and C. Dinsmore, "A Morphing Radiator for High-Turndown Thermal Control of Crewed Space Exploration Vehicles," in *Proceedings of 23rd AIAA/AHS Adaptive Structures Conference*, (Kissimmee, FL), 2015.

[49] D. J. Hartl and D. Lagoudas, "Aerospace Applications of Shape Memory Alloys," *Proceedings of the Institution of Mechanical Engineers, Part G: Journal of Aerospace Engineering*, vol. 221 (Special Issue), pp. 535–552, 2007.

[50] P. Walgren, O. Benafan, L. Erickson, and D. Hartl, "Towards High Turndown Ratio Shape Memory Alloy-Driven Morphing Radiators," p. V002T02A009, Sept. 2018.

[51] D. Lagoudas, D. Hartl, Y. Chemisky, L. Machado, and P. Popov, "Constitutive Model for the Numerical Analysis of Phase Transformation in Polycrystalline Shape Memory Alloys," *International Journal of Plasticity*, vol. 3233, pp. 155–183, 2012.

[52] D. J. Hartl, J. T. Mooney, D. C. Lagoudas, F. T. Calkins, and J. H. Mabe, "Use of a Ni60ti shape memory alloy for active jet engine chevron application: II. Experimentally validated numerical analysis," *Smart Materials and Structures*, vol. 19, p. 015021, Dec. 2009.

[53] B. Carpenter and J. Lyons, "Lightweight Flexible Solar Array Validation Report," *EO-1 First, NASA mission, validation report*, 2002.

[54] A. D. Johnson, "STATE-OF-THE-ART OF SHAPE MEMORY ACTUATORS," p. 5, 1998.

[55] F. T. Calkins and J. H. Mabe, "Flight Test of a Shape Memory Alloy Actuated Adaptive Trailing Edge Flap," in *Volume 1: Multifunctional Materials; Mechanics and Behavior of Active Materials; Integrated System Design and Implementation; Structural Health Monitoring*, (Stowe, Vermont, USA), p. V001T04A007, ASME, Sept. 2016.

[56] O. Akselsen, "Joining of shape memory alloys," in *Shape Memory Alloys*, InTech, 2010.

[57] J. P. Oliveira, R. M. Miranda, and F. M. Braz Fernandes, “Welding and Joining of NiTi Shape Memory Alloys: A Review,” *Progress in Materials Science*, vol. 88, pp. 412–466, July 2017.

[58] F. R. Phillips and D. C. Lagoudas, “Effect of stress redistribution during thermal actuation of shape memory alloys in notched cylindrical bars,” *Journal of Intelligent Material Systems and Structures*, vol. 29, pp. 2149–2163, June 2018.

[59] W. Buehler and R. C. Wiley, “THE PROPERTIES OF TINI AND ASSOCIATED PHASES,” Tech. Rep. AD0266607, Naval Ordnance Lab, White Oak, MD, Aug. 1961.

[60] T. Shinoda, T. Tsuchiya, and H. Takahashi, “Friction welding of shape memory alloy,” *Welding International*, vol. 6, pp. 20–25, Jan. 1992.

[61] T. Y. Yang, R. K. Shiue, and S. K. Wu, “Infrared brazing of Ti50ni50 shape memory alloy using pure Cu and Ti15cu15ni foils,” *Intermetallics*, vol. 12, pp. 1285–1292, Dec. 2004.

[62] A. Baz, S. Poh, J. Ro, M. Mutua, and J. Gilheany, “Active Control of Nitinol-Reinforced Composite Beam,” in *Intelligent Structural Systems* (H. S. Tzou and G. L. Anderson, eds.), pp. 169–212, Dordrecht: Springer Netherlands, 1992.

[63] H. C. Man and N. Q. Zhao, “Enhancing the adhesive bonding strength of NiTi shape memory alloys by laser gas nitriding and selective etching,” *Applied Surface Science*, vol. 253, pp. 1595–1600, Nov. 2006.

[64] V. Birman, “Stability of Functionally Graded Shape Memory Alloy Sandwich Panels,” *Smart Materials and Structures*, vol. 6, pp. 278–286, 1997.

[65] S. Lacasse, P. Terriault, C. Simoneau, and V. Brailovski, “Design, manufacturing, and testing of an adaptive composite panel with embedded shape memory alloy actuators,” *Journal of Intelligent Material Systems and Structures*, vol. 26, pp. 2055–2072, Oct. 2015.

[66] V. Birman, “Enhancement of Stability of Composite Plates Using Shape Memory Alloy Supports,” *AIAA Journal*, vol. 45, pp. 2584–2588, Oct. 2007.

[67] G. Zhou and P. Lloyd, “Design, manufacture and evaluation of bending behaviour of composite beams embedded with SMA wires,” *Composites Science and Technology*, vol. 69, pp. 2034–2041, Oct. 2009.

[68] G. Faiella, V. Antonucci, F. Daghia, S. Fascia, and M. Giordano, “Fabrication and Thermo-Mechanical Characterization of a Shape Memory Alloy Hybrid Composite,” *Journal of Intelligent Material Systems and Structures*, vol. 22, pp. 245–252, Feb. 2011.

[69] B.-K. Jang and T. Kishi, “Thermomechanical response of TiNi fiber-impregnated CFRP composites,” *Materials Letters*, vol. 59, pp. 2472–2475, Aug. 2005.

[70] J. M. Jani, M. Leary, A. Subic, and M. A. Gibson, “A review of shape memory alloy research, applications and opportunities,” *Materials & Design*, vol. 56, pp. 1078–1113, 2014.

[71] Y. J. Zheng, L. S. Cui, and J. Schrooten, “Basic design guidelines for SMA/epoxy smart composites,” *Materials Science and Engineering: A*, vol. 390, pp. 139–143, Jan. 2005.

[72] A. W. Hansen, L. V. R. Beltrami, L. M. Antonini, D. J. Villarinho, J. C. K. d. Neves, C. E. B. Marino, and C. d. F. Malfatti, “Oxide Formation on NiTi Surface: Influence of the Heat Treatment Time to Achieve the Shape Memory,” *Materials Research*, vol. 18, pp. 1053–1061, Oct. 2015.

[73] F. Niccoli, M. Alfano, L. Bruno, F. Furgiuele, and C. Maletta, “Mechanical and Functional Properties of Nickel Titanium Adhesively Bonded Joints,” *Journal of Materials Engineering and Performance*, vol. 23, pp. 2385–2390, July 2014.

[74] T. Ogisu, N. Ando, J. Takaki, T. Okabe, and N. Takeda, “Improved Surface Treatment of SMA Foils and Damage Suppression of SMA-Foil Embedded CFRP Laminates,” *Journal of Intelligent Material Systems and Structures*, vol. 12, pp. 265–270, Apr. 2001.

[75] ASTM, “Standard Test Method for Apparent Shear Strength of Single-Lap-Joint Adhesively Bonded Metal Specimens by Tension Loading (Metal-to-Metal),” Tech. Rep. D1002-10, ASTM International, West Conshohocken, PA, 2010.

[76] ASTM, “Test Method for Peel or Stripping Strength of Adhesive Bonds,” Tech. Rep. D903-98, ASTM International, West Conshohocken, PA, 2017.

[77] A. Santoro, M. Alfano, C. Maletta, L. Bruno, F. Furgiuele, and S. Candamano, “Adhesion strength of adhesive bonded NiTi thin metal sheets Resistenza alladesione di lamine incollate in lega Nichel-Titanio,” p. 8, 2013.

[78] J. Paine, W. Jones, and C. Rogers, “Nitinol actuator to host composite interfacial adhesion in adaptive hybrid composites,” in *33rd Structures, Structural Dynamics and Materials Conference*, Structures, Structural Dynamics, and Materials and Co-located Conferences, American Institute of Aeronautics and Astronautics, Apr. 1992.

[79] N. Smith, G. Antoun, A. Ellis, and W. Crone, “Improved adhesion between nickeltitanium shape memory alloy and a polymer matrix via silane coupling agents,” *Composites Part A: Applied Science and Manufacturing*, vol. 35, pp. 1307–1312, Nov. 2004.

[80] L. L. Hench and J. K. West, “The sol-gel process,” *Chemical Reviews*, vol. 90, pp. 33–72, Jan. 1990.

[81] T. Zimmerman, K. Blohowiak, M. Dilligan, T. Calkins, and J. Mabe, “Adhesive bonding of hybrid actuated shape memory alloy-composite structures,” *International SAMPE Technical Conference*, Jan. 2010.

[82] H. Truong, M. Martinez, O. Ochoa, and D. Lagoudas, *Experimental and Computational Investigations of Hybrid Interfaces in Hybrid Composite Laminates*. Sept. 2015.

[83] H. T. X. Truong, *An Experimental and Computational Study on Co-Cured Hybrid Metal-Polymer Matrix Composite Interfaces in High Temperature Hybrid Composite Laminates*. Thesis, May 2016.

[84] C. Bertagne, R. Sheth, D. Hartl, and J. D. Whitcomb, “Simulating Coupled Thermal-Mechanical Interactions in Morphing Radiators,” in *Proceedings of SPIE, Active and Passive Smart Structures and Integrated Systems*, vol. 9431, (San Diego, CA), pp. 94312F–94312F–10, Mar. 2015.

[85] M. Wescott, J. S. McQuien, C. L. Bertagne, J. D. Whitcomb, D. J. Hartl, and L. Erickson, "Design and Fabrication of a Composite Morphing Radiator Panel Using High Conductivity Fibers," American Institute of Aeronautics and Astronautics, Jan. 2017.

[86] R. M. Jones, *Mechanics of composite materials*. Philadelphia, PA: Taylor & Francis, 2nd ed., 1999.

[87] W. M. Lai, D. Rubin, and E. Krempl, "CHAPTER 4 - Stress and Integral Formulations of General Principles," in *Introduction to Continuum Mechanics (Fourth Edition)*, pp. 155–200, Boston: Butterworth-Heinemann, 2010.

[88] E. A. Peraza Hernandez, D. J. Hartl, and D. C. Lagoudas, "Introduction to Active Origami Structures," in *Active Origami: Modeling, Design, and Applications* (E. A. Peraza Hernandez, D. J. Hartl, and D. C. Lagoudas, eds.), pp. 1–53, Cham: Springer International Publishing, 2019.

[89] "Mechanical Cleaning Systems," in *Surface Engineering* (C. Cotell, J. Sprague, and F. Smidt, eds.), pp. 55–66, ASM International, 1994.

[90] "Acid Cleaning," in *Surface Engineering* (C. Cotell, J. Sprague, and F. Smidt, eds.), pp. 48–54, ASM International, 1994.

[91] A. Hassel, "Surface treatment of NiTi for medical applications," *Minimally Invasive Therapy & Allied Technologies*, vol. 13, no. 4, pp. 240–247, 2004.

[92] R. D. S. G. Campilho, ed., *Strength prediction of adhesively-bonded joints*. Boca Raton: CRC Press, Taylor & Francis Group, CRC Press is an imprint of the Taylor & Francis Group, an informa business, 2017.

[93] O. Volkerson, "die nietkraftverteilung in zugbeanspruchten Nietverbindungen mit konstanten Laschenquerschnitten," *Luftahrtforschung*, vol. 15, pp. 41–47, 1938.

[94] Loctite, "Loctite EA 9309.3na Aero Epoxy Paste Adhesive," technical Data Sheet, Bay Point, CA, July 2013.

[95] 3M, “3m Scotch-Weld 2216 B/A Gray Epoxy Adhesive,” technical Data Sheet, Mar. 2002.

[96] A. Silver, “Arctic Silver Thermal Adhesive,” technical Data Sheet, Arctic Silver, Inc, 2011.

APPENDIX A

SMA CHARACTERIZATION DATA

This appendix contains the data for the SMA characterization completed for this study. Characterization was conducted for three different SMA foils (or sheets) of various thickness (nominal thicknesses of 0.0762 mm, 0.127 mm, and 0.2032 mm).

A.1 0.0762 mm thick NiTi

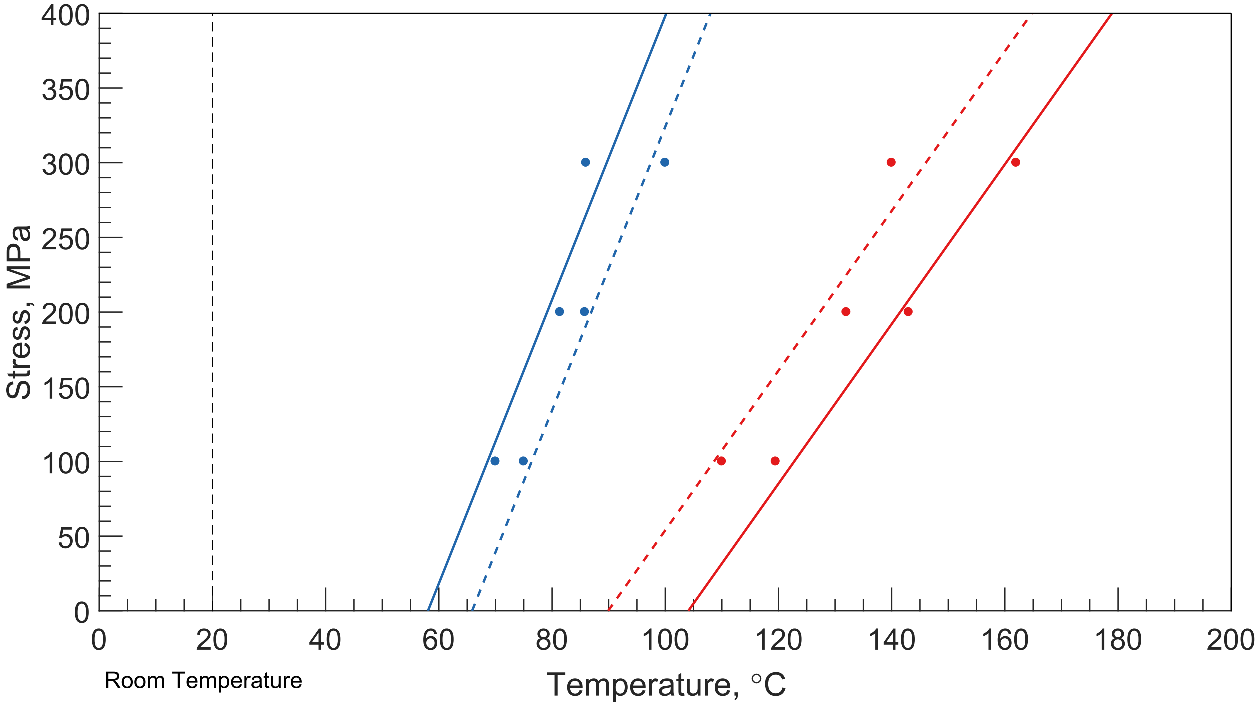

Figure A.1: Phase Diagram for the 0.0762 mm thick sheet, as determined by 3 isobaric thermal cycles (as denoted by the solid points)

Table A.1: Calibrated model parameters for the 8 mil thick NiTi used in the double panel thermal vacuum chamber tests

Model Parameter	**Calibrated value**
E^M	67.6 GPa
E^A	117.63 GPa
ν^M	0.33
ν^A	0.33
α^M	$0 \cdot 10^{-6}$ m/(m·°C)
α^A	$0 \cdot 10^{-6}$ m/(m·°C)
M_f	-59.57 °C
M_s	-52.555 °C
A_s	0.1446 °C
A_f	11.4731 °C
C^M	4.2525 MPa/°C
C^A	8.1976 MPa/°C
H_{min}	0.0%
H_{max}	4.86%
k	0.0403 MPa^{-1}
$\bar{\sigma}_{crit}$	60 MPa
n_1	0.5457
n_2	0.4644
n_3	0.4690
n_4	0.5458

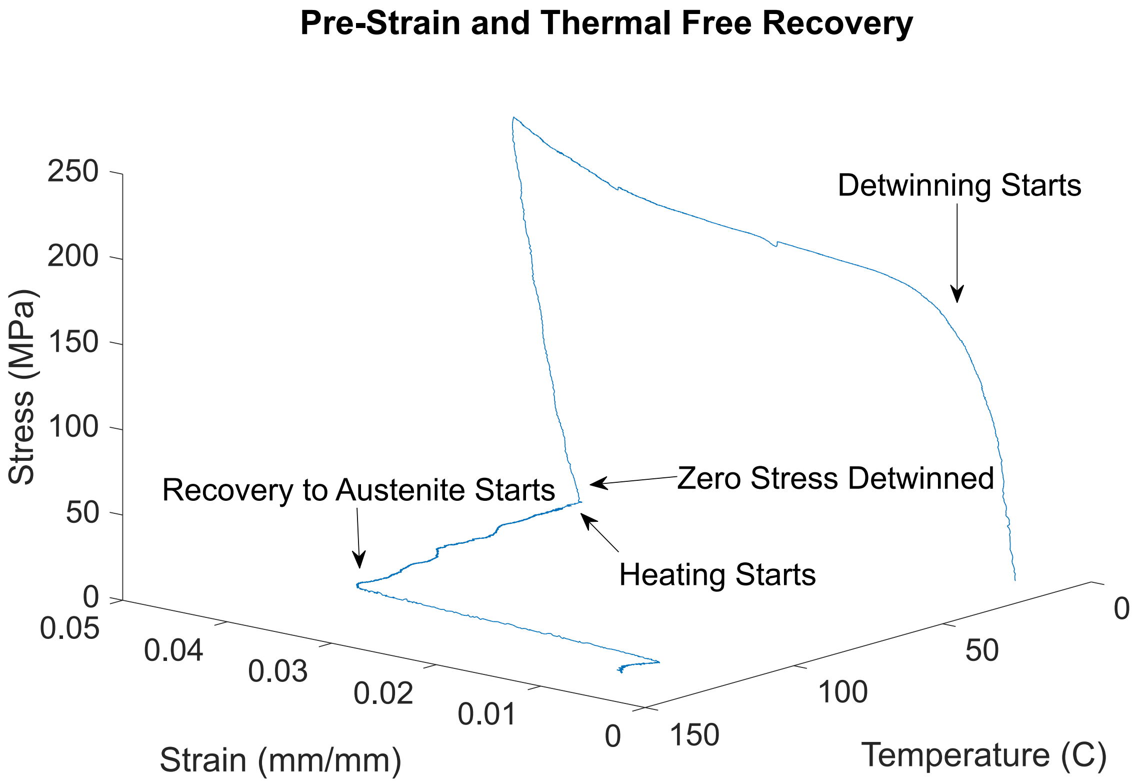

Figure A.2: Detwin and Free-recovery cycle for the 0.0762 mm thick sheet.

A.2 0.2032 mm thick NiTi

A.3 0.1270 mm thick Cobalt alloy

The NiTiCo was rolled to feature a thickness of approximately 0.1270 mm, and the material underwent multiple annealing heat treatments to better tune the transformation temperatures for the operating environment in Chamber G. Figure A.7 illustrates the effect of the heat treatments and the ability of the researchers at Glenn Research to shift transformation temperatures to better fit a particular mission profile. Figure A.7a depicts the zero-stress transformation temperatures before heat treatment, and features a distinct R-phase. After heat treatment, the hysteresis was tightened, but the austenite finish temperature had the potential of prohibiting the radiator from fully opening at high stresses. To remedy this, a final round of annealing was conducted to attempt to shift the transformation temperatures down 20 °C.

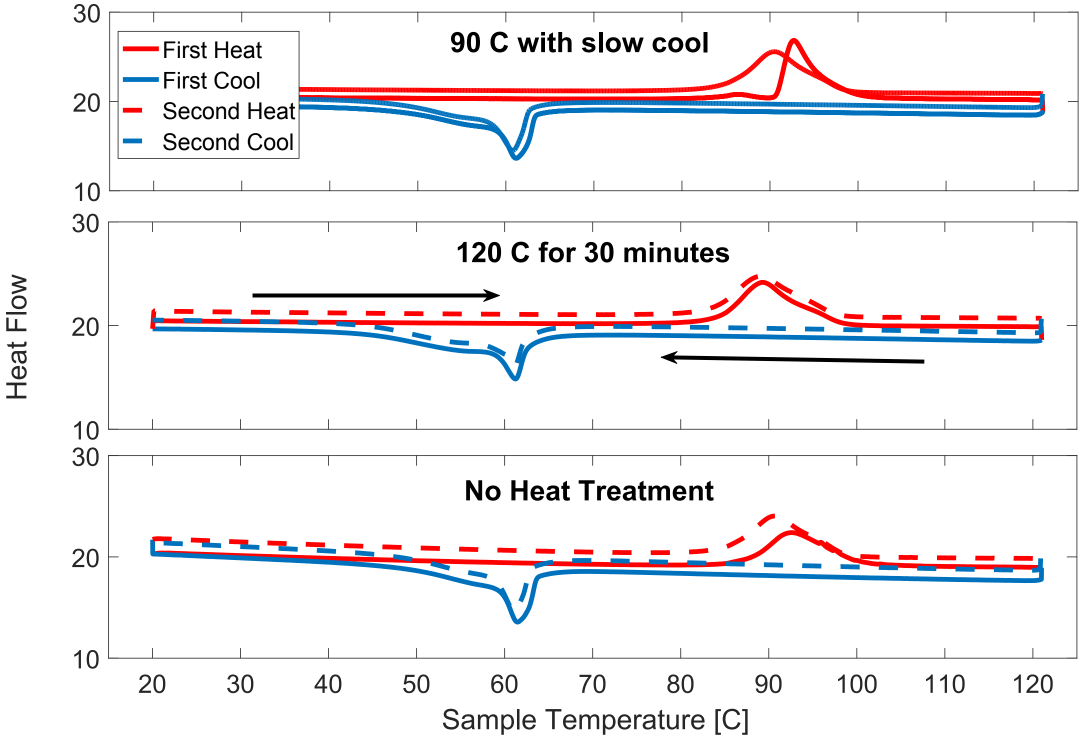

Figure A.3: Differential Scanning Calorimetry plots with various heat treatments. No variation in transformation was observed.

Furthermore, the material exhibits consistent zero-stress transformation strain (as shown in Figure A.9a, which is encouraging for thermal vacuum chamber testing. The evolution of maximum transformation strain (H^{cur}) as a function of applied tensile stress, as well as the related isobaric actuation cycles are shown in Figure A.9. Although the last round of annealing removed most stability from this material, sufficient training was accomplished in 15 isobaric cycles.

Table A.2: Calibrated model parameters for the 5 mil thick NiTiCo used in the single panel thermal vacuum chamber tests

Model Parameter	**Calibrated value**
E^M	69.8 GPa
E^A	119.87 GPa
ν^M	0.33
ν^A	0.33
α^M	$0 \cdot 10^{-6}$ m/(m·°C)
α^A	$0 \cdot 10^{-6}$ m/(m·°C)
M_f	-61.2592 °C
M_s	-9.1556 °C
A_s	-34.1691 °C
A_f	9.3199 °C
C^M	11.982 MPa/°C
C^A	7.1717 MPa/°C
H_{min}	2.49%
H_{max}	3.82%
k	0.034754 MPa^{-1}
$\bar{\sigma}_{crit}$	0 MPa
n_1	0.2352
n_2	0.1255
n_3	0.5817
n_4	0.4487

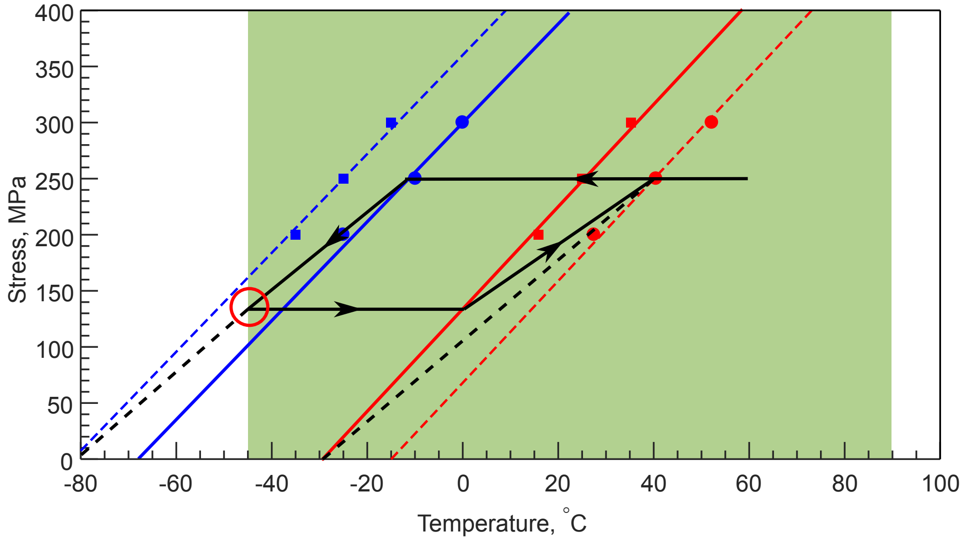

Figure A.4: Experimental phase diagram for the .008 in thick NiTi.

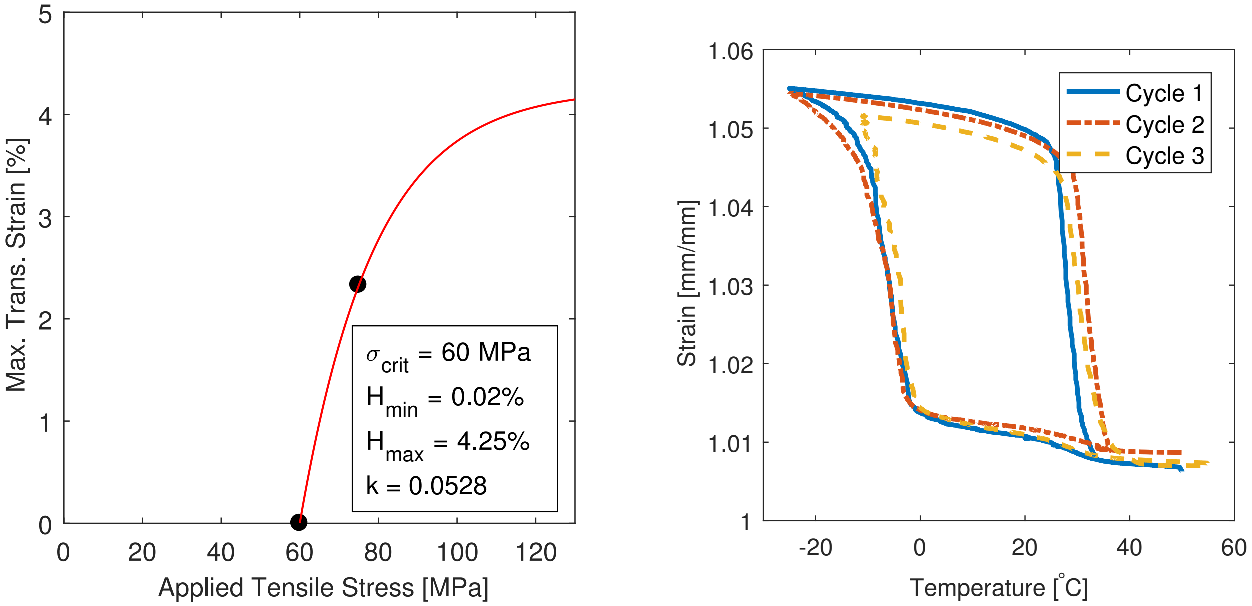

(a) Maximum transformation strain as a function of applied tensile stress

(b) Isobaric training cycles

Figure A.5: Additional characterization data for the .008 in thick NiTi

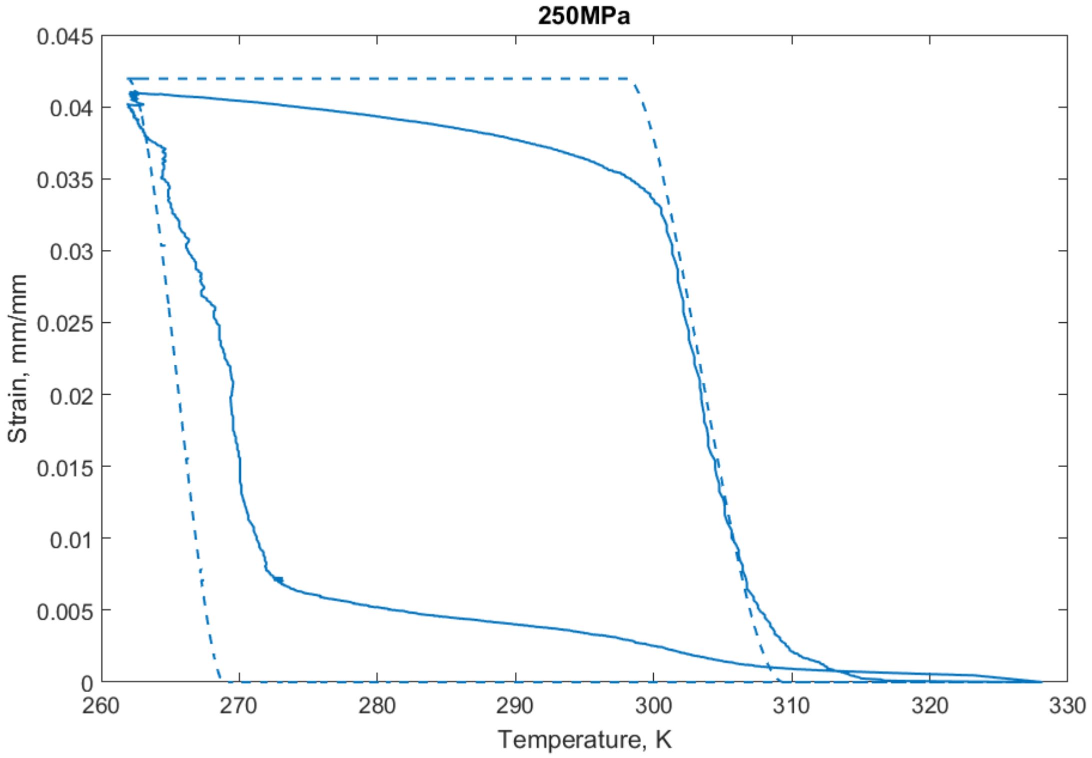

Figure A.6: Model Predictions vs. Experimental Data for the 8 mil NiTi Strip

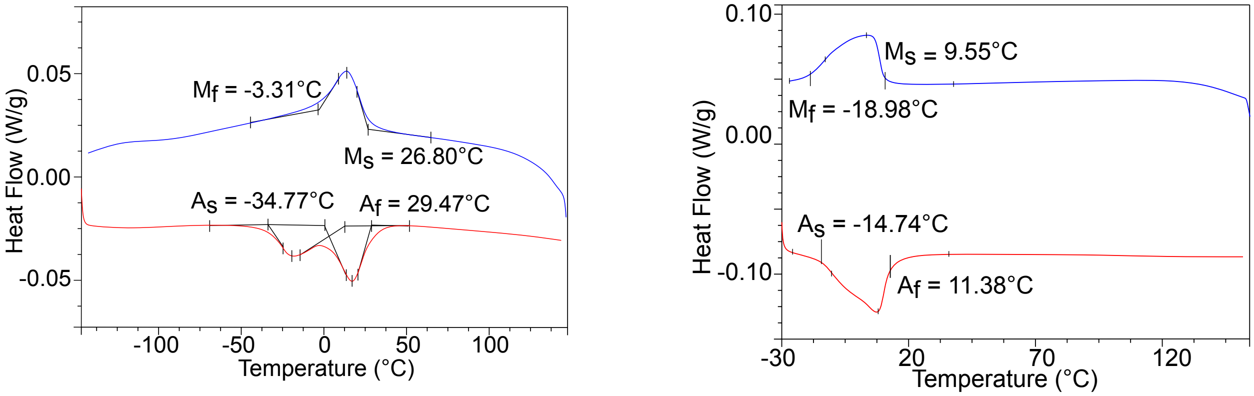

(a) Before heat treatment

(b) After heat treatment

Figure A.7: Differential Scanning Calorimetry of the NiTiCo, highlighting the effect of heat treatment on transformation temperatures

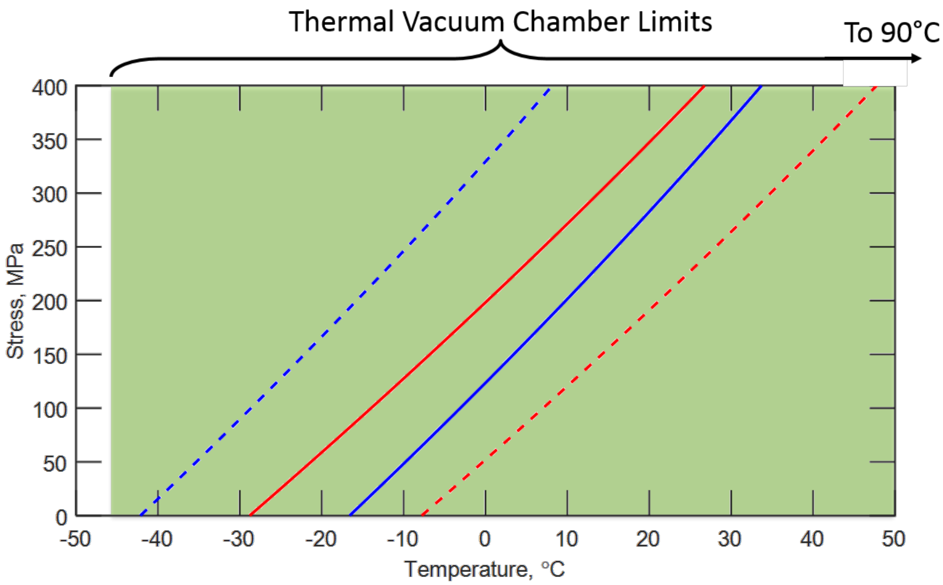

Figure A.8: Experimental phase diagram for the .005 in thick NiTiCo. The green rectangle shows the thermal vacuum chamber temperature limits as they relate to the transformation temperatures of the SMA.

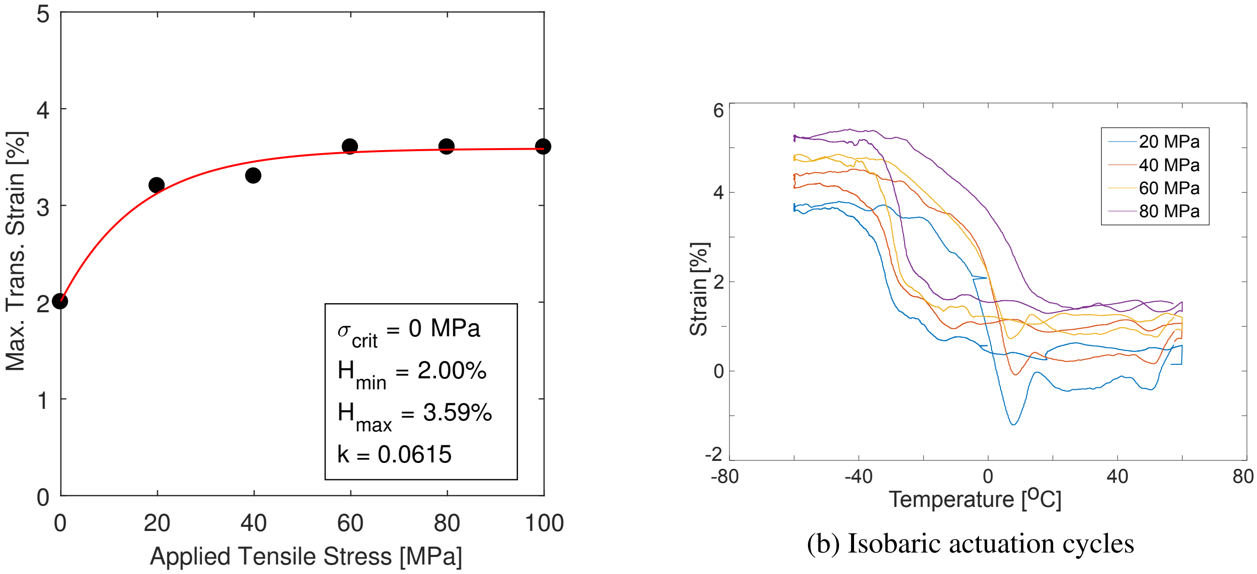

(b) Isobaric actuation cycles

(a) Maximum transformation strain as a function of applied tensile stress

Figure A.9: Additional characterization data for the .005 in thick NiTiCo

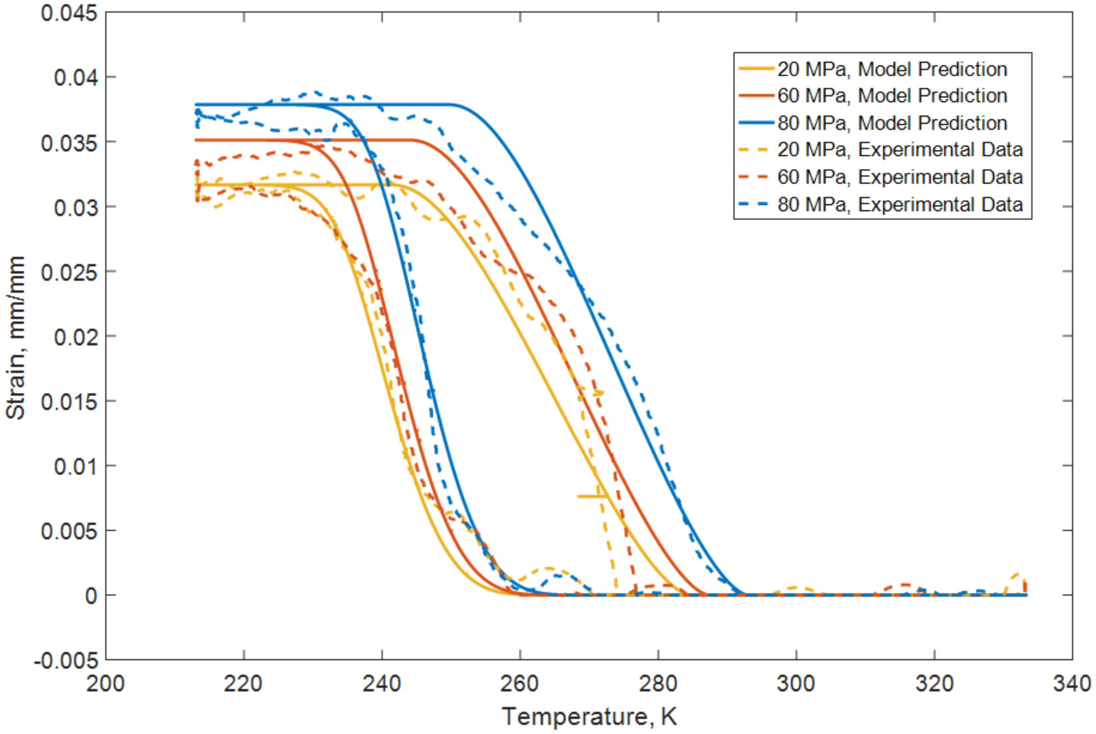

Figure A.10: Model Predictions vs. Experimental Data for the 5 mil NiTiCo strip

APPENDIX B

CONTRIBUTION OF VIEW FACTOR AND SURFACE EMISSIVITY ON HEAT REJECTION RATE

To explore the effect of varying both the panel view factor and surface emissivities on the overall heat rejection rate, a full factorial design of experiment was conducted. Panel radius was varied from fully closed to open. The convex and concave surface emissivities were varied between 0.1 to 0.3 and 0.7 to 0.9, respectively. Factor effects of these design variables are shown in figure B.1 with respect to the average heat rejection rate at that design variable level. It can be seen that the surface emissivities contribute to the heat rejection rate in a linear fashion; a two-times increase in the emissivity will result in a two-times increase in the heat rejection rate. However, as the panel radius contributes to the heat rejection rate in a nonlinear fashion, there are diminishing returns to the panel heat rejection rate as the panel nears a semicircular shape. This reinforces the design rationale of considering a semicircular panel "fully open."

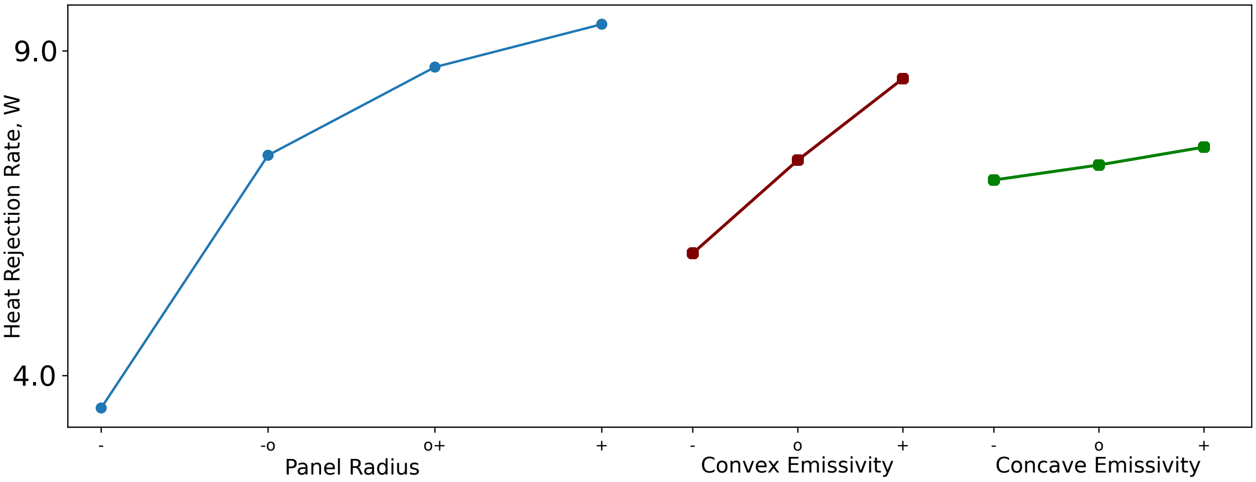

Figure B.1: Factor effects of panel radius and concave and convex emissivities.